Paternò-Büchi-Funktionalisierung von Phospholipiden in Gewebeschnitten für doppelbindungsspezifische bildgebende MALDI-Massenspektrometrie

Paternò-Büchi functionalization of phospholipids in tissue sections for double-bond position isomer resolved MALDI mass spectrometry imaging

Cumulative dissertation

by

Fabian Wäldchen

JUSTUS-LIEBIG-UNIVERSITÄT GIESSEN

Submitted to the

Faculty of Biology and Chemistry (FB08)

and prepared at the

Institute of Inorganic and Analytical Chemistry

For the degree of

Doctor rerum naturalium (Dr. rer. nat.)

Justus Liebig University Giessen, Germany

Giessen 2023

Gutachter

Erster Gutachter:

Prof. Dr. Bernhard Spengler

Institut für Anorganische und Analytische Chemie

Justus-Liebig-Universität Giessen

Zweiter Gutachter:

Jun.-Prof. Dr. Sven Heiles

Arbeitsgruppe Lipidomics der Abteilung Bioanalytik

Institut für Spektrochemie und Angewandte Spektroskopie Dortmund

Inhalt

Publication List

1. Selective Phosphatidylcholine Double Bond Fragmentation and Localisation using Paternò-Büchi Reactions and Ultraviolet Photodissociation

   Fabian Wäldchen, Simon Becher, Patrick Esch, Mario Kompauer, and Sven Heiles

   The Analyst, **2017**, 142, 4744-4755

   DOI: 10.1039/c7an01158

2. Reactive Matrix-Assisted Laser Desorption/Ionization Mass Spectrometry Imaging Using an Intrinsically Photoreactive Paternò-Büchi Matrix for Double-Bond Localization in Isomeric Phospholipids

   Fabian Wäldchen, Bernhard Spengler, and Sven Heiles

   Journal of the American Chemical Society, **2019**, 141, 11816-11820

   DOI: 10.1021/jacs.9b05868

3. Multifunctional Reactive MALDI Matrix Enabling High-Lateral Resolution Dual Polarity MS Imaging and Lipid C=C Position-Resolved MS^2 Imaging

   Fabian Wäldchen, Franziska Mohr, Andreas H. Wagner, and Sven Heiles

   Analytical Chemistry, **2020**, 92, 14130-14138

   DOI: 10.1021/acs.analchem.0c03150

Publications 2 and 3 are the basis of this doctoral thesis and are consequently referred to as “first” and “second publication of the project”, respectively.

Publication 1 presents earlier research results.

Zusammenfassung

Diese Arbeit beschreibt die Entwicklung und Implementierung neuartiger Matrizen und Probenvorbereitungsprotokolle für die bildgebende Tandemmassenspektrometrie (*engl. tandem mass spectrometry imaging* – MS^2I) von C=C-Doppelbindungspositionsisomeren (DBPIs) von Lipiden mittels Matrix-unterstützter Laser-Desorption/Ionisation (MALDI). Grundlage der Methodik ist die MALDI-Laser-aktivierte Paternò-Büchi- (PB-)Funktionalisierung der Doppelbindungen (DBs) mit PB-reaktiven MALDI-Matrizen. Die Kollisionsaktivierung der PB-funktionalisierten Lipide führt zur DB-Fragmentierung, und anhand der zugehörigen Neutralverluste können die DB-Positionen in den Fettsäureresten abgeleitet werden.

Im ersten Projektteil wurden flüssige PB-Reagenzien zur Lipidfunktionalisierung auf Gewebe verwendet, bevor feste Verbindungen in Betracht gezogen wurden, gleichzeitig als PB-Reagenz und MALDI-Matrix zu fungieren. Benzophenon (BPh) wurde als PB-reaktive Matrix identifiziert und Protokolle zu dessen Applikation auf Proben via pneumatischen Sprühens oder Sublimierens entwickelt. Bei einem Vergleich der mit BPh und der mit einer bekannten Matrix generierten MSI-Bilder zeigt sich der Nutzen der neuen Matrix. Nebst der Einsatzbarkeit für allgemeine MSI-Experimente, erlaubt BPh die Lokalisierung von DB-Positionen in verschiedenen Lipidstandards und die hochaufgelöste Abbildung lateraler DBPI-Verteilungen in Gewebeschnitten des Cerebellums der Maus (15 µm Pixelgröße) und in parasitären Würmern (20 µm Pixelgröße). Zur Auftragung der PB-reaktiven Matrix sind kein spezielles Zubehör oder zusätzliche Probevorbereitungsschritte vonnöten.

Ziel des zweiten Projektteils war die Etablierung einer PB-reaktiven Matrix, die eine effizientere Lipidionisierung und PB-Funktionalisierung ermöglicht, sowie eine höhere laterale Auflösung und die Ausweitung der DBPI-Analyse auf mehr Lipidklassen. Alle zwölf getesteten BPh-Derivate wiesen eine bessere Ionisationseffizienz auf (bis zu 50-fach höhere Ionenintensitäten), allerdings führten nur fünf davon zu PB-Produkten. Die höchste Ausbeute wurde mit 2-Benzoylpyridin (BzPy) erzielt, und dessen Einsatz ermöglichte die DBPI-Analyse für mehr Lipidklassen, sowie erste Beispiele im negativ-Ionen-Modus. Ebenso wurde die laterale Auflösung in MSI-Experimenten von 15 µm Pixelgröße (mit BPh) auf 7 µm (mit BzPy) verbessert. Die Listen annotierter Lipide des Cerebellums der Maus enthielten Spezies, die nur mit BzPy-Anlagerung detektierbar waren. Die neue Matrix begünstigt die Protonierung von an sie gebunden Spezies höchstwahrscheinlich aufgrund ihres basischen Stickstoffatoms im Pyridin-Ring. Auch die Pixelgröße von DBPI-auflösenden MS^2I-Bildern wurde verbessert von 15 µm (mit BPh) auf 10 µm (BzPy), was die Auflösung lateraler DBPI-Verteilungen in β-Zellen der Langerhans-Inseln in Gewebeschnitten des Pankreas der Maus möglich machte. Die DBP-Isomerie von sechs Lipidsignalen

wurde aufgeklärt und die bildgebende Auftragung der DBPI-diagnostischen Fragmentionensignale zeigte unterscheidbare Verteilungen für vier DBPIs.

Der Anwendung der entwickelten Methode zur MSI- und DBPI-Analyse von Diabetes- und Herz-Kreislauf-Erkrankungs-Modellgewebe wurde der dritte Projektteil gewidmet. Den Ergebnissen in Langerhans-Inseln des Maus-Pankreas folgend, wurden DBPI-Signalintensitäts-Verhältnisse zwischen diabetischem und gesundem Pankreasgewebe verglichen. Signifikante Unterschiede deuteten auf veränderte Rollen der DBPIs im erkrankten Gewebe hin. Im Falle der Herz-Kreislauf-erkrankten Mäuse wurden die DBPI-Verteilungen in Lungengewebe studiert. Neben der Auflösung von Bronchien und Blutgefäßen in den erhaltenen MSI-Bildern wurden erhöhte Signale eines Lipid-DBPIs im Epithelium der Bronchien detektiert. Diese Ergebnisse demonstrieren exemplarisch die Anwendbarkeit der entwickelten Methode für biochemische und medizinische Studien. Zukünftige Forschungen sollten die Optimierung der Methode für höhere Ionen- und PB-Ausbeuten in den Fokus stellen, um DBPI-auflösende MS^2I-Analysen für mehr Lipidklassen und Lipide geringer Häufigkeit zu ermöglichen. Unter Verwendung von Matrizen, die diese Voraussetzung erfüllen, könnte der hier präsentierte Ansatz als eine Routinemethode für medizinische Forschung und Diagnose implementiert werden. Als solche könnte er Forschende dabei unterstützen, lokale Lipidmetabolismus-Vorgänge wie beispielsweise Desaturasen- und Elongasen-Aktivität und -spezifizität besser zu beschreiben.

Abstract

This work describes the development and implementation of novel matrices and sample preparation protocols for matrix-assisted laser desorption/ionization (MALDI) tandem mass spectrometry imaging (MS^2I) of C=C double bond (DB) position isomers (DBPI) of lipids. The methodology is based on MALDI-laser-triggered Paternò-Büchi (PB) functionalization of the lipid DBs with PB-reactive MALDI matrices. Collisional activation of the PB-functionalized lipids leads to DB fragmentation, and the corresponding neutral losses are used to pinpoint DB positions in their fatty acid residues.

In the first part of the project, liquid PB reagents were employed for on-tissue lipid functionalization before solid compounds were considered to serve as reagent and MALDI matrix. Benzophenone (BPh) was identified as a PB-reactive matrix and matrix application protocols were developed for pneumatic spraying or sublimation of BPh onto samples. Comparing the MS images acquired with the new matrix BPh to imaging results of a common matrix demonstrated BPh's benefit for MALDI-MSI. Apart from working as a matrix for common MSI, BPh allowed to localize DB positions in various lipid standards and to resolve lateral DBPI-distributions with high resolution in mouse cerebellum (15 µm pixel size) and in a parasite worm (20 µm pixel size). To deposit the PB-reactive matrix, no special equipment and no additional sample pretreatment were required.

The second project part targeted to find PB-reactive matrices, providing more efficient lipid ionization and functionalization for higher lateral resolutions and the DBPI analysis of more lipid classes. All twelve screened BPh derivatives could be used as MALDI matrices and enhanced the ion intensity (up to 50-fold) but only five compounds yielded PB products. The highest PB reactivity was found for 2-benzoylpyridine (BzPy). With BzPy, DBPI analysis was enabled for more lipid classes and for first examples in the negative-ion mode. Also, the lateral resolution of MALDI-MSI experiments was improved (7 µm) compared to BPh (15 µm). The annotation lists of mouse cerebellum tissue lipids contained species that were exclusively detected with BzPy attachment. Most likely due to its basic nitrogen, BzPy boosts the intensity of protonated ions. Compared to 15 µm pixel size in DBPI-resolved MS^2I with BPh, BzPy allowed a reduced pixel size of 10 µm, making possible the resolution of lateral DBPI distributions in β-cells of the murine pancreatic islets. The DBP isomerism was elucidated for six lipid signals. Imaging the DBPI-diagnostic fragment ion signals showed distinct distributions for four DBPIs.

Applying the established method to disease-model tissue was the third part of the project. Namely, it was used for MSI and DBPI analysis of diabetes- and cardiovascular-disease-model mouse tissue. Following up the findings in murine pancreatic islets, the DBPI ratios in diabetic and healthy pancreas tissue were compared. Significant variations suggested changing roles of the DBPIs. Concerning

cardiovascular-diseased mice, DBPI distributions in lung tissue were studied. Besides resolving bronchi and blood vessels in MS images, an elevation of a phosphatidylcholine DBPI level was detected in the epithelium of the bronchi. These results exemplify the applicability of the developed method to biochemical and medical studies. In future, the method should be optimized for higher ion- and PB-yields to facilitate DBPI-resolved MS^2I of more lipid classes and low-abundance lipids. With matrices fulfilling this requirement, the PB-reactive matrix approach could be implemented as a routine method in medical research and diagnosis. As such, it would assist the investigation of localized lipid metabolism, e.g. desaturase and elongase activities and specificities.

1. Introduction

1.1. Lipid Structures and Roles

Biological systems are composed of three major functional classes. These are proteins, genes and metabolites.[1] Their analyses are called proteomics, genomics and metabolomics, where the "-omics" suffix refers to the investigation of the *entirety* of the three classes of biomolecules.[2] Metabolomics include lipidomics, dealing with the analysis of lipids which are loosely defined as biomolecules that are soluble in nonpolar solvents.[3] Whereas proteomics and genomics are well established methods, lipidomics is still an emerging research field. In the last ten years, the number of publications, resulting from a search for the term "lipidomics" in "Web of Knowledge", increased by a factor of approximately eight.[4] In contrast to the understanding of lipids just being membrane building blocks, energy storage and passive components of biological processes, current research showed that they play crucial roles in signaling and are active parts of cell function.[5] The wide field of lipid functions leads to a plethora of different structures (>100,000[4]) summarized under the term lipids.[3] Because this includes compounds that are greatly different in structure and function, the lipids were categorized by the *International Lipid Classification and Nomenclature Committee*. Based on biosynthetic pathways and structural similarities, the LIPID MAPS® databank established eight categories (fatty acids (FAs), glycerolipids (GLs), glycerophospholipids (GPs), sphingolipids (SPs), sterol lipids (STs), prenol lipids, saccharolipids, polyketides). These were subdivided in numerous classes and subclasses, e.g. based on the lipid backbone (blue in Figure 1A and 1C) like glycerol and sphingosine and/or the head group such as phosphocholine, -ethanolamine, -glycerol, -inositol, or serine (green in Figure 1A and 1B).[6] In the

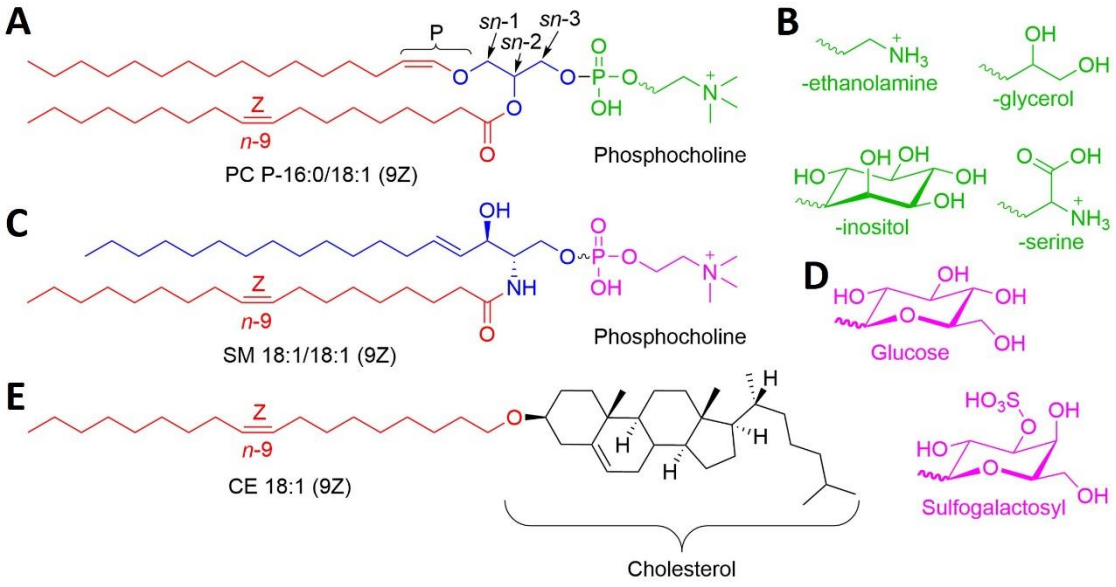

Figure 1. Examples of some lipids to illustrate lipid structures and nomenclature.

example of GPs, FAs (red in Figure 1A, 1C and 1E) are attached to the lipid backbone in positions labeled by the stereospecific numbering (*sn*-1/*sn*-2/*sn*-3) and are described by their length and unsaturation (carbon number:number of unsaturation sites) as well as the DB position(s) and geometry (cis/trans or Z/E). Naming of the DB position can be done counting from the acyl carbon (Δ-nomenclature used by LIPID MAPS®) or the aliphatic end of the fatty acyl (*n*-x-nomenclature used in common trivial names). As an alternative to FAs, also alkyls or alkenyls can be attached by ether or vinyl ether bonds, which is indicated by an O- or a P-character, respectively. According to the LIPID MAPS® nomenclature, the lipid shown in Figure 1A would therefore be named PC P-16:0/18:1 (9Z), where PC stands for phosphatidylcholine and the order in that the FAs are given reflects their position (*sn*-1/*sn*-2) on the backbone. Besides phosphosphingolipids, like the sphingomyelin (SM 18:1/18:1) shown in Figure 1C, the sphingosine backbone can also carry one or more glycosyl units (e.g. glucose or galactose) or sulfoglycosyl (e.g. sulfogalactosyl) head group (violet in Figure 1D), resulting in a glycosphingolipid (HexCer) or sulfatide (SHexCer), respectively. In the case of sterol lipids like the cholesterol ester (CE) shown in Figure 1E, backbone and head group are merged in the cholesterol moiety.[6]

One important function of lipids is the separation of the intracellular medium (cytoplasm) and the extracellular medium as well as the compartmentalization of cell organelles.[7] Both media are aqueous solutions which is why the lipids form a bilayer membrane where the hydrophilic head groups point to the intra- and extracellular space and the hydrophobic tails point to each other building up the hydrophobic core that blocks the mixing of intra- and extracellular media. Lipid bilayer membranes are thus the barrier against substantial fluctuations maintaining the parameters: temperature, relative humidity, pH value, sun exposure, osmotic pressure and nutrient concentration.[8] Lysosomes are organelles that digest macromolecules to recycle their components. The responsible lysosomal enzymes showcase the importance of compartmentalization because they are only active in the lysosome-internal acidic pH value (between 4.5 and 5)[9] that is kept constant by the membrane and transmembrane proton pumps.[10]

At the same time, lipids are the membrane's gatekeepers and control the traffic between intra- and extracellular space. Plasma membranes are selectively permeable, enabling to transport distinct species in and out of cells.[8] Phosphatidylcholines (PCs), -ethanolamines (PEs), -serines (PSs), -inositols (PIs) and sphingomyelins (SMs) are the main components of cell membranes, and the detailed composition depends on the organism, cell type and even cell state. Different compositions, especially, local differences lead to changes of the membrane tension, thickness, and curvature.[7] Phosphatidic acids (PAs) and PEs, for example, possess small head groups and are cone-shaped lipids, in contrast to PCs, phosphatidylglycerols (PGs), PSs and PIs that have bigger head groups and are cylindrical- or even invertedly cone-shaped. Membrane regions that are rich of PAs or PEs, hence, have a negative

curvature that looks like a valley, regions dominated by cylindrical-shaped lipids are planar and an enrichment of inverted cone-shaped lipids leads to a positive curvature.[11,12] Such curvature distortions e.g. serve the transport of proteins between organelles or from the plasma membrane to organelles by vesicular trafficking.[13] In this process, proteins force the membrane to bend to a positive curvature for the so-called budding of a vesicle. After scission of the vesicle, it is transported to the target cell compartment to be fused with the organelle membrane and release its cargo.[13] Temporal local curvature variations can also control the function of membrane proteins that are "solvated"[14] in the membrane. Membrane mechanical stress can activate protein's function and *vice versa* protein action deforms the membrane which in case of overlapping deformation sites of other membrane proteins can serve as signal pathway between proteins.[7]

Also, membrane-like structures are part of the lipid-based energy storage but in this case just a monolayer is needed because the core of the intracellular energy-storing organelles called lipid droplets is not aqueous. Instead, neutral lipids such as triacylglycerides (TGs) and CEs are stored here. As soon as energy is needed, this chemically stored fuel can be released by enzymatic cleavage of the FAs and subsequent beta-oxidation.[15]

Beside the passive roles of lipids, they directly affect protein function. PAs are negatively charged membrane parts and, for example, activate phospholipase A1 (an enzyme that breaks lipid *sn*-1 ester bonds[16]) by anchoring the enzyme in close vicinity to its PC and PE substrates.[17] In the abscisic acid (ABA) signaling pathway, PAs act as messengers in a signaling cascade. ATHB6 is a transcription factor protein that, after activation by another protein called ABI1, blocks the ABA signaling pathway. This effect is attenuated by PAs that bind ABI1 to the plasma membrane and prevent it to migrate from the cytosol to the nucleus where it would activate ATHB6. Zhang et al. proposed a signaling mechanism where ABA stimulates phospholipase D to produce PA that inhibits ABI1 and thus the activation of ATHB6 which consequently cannot block the ABA response.[18]

In addition to the examples in healthy organisms, lipids also play roles in disease and therefore lipidomic research could help in diagnosis, treatment and prevention of various physical disorders like cardiovascular disease and diabetes.[4]

1.2. Lipids in Diabetes and Cardiovascular Disease

Diabetes is one of the major global health problems with 537 million cases and 6.7 million diabetes-related deaths in 2021.[19] Two forms of diabetes are known: Type 1 diabetes is a consequence of an autoimmune attack on the pancreatic β-cells that are responsible for insulin production. Insulin is a hormone serving the transport of glucose from the blood to the cells of an organism. Disabled β-cells

and the resulting lack of insulin lead to high blood glucose levels (hyperglycemia) and without external insulin supply the patients would die. Type 1 diabetes is caused by a genetic defect and cannot be prevented, whereas the major diabetes type 2 with over 90 % of all diabetes cases develops more slowly and in an early stage prevention, delay or even remission is possible.[19] As of type 1 diabetes, β-cell dysfunction and hyperglycemia is the outcome of type 2 diabetes but the initial cause of the latter form of the disease is not a lack in insulin but a so-called insulin resistance predominantly of skeletal muscle and liver cells.[20] To balance this, β-cells increase insulin production but in later disease states fail to provide increasing levels of insulins.[19] Insulin secretion is controlled by β-cells that respond to variable demand signals like increased levels of glucose or free FAs resulting from e.g. fasting-feeding cycles. This control is impeded in type 2 diabetes and the combination of insulin resistance, impaired insulin secretion and a deficit in ß-cell mass and function leads to hyperglycemia.[21]

Lipids, especially the already mentioned free FAs are known key players in the etiology of insulin resistance. They play a signaling role in diabetes by activating the toll-like receptor 4,[22] which is a critical transmembrane receptor protein for the innate immune response because it regulates pro-inflammatory signaling pathways.[23] This inflammatory signaling is associated with insulin resistance and thus with type 2 diabetes.[22] Another lipid class playing a role in insulin resistance are diacylglycerols (DGs). Shulman and coworkers showed that liver and skeletal muscle cells of acetyl-CoA carboxylase 2 knock-out mice possess lowered DG concentrations, decreased activity of protein kinase C and increased insulin sensitivity. These findings are in line with the group's suggestion that DG accumulation activates a protein kinase cascade which in turn inhibits insulin signaling of another protein kinase. Consequently, DGs hinder the glucose uptake of cells.[24] Ceramides were also shown to impair the protein kinase-driven insulin signaling by two different mechanisms.[25] First, they are promoting the dephosphorylation and deactivation of the protein kinase called "Akt". Second, ceramides were observed to impede the Akt translocation to the membrane where it must be activated to enter the cytosol and subsequently stimulate the translocation of glucose transporter-4 from the cytosol to the membrane. Therefore, ceramides hinder the glucose uptake of the cell, that in healthy organisms is mediated by the named glucose transporter. Besides playing a role in insulin resistance, ceramides are involved in the initiation of β-cell apoptosis which is one of the major problems in diabetes. Ceramides trigger apoptosis by recruiting and activating pro-apoptotic proteins to increase the mitochondrial membrane permeability[25] for the electron carrier heme protein cytochrome c which is released in the cytosol to prompt the cell's suicide.[26]

Although many treatment approaches exist to improve the patient's quality of life, no therapy was able to cure the loss of β-cells.[27] Nevertheless, the development of type 2 diabetes can be delayed or stopped in an early prediabetes stage. This is possible by medication or even just lifestyle interventions

if the disorder is diagnosed very early. Diabetes is strongly correlated to obesity which is foremost because of the release of free FAs by adipocytes when their storage capacity is exceeded.[21] Beside losing weight by physical activity and a healthy diet (e.g. less sugar) also avoiding risk factors like sedentary lifestyle, excessive and deficient sleeping and consume of alcohol and tobacco, decreases the risk of diabetes. Because the lifestyle of many people, especially in western societies, fulfills at least some of the diabetes risk factors, a broad screening would assist early diagnosis and treatment.[28] Detailed diagnosis of disease type and state and individualized therapy is complex because diabetes can vary in symptoms or can be symptomless for a long time.[21] Diabetes studies mostly focus on genetics and proteomics. Lipidomic studies, on the other hand, predominantly investigate variations on the lipid class level like, for example, elevated concentrations of free FAs in plasma[28] or accumulation of TGs in skeletal muscle cells.[29] Although lipid class upregulation was shown to help diabetes prediction by using the TG-glucose index,[30] it is not clear which roles specific lipids and lipid isomers play on a molecular level. Pancreas, liver, skeletal muscle, kidney, brain, small intestine and adipose tissue are all part of developing type 2 diabetes, but little is known about how the lipid composition of these organs changes with progression of the disease.[28] Convenient lipidomics can improve the understanding of diabetes pathogenesis. This can help to find biomarkers for reliable prediction and diagnosis to prevent the development or track therapy success.[21,31]

In addition to the direct diabetes symptoms, diabetes patients often suffer from cardiovascular complications which are also the leading cause of death of diabetes.[21] Diabetes and cardiovascular diseases share risk factors such as physical inactivity, unhealthy diet (much salt, high fat and energy-dense food), obesity and consume of tobacco and excessive amounts of alcohol.[32] One part of the cardiovascular diseases is atherosclerosis. It is the process by that blood vessels of the cardiovascular system are blocked and cause myocardial infarction (heart attack) and stroke. The process starts in regions of turbulent blood flow i.e. vessel-bifurcations, -narrowing or -curvature where the concentration of low density lipoproteins (LDL) is increased by local recirculation.[33,34] Lipoproteins are macromolecular complexes, consisting of lipids and proteins and serve as lipid transporters in the blood.[35] Higher LDL concentrations let them pass the endothelial cells (interface between vessel-lumen and -wall) to enter the arterial wall where they are oxidized. This works as an initial trigger for the inflammatory reaction in the arterial wall that forces the endothelium surface to adhere white blood cells (especially monocytes). After transport of the monocytes into the wall and their differentiation to macrophages, they release pro-inflammatory proteins (so-called cytokines, chemokines and chemoattractants) and lipid mediators like lysophospholipids and FAs (especially arachidonic acid). At the same time, they excessively consume oxidized LDLs and are converted to lipid-laden macrophages, i.e., foam cells. The accumulation and apoptosis of foam cells lead to a lipid-filled necrotic core that is

separated from the blood flow by the so-called fibrous cap. To build that up, smooth muscle cells (SMCs) migrate between the necrotic core and the endothelium and produce collagen to serve as a matrix for the SMCs. As long as the fibrous cap protects the necrotic core of the atherosclerotic plaque, the artery is narrowed but not blocked. When the fibrous cap becomes thinner because of pro-inflammatory proteins that impede SMCs migration and collagen synthesis, plaque rupture can happen. In that process the lipids and inflammatory content of the necrotic core are exposed to blood which results in thrombosis and possibly in myocardial infarction or stroke, depending on whether the vessel supplies the heart (coronary artery) or the brain (cerebral artery), respectively.[32–34]

Like it was mentioned above, lysophospholipids play a role in the mediation of inflammatory response in atherosclerotic lesions. Lysophosphatidic acids (LPAs), for example, favor the above-mentioned recruitment and proatherosclerotic action of monocytes and SMCs.[36] LPAs stimulate: (1) the adhesion-molecule expression by endothelial cells to tether monocytes and let them enter the vascular wall, (2) the production of pro-inflammatory reactive oxygen intermediates, cytokines and arachidonic acid, (3) the lipid accumulation of monocyte-derived macrophages and foam cell formation[36], and (4) the dedifferentiation[37], proliferation[38] and migration[39] of SMCs.[40] Mast cells are immune cells known to accumulate in atherosclerotic plaques and to play a role in their destabilization and subsequent rupture.[41] LPAs were shown to be a factor in mast cell activation and to induce intraplaque hemorrhage (bleeding) which means that newly formed blood vessels in the artery wall release blood resulting in coagulation and thrombosis that can lead to plaque rupture.[42]

Similar to LPAs, also lysophosphatidylcholines (LPCs) were shown to have pro-inflammatory and atherogenic effects. Besides the promotion of monocyte migration, lipid uptake, release of pro-inflammatory proteins and conversion to foam cells, LPCs are major mediators of apoptosis of endothelial cells, monocytes and SMCs.[43,44] Considering that the choline group of LPCs is readily removed by the lysophosphatase D yielding LPAs, similar observations for the pro-inflammatory effects of LPCs and LPAs are predictable.[45] LPCs have also been linked to anti-inflammatory events, e.g. the mediation of cholesterol efflux from macrophage-derived foam cells.[46] As the excessive lipid consume of foam cells is a pivotal step of atherosclerosis, the inversion of it is a perfect example of the apparently ambivalent roles of LPCs. At the same time, it exemplifies the problem of a low level of specificity in the analysis of lipids. LPCs are a whole class of lipids that includes numerous distinct species differing in length and degree of unsaturation of their acyl chain, as well as the DB geometry and position. It has been shown that the influence of LPCs in inflammation can vary depending on the length and unsaturation of their hydrocarbon chain.[47,48] Hence, the lipid's structural variety is likely to be one reason for the ambiguous results concerning the roles of LPCs in cardiovascular diseases. Comprehensive lipid analysis resolving individual lipid species can help to understand cardiovascular

pathogenesis. Stegemann et al., for example, studied and compared the lipid content in plaque tissue and healthy artery tissue. They assigned 150 lipid species with resolution of their individual FAs and identified 24 lipids that were exclusively present in plaques.[49] Such lipidomics studies can reveal molecules that are of crucial importance for a disease and could serve as biomarkers or therapy target.

1.3. Lipidomics - Routine Analytic Methods and Current Challenges

Although lipidomics is a modern and still emerging research field[50,51], lipid analysis started earlier and some routine methods for it exist. Early lipid research relied on thin layer chromatography (TLC) and gas chromatography (GC) for the separation of lipid extracts based on polarity differences.[52] In general, chromatographic separation of an analyte mixture happens by ad- or absorption of the analytes by a stationary phase and subsequent elution of them by a mobile phase.[53] Due to distinct interaction of the analytes with the stationary phase, the elution time is analyte-specific and can lead to separation. GC employs a gaseous mobile phase and a liquid stationary phase whereas TLC is a so-called liquid chromatography (LC) method and works with a liquid mobile phase and a solid stationary phase. Instead of TLC, modern lipidomics primarily use column-based LC where a column is packed with the solid stationary phase material.[54] Three main modes are distinguished: Normal phase LC (NP-LC) and hydrophilic interaction liquid chromatography (HILIC) separate lipids based on their polarity. Reversed phase LC (RP-LC) separates based on the lipid's hydrophobicity. NP-LC and HILIC both employ polar stationary phases but whereas NP-LC is done with non-polar organic solvents for the mobile phase, HILIC uses water and water-miscible organic solvents. For analyte elution in NP-LC and HILIC, the proportion of polar organic solvents and water is increased, respectively. Thus, the retention and elution mechanisms differ but still the lipids are separated based on the polarity of their head group. HILIC is more commonly used for lipidomics than NP-LC because the aqueous mobile phase of HILIC is advantageous for the mass spectrometric detection of the separated lipids. In HILIC, the analytes are bound to the stationary phase by the name-giving hydrophilic interactions, i.e., dipole-dipole, H-bounding and electrostatic interactions. RP-LC relies on non-polar stationary phases and polar mobile phases. Hydrophobic interactions with the stationary phase lead to lipid separation based on their hydrophobic part, i.e., the length and degree of unsaturation of the FA residues, making RP-LC separation to some degree orthogonal to HILIC separations. The elution of analytes in RP-LC is done by increasing the percentage of non-polar organic solvent.[54]

Another separation method is ion mobility spectrometry wherein analytes are ionized and accelerated by an electric field to be then separated based on their mobility through an inert-gas-filled drift chamber.[55] As in the case of chromatography, ion mobility spectrometry introduces an analytical dimension because larger ions collide with more inert gas molecules than smaller ones and thus

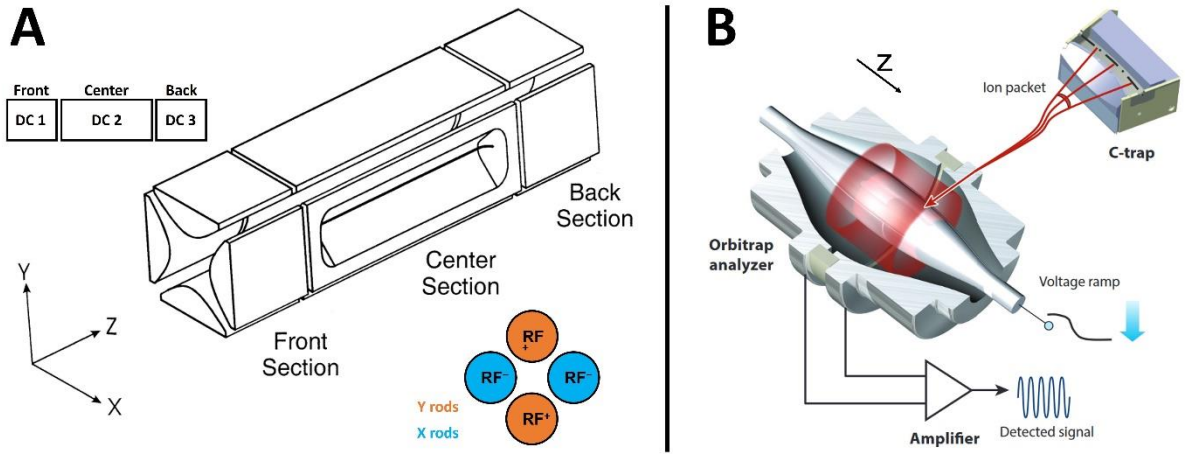

Figure 2: Instrumental and functional details of a (A) linear quadrupole ion trap and an (B) orbital trapping analyzer (Orbitrap). Reprinted with permission from (A) reference 58 © 2002 American Chemical Society and (B) reference 60 © 2015 Annual Reviews.

possess a longer drift time through the drift chamber. The so-called collision cross section (CCS) is an analyte-specific value that numerically reflects this phenomenon and is dependent on the shape, the size and the charge of e.g. a lipid ion.[55]

Using chromatography and ion mobility spectrometry, the lipidome can be separated but particular molecular species cannot be resolved. In contrast, the employment of mass spectrometry (MS), especially high-resolution MS allows to measure accurate mass-to-charge-number values (*m*/*z*) and to determine lipid's sum formula by comparison of accurate and theoretical *m*/*z*. The sum formula in turn provides information about the lipid backbone, head group and overall number of fatty acyl carbons and DBs.[4] Two of the most common MS instrument types are time-of-flight (TOF) and quadrupole ion trap mass analyzers. Measurements with TOF-MS are based on the *m*/*z*-dependent acceleration of ions by an electric field and the consequently *m*/*z*-dependent drift time in a field-free region.[56] The general principle of quadrupole ion trapping is to force ions to fly on stable trajectories between four hyperbolic electrodes that periodically switch between electrostatic attraction and repulsion with a defined radio frequency (RF).[57] In modern linear quadrupole ion trap mass spectrometers, the ions are trapped in a potential well of direct current (DC) and RF electric fields until they are resonantly ejected for detection. The well is created by an axial trapping DC field and a radial trapping RF field which are applied to the three sections (Front, Center, Back) of all quadrupole rods and pairwise to opposite rods (orange and blue), respectively (Figure 2A). The mathematical description of the potential well is given by Formula 1

$$\Phi = \frac{U+V\cos(\Omega t)}{r} \cdot (x^2 + y^2 - 2z^2) \qquad \text{Formula 1}$$

where U is the DC potential, V the RF potential with its frequency Ω, t is the time, r the distance from the central z-axis, and x, y and z are the three coordinate axes. With the so-called Matthieu equation,

two parameters (a, q) per dimension are obtained that allow to describe stability and instability of ion trajectories in quadrupole ion traps. The two parameters are given in Formulae 2 and 3

$$a = -\frac{8zeU}{mr_0{}^2\Omega^2} \qquad \text{Formula 2} \qquad\qquad q = \frac{4zeV}{mr_0{}^2\Omega^2} \qquad \text{Formula 3}$$

where $z * e$ is the charge and r_0 defines the trap size. As these equations define stable ion trajectories and contain the *m*/*z* ratio, it is possible to trap ions of certain *m*/*z* values by applying an appropriate combination of U and V when choosing a fixed alternating current (AC) frequency. In the trap, an inert gas is provided for low energy collision-induced ion deceleration to diminish the impact of initial axial velocity and thus focus the ions and reduce the dimension of the ion cloud. For the resonant axial ejection of ions, two phases of frequency-tunable (5-500 kHz) AC voltage are applied to the X rods. An AC-frequency sweep excites ions to radially exit the trap successively at their *m*/*z*-dependent resonance frequency.[58] The emitted ions are then, for example, destructively detected by a secondary electron multiplier or a channeltron. Alternatively, ions can be ejected in *z*-direction (Figure 2A) to be sent to another mass spectrometer like an orbital trapping mass analyzer.[56] Combining the axial ejection of a defined *m*/*z* range and sending the remaining ions to another mass analyzer enables tandem MS or multiple MS analysis (MS^n) detailed below in this chapter. The "Orbitrap" was invented by Alexander Makarov in 2000 and is much smaller (table-top size) and cheaper compared to the high resolution Fourier-transform ion cyclotron resonance instruments that require maintenance-intense cryomagnets.[59] Modern high field Orbitraps readily achieve mass resolutions of >200.000 whereas 2000 is considered already a high resolution for quadrupole ion traps.[56,60] In principle, the Orbitrap is constructed by an inner spindle-shaped electrode and two surrounding outer electrodes that match the shape of the central spindle (Figure 2B). After accumulation in a curved linear ion trap (C-trap) and ejection by a voltage ramp, ion packages enter the analyzer through a decentral orifice and are trapped in an orbiting motion around the inner electrode that attracts the ions while the outer electrodes repel them. Due to the decentral injection, the axial field component causes the ion "ring" to oscillate in *z*-direction. This oscillation does not depend on the initial ion velocity and the radial motion, but its frequency depends on *m*/*z* and induces an AC image current in the outer electrodes. By measuring and amplifying this current and Fourier-transforming the time-dependent signal, the axial oscillation frequencies of the trapped ions are translated into *m*/*z* values and ion counts, i.e., a mass spectrum.[56,60] No matter which mass analyzer is employed, MS requires ionization of the analytes, and soft ionization techniques like electrospray ionization[61] (ESI) and MALDI[62,63] are inevitable to mass spectrometrically investigate intact ions of biomolecules such as lipids.[56]

In ESI, an analyte solution is electrically charged and sprayed towards the mass spectrometer inlet by an inert gas flow. The spraying capillary and the inlet are counter electrodes with high voltages (Figure

3). In the positive-ion mode, the spraying capillary is positively charged and a so-called Taylor cone[64] is formed at the spraying capillary tip. Because of the high charge-carrier density per area at the cone tip a fine jet emerges. High charge density and strong Coulomb repulsion let small, charged droplets escape from the jet. While flying towards the mass spectrometer inlet, the droplet's solvent evaporates and the charge density rises. At the so-called Rayleigh limit[65], the droplets burst into smaller droplets which repeat that process until isolated gas-phase ions result.[66] Two mechanisms exist for the final step. In the so-called ion evaporation model, droplets with radii less than 10 nm directly emit analyte ions into the gas phase. This mechanism fits for small but not for large ions. Another model assumes the complete solvent evaporation from a droplet that contains only one large molecule. This molecule would inherit the charges of its droplet and the model is consequently called charge residue model.[66]

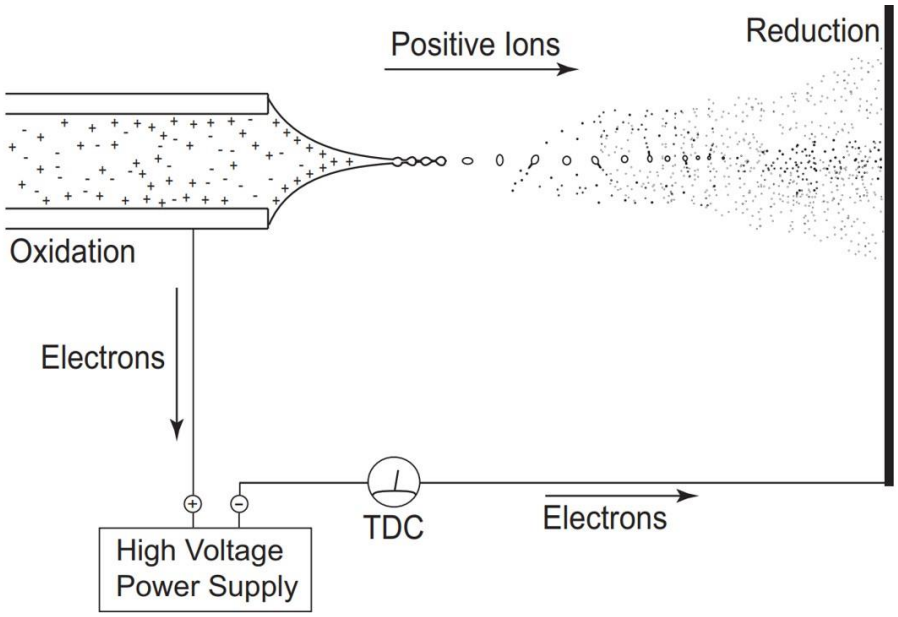

Figure 3: Depiction of the ESI instrumental setup for the positive-ion mode and processes leading to isolated ions by electrospraying. Reprinted with permission from reference 66 © 2009 Wiley.

Liquid samples like body fluids or organ tissue extracts can be analyzed by ESI-MS in two different ways. Either the solution is directly sprayed without prior separation[67] or the ESI source is coupled to a LC system (LC-MS).[54] Whereas the first approach called shotgun MS is faster, less laborious than LC-MS and needs only small analyte amounts, LC-MS comes with higher sensitivity and additional information. Shotgun lipidomics is susceptible to ion suppression effects. This means that lipids with a strong ionization tendency diminish the MS intensity of lipids that are harder to ionize. PCs, for example, suppress PEs. LC-MS can solve this problem and enables the detection of much more species by reducing spectral complexity.[54] Furthermore, the distinct retention or drift time of certain lipids is an additional analytical dimension that with the aid of standards can decipher lipid isomers.[55,68] These are compounds that have the same *m*/*z* but structurally differ in e.g. the fatty acyl composition, their

backbone attachment, DB geometry or DB position(s). Accurate *m*/*z* measurements of intact lipids and even LC-MS without lipid standards cannot resolve isomer structures. But with fragmentation methods, i.e., MS^n and by investigation of the resulting fragments, researchers can derive structural characteristics of the isomeric lipid precursors.[69] The most common fragmentation techniques are collision-induced dissociation (CID) and higher energy collision-induced dissociation (HCD).[1] Here, analytes gain internal energy by collisions with inert gas molecules/atoms until the energy suffices for the fragmentation of any bond. Consequently, the energy is consumed in low-energy dissociations before molecules can accumulate enough energy for higher energy fragmentation paths.[70] Thus, the major fragmentation sites in phospholipids are the ester linkages from the lipid backbone to the head group and the FAs. Resulting fragment ions and the corresponding neutral losses allow to identify the head group and determine the length and unsaturation of individual FAs.[71] Unfortunately, common collisional fragmentation is blind to *sn*- and DB-position isomerism.

1.4. Isomer-resolved lipidomics

The more precisely lipid structures are resolved, the more readily researchers can draw conclusions about biochemical roles of lipids. Also, more specific biomarkers can be found to, for example, assist medical diagnosis. In order to resolve lipid isomers, many MS approaches have been tested, including alternative fragmentation techniques, analyte derivatization and the combination of both.[69] The goal of alternatives to CID is to introduce high energy fragmentation paths. This is done by introducing more energy than CID or introducing energy more specifically to the bonds to break. One way to activate ions with more energy per hit than with collisional techniques is ultraviolet photodissociation (UVPD).[70] Instead of exciting molecular vibrations like infrared multiphoton dissociation (IRMPD) and CID, UVPD excites a molecule to electronically excited states to open new fragmentation channels. Whereas IRMPD is based on the absorption of multiple IR photons, in UVPD molecules can be fragmented by the absorption of a single UV photon. Using a 193 nm UV laser, members of the Brodbelt group discerned DBPIs of PCs on the basis of diagnostic carbon chain fragment ions that are not found in CID-MS^2 spectra.[72] In later publications they combined HCD and subsequent UVPD in a MS^3 experiment. Therein, an initial collision-induced head group loss led to ring closure between the glycerol backbone and the carbonyl oxygen of the *sn*-2 FA to form five-membered dioxolane rings. Subsequent UVPD caused cross-ring cleavage and selective detachment of the *sn*-2 FA which served the *sn*-isomer analysis of various GPs (PCs, PEs, PAs, PSs, PIs, PGs and cardiolipins).[73,74] The Reid group extended DB fragmentation by UVPD to sphingolipids wherein the sphingosine DB as well as FA carbon chain DBs were elucidated.[75] Becher et al. could show that the attachment of PCs with iron (II) cations improves

the UVPD selectivity for the *sn*-2 FA, which has been used for the relative quantification of *sn*-isomers.[76]

Electronic excitation is also possible by electron-induced dissociation (EID). In contrast to CID, electron activation leads to FA carbon chain fragments and was used to distinguish DB isomers of PCs[77], SMs[78] and TGs[79]. Similar to UVPD, EID has been shown to selectively yield *sn*-1-fragments enabling *sn*-isomer distinction for PCs[77] and TGs[79]. In addition, Baba et al. could show that the mechanisms of radical carbon chain fragmentation differ between E- and Z-DBs. Resulting diagnostic fragment ion intensities were used to uncover DB geometry and resolve E/Z-DB isomers of PCs, SMs and TGs.[80] Another fragmentation alternative for radical carbon chain fragmentation is metastable atom-activated dissociation and its benefit for revealing DBPIs has been shown by Deimler et al.[81]

Instead of altering the fragmentation technique, analytes can be derivatized to add functionality and/or to open alternative fragmentation paths. For radical-directed dissociation (RDD), Pham et al. added functionality to lipid analytes by supplementing the ESI spraying solution with iodine-substituted derivatives of benzoic acid that provide highly reactive radicals after photoactivation. Subsequent CID of the radical species allows the investigation of DBPIs in GPs, SMs and TGs[82,83] and of epimers in glycosphingolipids.[84] The Xia group showed that RDD is also possible without photoactivation using only the more available collisional activation. They used bicarbonate as ESI-solution additive, forming adducts of PCs wherein the *sn*-2 FA can selectively be detached and the FA chains can be fragmented to infer *sn*-isomers[85] as well as sites of unsaturation and chain branches.[86] Recently, they presented another radical precursor that was attached to the amine group of PEs by offline derivatization (vortexing at 50 °C for 60 minutes) prior to ESI-MS analysis. This has been used to study the positions of cyclopropanation, methylation and DBs in the FA chains of bacterial PEs.[87] Derivatization can also be done inside the mass spectrometer avoiding laborious sample preparation steps, as shown by Blanksby, McLuckey and coworkers: Negative-ion mode CID of GPs liberated the *sn*-1 and *sn*-2 FAs that were subsequently charge switched in an ion/ion gas-phase reaction with tris-phenanthroline magnesium dications inside a linear quadrupole ion trap. Positive-ion mode CID of the charge-switched products led to DB dissociation.[88]

Opening alternative fragmentation paths for certain moieties has been done by selective functionalization, yielding features that were readily fragmented by the used dissociation method. For example, the epoxidation of lipid DBs forms strained three-membered epoxide rings that can be fragmented by CID. Utilizing the common epoxidation reagent mCPBA, this approach suffers from long reaction times (incubation at 50 °C for 60 minutes).[89] Cao et al. therefore applied a helium-sustained low-temperature plasma (LTP) onto lipid solutions in acetonitrile and reached >90% of LTP-triggered

epoxidation after 2 minutes.[90] In a recent publication, another approach was presented using the reactive oxygen that is produced in an ambient corona discharge between the inlet of the mass spectrometer and the sample-containing glass capillary to which a high voltage of 4 kV was applied.[91] Lipid DBs were also pinpointed by the aid of a functionalization with the common reagent chloramine-T. It reacts with lipid DBs in 15 seconds of vortexing to form aziridines which are the nitrogen-analogues of epoxides and can be fragmented by CID.[92]

One of the most commonly used DB derivatization techniques is ozonolysis or ozone-induced dissociation (OzID) introduced by Blanksby and co-workers.[93] In OzID, lipid ions are trapped in an ozone-filled ion trap where lipid DBs are ozonolyzed, i.e., lipid DBs are fragmented. OzID can be combined with CID to unveil *sn*-isomers: After CID-caused head group loss, the resulting fragments are further dissociated by OzID which selectively detaches the FA in *sn*-2 position.[94] In a large scale OzID study of breast cancer tissue, Young et al. uncovered unusual lipid DBPIs, revealing an aberrant activity of the fatty acyl desaturase 2 (FADS2). Employing gene silencing and stable isotope tracing, the authors found high plasticity of FADS2 in terms of substrate acceptance and the desaturation site.[95]

Another widely used DB functionalization is the photochemical PB reaction[96,97] between a carbonyl C=O and a C=C bond within a lipid, forming a strained four-membered oxetane ring.[98] Mechanistic considerations are depicted below (Scheme 1) and include three possible pathways.[99] They share the initial step of photoactivation of a carbonyl's electron to an excited singlet state. Next, the excited molecule can either directly react with the C=C to form a singlet diradical ^{1}D (red in Scheme 1) or can first undergo intersystem crossing (ISC) to an excited triplet state to subsequently react with the C=C. The latter case results in the same triplet diradical ^{3}D (blue in Scheme 1) as ISC of ^{1}D stemming from the first path. Electron recombination of ^{3}D can happen via cyclization or loss of the new bond forming an oxetane or recover the substrates, respectively. According to computational research, the third

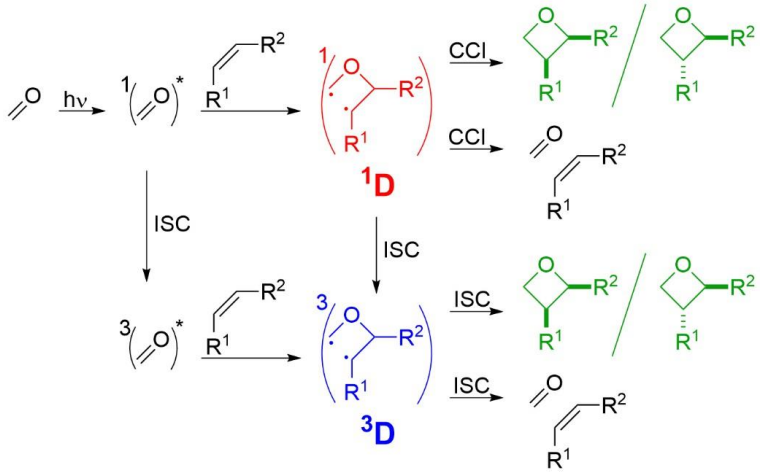

Scheme 1: Main mechanisms of the Paternò-Büchi reaction.

possible pathway is crossing a conical intersection (CCI) which directly leads ^{1}D to the oxetane or the substrates.[100] Phenylic carbonyls stabilize the diradical intermediate, causing long lifetimes that allow bond rotation and in turn the loss of the alkene's E/Z stereochemistry (see green in Scheme 1).[99]

In the lipid functionalization methodology introduced by the Xia group in 2014, lipid solutions in 1:1 water:acetone are electrosprayed by nanoESI while the capillary is irradiated with UV light to activate acetone for the PB reaction. To date, the PB strategy has been further developed, combined with other techniques and applied to many different sample types like various mammal organs,[101–103] algae,[104] fish,[105] in vivo samples, plant seeds and human tissue after surgical removal.[106] Combining the PB method with HPLC reduces the MS data complexity, can resolve constitutional isomers[104] and enables large-scale lipidomic studies on the DBPI level.[103] For post-HPLC-column derivatization, the eluent was duct through a UV light-irradiated capillary before being sprayed by ESI. Comparing DBPI ratios in healthy and cancerous human breast tissue and in plasma samples of healthy and type 2 diabetes infected individuals, Zhang et al. discovered significant changes that can serve as biomarkers for disease diagnosis.[103] In another study, the PB method was combined with a liquid microjunction surface sampling probe that desorbs lipid analytes directly from tissue before they are functionalized by passing an UV light-irradiated capillary and subsequently get analyzed by ESI-MS^2.[107]

In addition to acetone, other PB reagents were tested to enhance the ion yield and derivatization yield and further functionalize the lipids. The PB attachment of acetophenone, e.g., introduces a chromophore in direct vicinity to DBs, enabling their cleavage by UVPD with higher selectivity than CID.[108] Installation of the basic 3-acetylpyridine (3-AcPy) can boost the detection of hard-to-ionize compounds (TGs, hexen, cyclohexene, CEs and FA esters) and can switch the charge of FAs that are preferably detected as negative ions.[109] Simultaneously, the attachment of the isomer 2-AcPy paves the way for *sn*-isomer analysis of GPs in CID-MS^3 experiments.[110] Initial head group loss results in a dioxolane which is favorably fragmented by cross-ring cleavage, yielding fragments lacking the *sn*-2 FA. Independent of their *sn*-position, unsaturated 2-AcPy-bearing FA fragments experience the strong 2-AcPy-caused intensity boost. Therefore, these 2-AcPy-functionalized fragments dominate the spectra, negating the favored detection of *sn*-2 fragments. Accordingly, depending on whether the unsaturated FAs were attached to the *sn*-1 or *sn*-2-position, the dominant fragments are products of cross-ring cleavage or not.[110] With the assistance of an iridium-based photocatalyst, Feng et al. were able to use a visible-light-induced PB functionalization with methyl benzoylformate (MBF) to distinguish DBPIs and E/Z-isomers. After visible-light excitation of the photocatalyst, it activates MBF by triplet-energy transfer to efficiently react with lipid DBs (PB yields up to 72%). In course of PB derivatizations, Z-isomers readily undergo isomerization to the corresponding E-isomers. Because E-isomers elute slower than Z-isomers, a new peak with a longer retention time appears in chromatograms of Z-isomer

samples after PB functionalization. Comparing pre- and post-functionalization chromatograms enables E/Z-isomer resolution, because the PB functionalization of E-isomer in contrast to Z-isomer samples yields no or very low additional chromatographic peaks.

Lipidomic studies mostly analyze tissue or body fluid extracts, containing the lipid content of tens or even thousands of cells because the work with smaller amounts is challenging in terms of sample handling and instrumental sensitivity. Consequently, most lipidomic studies are blind for intercellular heterogeneity. In contrast, Li et al. published a DBPI- and *sn*-isomer-resolving single-cell shotgun lipidomics workflow, combining their PB and bicarbonate strategies with cell fixation and droplet-assisted nanoESI.[111] The cell fixation prevents cell lysis caused by the chemical conditions of the PB preparation step. Cell lysis would otherwise threaten the cell integrity and consequently single-cell analysis. For droplet-assisted nanoESI, solvent droplets are applied to the nanoESI tip to achieve a better analyte extraction of the single cells. Using the described method, single cancer cells were annotated to being either drug-sensitive or drug-resistant, based on quantitative DBPI and *sn*-isomer analysis.[111] This example highlights the potential of accepting the challenge of probing local biomolecule concentrations. Another technique that, on the one hand, already routinely probes local biochemistry and, on the other hand, still develops, is MALDI-MS and is discussed hereafter.

1.5. MALDI-MS

In laser desorption/ionization MS (LDI-MS) experiments with several amino acids, Karas and Hillenkamp discovered that mass spectra of tryptophan at its threshold laser irradiance possess higher ion yields at lower fragmentation than other amino acids. Additionally, LDI-MS of tryptophan-alanine mixtures at the tryptophan threshold irradiance yielded tryptophan and alanine peaks although the threshold of alanine is higher by a factor of ten. These observations were interpreted to be caused by a matrix effect of excess tryptophan that absorbs the laser energy and assists the soft ionization of alanine.[63] This finding initialized the research field of MALDI-MS. Beside the advantage of higher MS intensities, utilizing matrices also ensures the soft ionization of large, fragile biomolecules to get intact molecular ions with little or no fragmentation.[62,112] In 1988, Tanaka et al. introduced their so-called "ultra-fine metal plus liquid matrix method" using cobalt particles of 30 nm diameter and glycerol as matrix to achieve ions of proteins and polymers up to m/z 100,000.[113] In more detail, the "assistance" of the matrix is to isolate analytes from each other in a solid solution, to provide charge carriers and to absorb and mediate laser energy for a soft and nondestructive phase transfer (desorption) and ionization. MALDI-MS rapidly developed and was optimized by, for example, testing various matrices,[114] varying the laser wavelength,[115] and installing an additional laser for post-ionization.[116]

Even though MALDI-MS is routinely used in laboratories today, the processes after laser irradiation of the sample are still not fully understood. Because understanding desorption/ionization helps to optimize MALDI workflows in terms of e.g. sensitivity, reproducibility and reliability, the mechanism was studied extensively and various models were developed.[117] Early work investigated wavelength dependence,[118] the role of photoionization and photochemistry[114] and angular-resolved initial velocity distributions of desorbed material.[119] Although the acronym "MALDI" is set, the choice of the term "desorption" is still discussed because it suggests a thermal phase transfer of individual molecules from the surface of the sample. This is in contrast to the also proposed explosive ejection of clusters composed of matrix and analyte molecules.[120] Nowadays, it is consensus that after material ablation and initial charge separation there is a so-called MALDI plume. This plume is characterized by high temperatures and still high particle densities and consequently it is the location of secondary processes that most likely lead to the ions that are finally detected by MS.[117] Within this two-step framework it is still under debate how the primary ions are formed and which secondary reactions proceed in the plume. As MALDI is a photoinduced process, it is intuitive to assume a photochemical ionization, but direct photoionization of electronically excited matrix molecules cannot be the basis because the ionization potentials are higher than the energy of absorbed photons, regardless of whether considering ultraviolet (UV) or infrared (IR) light. Instead, observed photoionization products were explained by multiphoton ionization based on energy pooling. Here, the energy of multiple excited molecules is shared in favor of one molecule to reach a higher excited state above the ionization limit, whereas the others transition into a lower lying electronic state in this collective process.[114] Chromophores are known to strongly interact with other chromophores in spatial vicinity. Therefore, energy pooling in the diffusely excited solid is much more likely than the multiple excitation of one molecule.[121] Another mechanism assumes excited-state proton transfer (ESPT) from excited matrix molecules to ground state analyte molecules which is promoted by an increase of matrix acidity or basicity as a consequence of electronic excitation. Although this chemistry was observed for some compounds, common matrices did not show ESPT-activity[114] and known ESPT-active compounds failed as MALDI matrices. Consequently, ESPT is not considered to significantly contribute to the ionization process in MALDI.[121]

Photoionization also plays an essential role in a third model regarding the finally detected ions as lucky survivors of charged matrix-analyte clusters that are desolvated by direct evaporation of neutrals or indirectly after neutralization reactions.[122] According to the lucky survivor model, the liquid solution charge states of analytes are preserved in the "solid solution" i.e. the matrix. The photon energy absorbed by the matrix leads to desorption of preformed ions as clusters including analyte- and matrix-molecules and -ions as well as corresponding counterions. But some clusters statistically occur with an

excess or deficit of cations or anions. Excess energy of the highly excited clusters facilitates (1) neutralization reactions with matrix ions and/or by proton- and electron-transfer and (2) the desolvation of neutral species finally yielding (luckily surviving) isolated ions in the gas phase.[123] Instead of cluster reactions, the energy pooling-based "coupled chemical and physical dynamics model" (CCPD) takes secondary reactions between free molecular species in the hot dense plume into account.[124] Here, analyte ions are produced by collisions of analyte neutrals with photoionized matrix.[125] Conceivable matrix ion species are matrix radical cations ($m^{\bullet+}$), protonated/deprotonated matrix ($[m+H]^+/[m-H]^-$) and metal-cation adducts of the matrix ($[m+Me]^+$). Electron transfer from neutral analytes to matrix radical cations is only likely if the analyte's ionization potential is lower than that of the matrix. Otherwise $m^{\bullet+}$ is converted to $[m+H]^+$ by detaching a hydrogen from a neutral matrix molecule. Secondary reactions forming analyte ions are predominantly protonation, deprotonation and cationization.[121]

A central phenomenon of MALDI-MS is the dominant detection of singly charged ions. Even for large molecules wherein spatial distance can stabilize multiple charges and in the case of adducts with divalent cations, charge numbers exceeding one are almost completely absent in MALDI-MS spectra.[125] Regardless of the model applied, charge reduction takes place as secondary reactions in the plume i.e. proton- or electron-transfer processes. According to the lucky survivor model, the electron capture cross section is the reason for the exclusive survival of singly charged ions.[122] Supported by their higher cross section, multiply charged clusters more efficiently trap electrons stemming from photoionization of other clusters or the metal below the sample.[126] The CCPD postulates collision-induced proton- and electron-transfer reactions of multiply charged ions with neutral matrix molecules[125] or adduction with deprotonated matrix anions.[121]

Another typical MALDI phenomenon is that matrix ions can be suppressed completely if analyte concentrations are sufficiently high.[119,125] Besides on the analyte concentration, the matrix suppression effect also depends on the laser fluence as follows: Higher fluence needs higher analyte concentration to suppress the higher number of matrix molecules being photoionized.[124] In the lucky survivor model, the analyte concentration dependance is explained by the need of at least one acidic/basic analyte molecule per charged cluster that can claim the charge.[123]

Lower MS abundance of negative compared to positive ions are widely observed in MALDI-MS.[122] Karas et al. proposed that this is a result of adduct interactions being weaker for anions compared to cations (e.g. Cl^- versus Na^+, K^+). Further, they argue that anions are less basic than most analytes and therefore will "survive" instead of deprotonating an analyte molecule. The high mobility of electrons is considered another reason for low negative ion abundance as this leads to their rapid loss from the

plume, preventing negative ion formation. Moreover, photoionization of clusters is named as a possible explanation for higher positive-ion abundances because it yields positive charges and electrons. Whereas electrons rapidly leave the plume, positively charged clusters are far less mobile and remain available for secondary processes yielding isolated positive ions in the gas phase.[122]

In contrast to the models discussed above, the thermal ionization models assume thermal equilibrium or quasi-equilibrium for the ionization processes. Early examples are the reports of Chait[127] and Beavis[128] postulating the polar fluid model in that the matrix aids the charge separation as a polar solvent. The matrix is electronically excited and electronic energy is converted to vibrational energy by non-radiative processes. Vibrational, i.e., thermal energy, leads to melting of the matrix. For a short period, the matrix serves as a hot polar solvent for molecules to frequently collide and react in thermal protonation and deprotonation reactions that produce ions. Equilibrium is reached before matrix- and analyte-neutrals and -ions are desorbed to the gas phase. In detail, the reactions are autoprotolysis, proton disproportionation and proton transfer to/from analyte neutrals from/to protonated/deprotonated matrix ions:[129]

$$2\ m \rightleftharpoons [m+H]^+ + [m-H]^- \qquad 2\ A \rightleftharpoons [A+H]^+ + [A-H]^-$$

$$m + A \rightleftharpoons [m+H]^+ + [A-H]^- \qquad m + A \rightleftharpoons [m-H]^- + [A+H]^+$$

$$[m+H]^+ + A \rightleftharpoons m + [A+H]^+ \qquad [m-H]^- + A \rightleftharpoons m + [A-H]^-$$

Questions of thermal equilibrium are not addressed in the lucky survivor model, but are commented by the CCPD as relying on primary ion formation by energy pooling and secondary ionization in the plume.[124] These secondary analyte ionizations can proceed to local thermal (quasi) equilibrium if molecules undergo a sufficient number of collisions before reactions are interrupted by physical expansion and ion extraction by applied electric fields.[125] However, thermal equilibrium was concluded to be unlikely. On the one hand, reverse reactions of analyte ionizations are considered to be too slow to reach equilibrium in typical MALDI time scales. On the other hand, ions with varying formation energies were observed in comparable abundances which is in conflict with thermal equilibrium.[124]

In experiments with a deuterated matrix, Jaskolla et al. evaluated the role of preformed ions and gas-phase protonation/deuteronation in MALDI.[130] Exclusive analyte ionization in the gas phase would produce only deuteronated signals, whereas exclusive desorption of preformed ions would result in only protonated signals. Variation of the sample preparation pH and the laser fluence suggest a mixture of both mechanisms. At lower pH values, higher signals of protonation were observed emphasizing the role of preformed ions. In contrast, deprotonation-derived signals were more abundant at higher laser fluences, indicating an increased role of gas-phase reactions.[130]

1.6. MALDI-MS imaging

After over 35 years since the first MALDI experiments, the detailed MALDI mechanism is still discussed but nevertheless MALDI is routinely used as a reliable method in bioanalytical chemistry. In addition to being a soft ionization technique, MALDI comes with the advantage to extract the content of a small sample region with diameters in the micrometer range. MALDI-MS imaging (MALDI-MSI), introduced in 1994 by Spengler et al.[131], uses the micrometer accuracy of the ablation by a highly focused laser beam for the pixel-by-pixel scanning of a sample acquiring a mass spectrum for each pixel (Figure 4). Subsequent plotting of the MS intensity (I) of a certain *m/z* signal in a color or gray scale for every pixel in the scanning raster (x, y, z coordinates) yields an image of the analyte distribution in, e.g., a biological tissue sample.[132] How accurate MALDI-MS images reflect the real biological distributions, is affected by, for example, sample heterogeneity (physical or chemical), sample preparation, the matrix choice and ion suppression effects.[133–136]

As described for matrix ions, also the detection of analytes is suppressed when other analyte molecules, competing for charge, are more effectively ionized. This was shown for various analyte classes[133,134,137–139] but one prominent example is the ion suppression exerted by PCs in lipidomics studies.[136] In the positive-ion mode, the ionization affinity of PCs is higher than that of PAs, PEs, PGs and PSs, hindering their positive charging, whereas the latter species cause lower PC-derived signals in

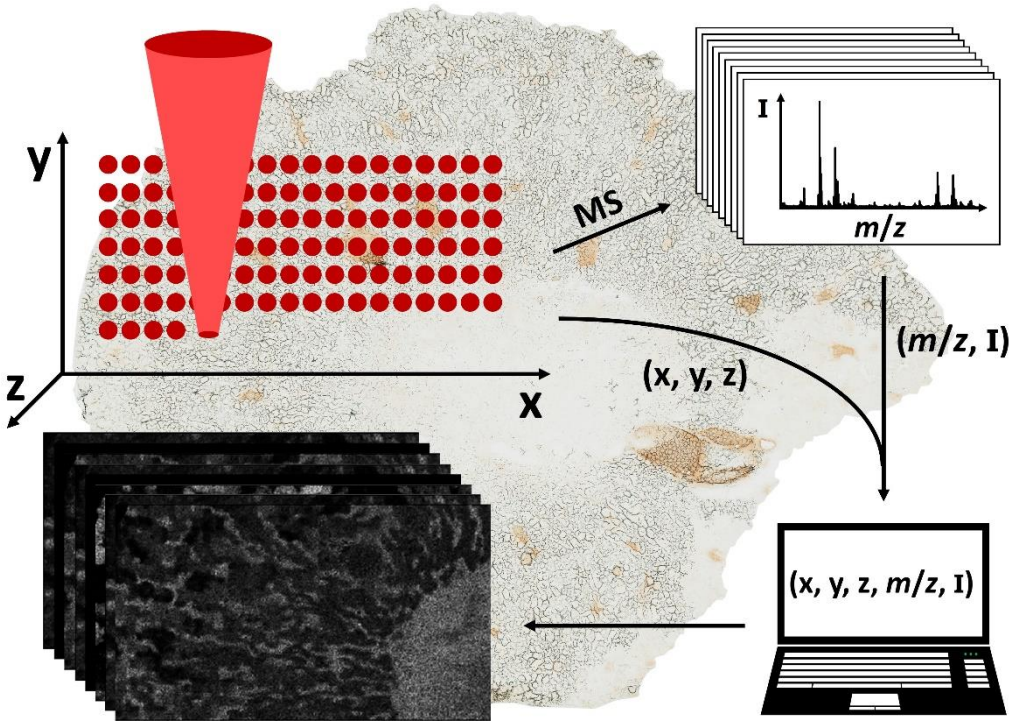

Figure 4: General workflow of MALDI-MSI experiments. For every pixel with the spatial coordinates x, y and z, a mass spectrum is recorded providing *m/z* and intensity (I) values. Plotting I in a color or gray scale for every pixel yields lateral distribution images like at the bottom left.

the negative-ion mode. At the same time, PCs were observed to boost the negative-ion intensity of PEs, PGs, and PSs, most likely by promoting deprotonation or cation detachment from the other lipids.[136] This showcases that MALDI-MSI results can be compromised by ion suppression effects. If, for instance, PCs are endogenously upregulated in a certain tissue area, mass spectrometric PE signals will be reduced there even though the biological PE-distribution would be homogenous throughout the whole tissue.

Local (bio)chemical and physical sample conditions also influence MSI results. Alkali metal adduct ions are part of the most common lipid signals in MALDI-MSI of biological tissues.[140] Local presence of alkali metal cations interferes with the signal intensity of protonated lipids from the same location.[141] This problem can be solved by washing the sample with ammonium acetate or ammonium formate solutions.[142] Sample preparation steps can thus help to overcome imaging issues but also can cause problems as exemplified by the impact of divergent analyte extraction and incorporation into matrix crystals. The analyte migration and co-crystallization with the matrix is crucial for efficient ionization by MALDI and can vary between analytes and sample preparation strategies.[143,144] Matrix application for imaging experiments is most commonly conducted by spraying (electro, ultrasonic, vibrational or pneumatic spray) or sublimation/recrystallization. Utilizing pneumatic spraying, highly concentrated matrix solutions (almost saturated) are nebulized by a vigorous inert gas flow and sprayed onto the sample. Under optimized conditions, the sample is slightly wetted providing the possibility for analytes to be extracted and to co-crystallize with the matrix while preventing wash-out effects. No solvent is used if the matrix is applied by sublimation onto the sample surface. To ensure co-crystallization though, the matrix is forced to recrystallize by exposure of the matrix-coated sample to a solvent-saturated atmosphere.[143] Besides ensuring co-crystallization and avoiding analyte delocalization, the matrix amount must be carefully controlled. This is because thick coating will cause analyte suppression and insufficient coating will diminish the “softness” of ionization when MALDI is locally replaced by the harsh LDI. Scanning electron microscopy experiments revealed that the structure of matrix-analyte co-crystals on top of various biological tissues changes with varying morphology of the tissue.[145] In short, the quality of the MALDI matrix varies depending on the used method and the tissue type. A recent work of the Soltwisch group, for example, employed laser microdissection of histological regions of mouse cerebellum that were defined on basis of MALDI-MS images to extract the lipids of the released material and analyze it by quantitative LC-MS. Comparison of the MALDI-MSI and the LC-MS results unveiled discrepancies between the lateral distribution displayed by MSI and the enrichment and depletion found by LC-MS.[146]

Choosing a matrix for a MALDI-MSI experiment influences the analyte species that can be imaged. Some matrices specifically perform in the negative- or the positive-ion mode whereas others can be

used in both ion modes. Most matrices are low-molecular-weight compounds. So, a matrix ion signal background can disturb the detection of low molecular weight analytes in metabolomics if the mass spectrometer cannot resolve matrix and analyte peaks. Nevertheless, matrix cluster ions can interfere with higher-weight analyte ion signals too. The most commonly used matrices in lipidomics (Scheme 2) are 2,5-dihydroxybenzoic acid (DHB), α-cyano-4-hydroxycinnamic acid (CHCA), 9-aminoacridine (9AA), 1,5-diaminonaphtalene (DAN), 2,5-dihydroxyacetophenone (DHA), and sinapinic acid (SA).[132,147,148] Perry et al. recently evaluated how the lipid profiles acquired by MALDI-MSI of mouse liver tissue depend on the employed matrix. Applying five commonly used matrices, variations have been found concerning the lipid coverage, the preferred ionization of certain lipid subclasses and the patterns of proton, sodium and potassium adducts. One matrix tested in this study is DAN and it showed a special reactivity with phosphatidylcholines. It detaches a methyl group from the choline head group, yielding molecules with the same *m/z* value as a PE with two more acyl chain C-atoms than the original PC, i.e., the ion signal of $[PC\ 34:0-CH_3+H]^+$ is erroneously annotated as $[PE\ 36:0+H]^+$.[148]

Due to the fact that every biological sample is different, ion suppression and other confounding factors are not constant. This is important to note for MALDI-MS image interpretation. As these factors are difficult to predict, quantification via MALDI-MSI requires internal standards that, for example, are spotted on top of or beneath the tissue.[149,150] The use of internal standards is more easily done in desorption electrospray ionization (DESI) and nanospray desorption electrospray ionization (nanoDESI) MSI experiments where the analytes of a sample are desorbed by applying a solvent mixture as electrospray or "permanent droplet", respectively.[151,152] Simple incorporation of internal standards in the applied solvent mixture enables quantitative analysis.[153] In so-called droplet pick-up mechanism of DESI, the impacting electrospray desorbs secondary droplets from the sample that is already wetted by the sprayed solvent mixture. These secondary droplets contain charged analytes and undergo ionization as discussed for ESI. In nanoDESI experiments, a solvent-delivering primary capillary, the

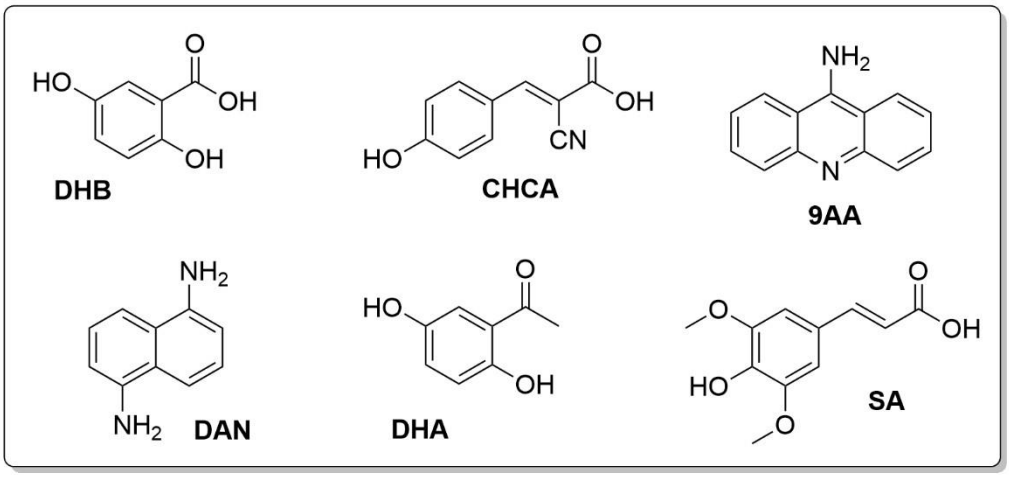

Scheme 2: Examples of MALDI matrices that are most commonly used in lipidomics studies.

sample and a nanospray capillary are permanently bridged by a solvent mixture droplet. The analyte solution produced by constant solvent application onto the sample is sucked and electrosprayed by the nanospray capillary.[154] Ionization is again similar to the ESI mechanism. DESI and nanoDESI offer the advantage that no sample preparation is needed but even with specialized equipment, nanoDESI provides lateral resolution down to 10 µm pixel size[154] which is better than DESI (typical larger than 20 µm)[155–157] but still not in the range of MALDI-MSI.[158,159]

The lateral resolution in MALDI-MSI is limited by the laser focus diameter, the matrix crystal size and the amount of ablated material that can be ionized without fragmentation and transferred into the mass spectrometer as intact molecular ions. Kompauer et al. developed a MALDI source employing a focused laser beam and optimized the sample preparation for small matrix crystals to enable lateral resolutions down to 1.4 µm.[158] Because smaller pixels mean less desorbed material, a high ionization yield is desirable. Soltwisch et al. used laser-induced post-ionization to address this.[160] In their so-called MALDI-2 setup, a second laser fires into the desorption plume created in the MALDI event with the aim to increase the ionization of desorbed material. In a recent study, the authors introduced transmission-mode MALDI-2 in which the sample is penetrated by laser light from the backside through a UV-transparent sample holder.[159] With this setup they achieved a pixel size of 0.6 µm. Another favorable effect reported for MALDI-2 is that the above-mentioned suppression exerted by PCs is mitigated.[146] Smaller pixels at constant overall image size mean more pixels and longer acquisition times. Scanning a particular area with a 1 µm pixel size needs 16 times more pixels than a scan with 4 µm pixels. Typically, the following sequence is used for MALDI-MSI measurements: move to a defined sample location, fire the laser, acquire a mass spectrum, and repeat this procedure. The time per pixel has been dramatically reduced by using a rapidly firing laser while continuously moving the sample stage and simultaneously acquiring mass spectra.[161] In the conventional spot mode, only a part of the pixel's material is ablated, but by moving the stage in a small zigzag pattern while the laser fires with maximum repetition rate, the material of the full pixel can be used.[161] Non-planar samples are challenging because they run out of focus if they are not refocused on spots of a differing height. An autofocusing MALDI source developed by the Spengler group utilizes a laser triangulation system with a camera that recognizes the lateral position of a second laser that is calibrated to cross the laser beam in its focus plane. If the system is in focus, the autofocus laser irradiates the spot-to-measure. If the laser is missing the spot, the sample stage corrects its *z*-position and resolves height variations down to 1.5 µm.[162]

Besides simple matching of spatial coordinates with *m*/*z*-intensity data pairs, some *in silico* corrections are common practice in MSI data processing.[163] Normalization of the signal intensity to the total ion count (TIC), a certain matrix or analyte signal, or an internal standard signal is used to compensate for

artifacts stemming from sample heterogeneity, matrix hot spots or poor sample preparation. In order to assign *m*/*z* signals with higher mass accuracy, post measurement *m*/*z*-recalibration is applied by correcting all signals on the basis of the deviation of a known signal from its theoretical *m*/*z* value.[163] Mirion[164] and MSIreader[165] are visualization tools translating the raw data into MS images. The tools can also produce overlay images of several *m*/*z* channels (in distinct color scales) or by superimposing microscopic and MS images. Moreover, regions of interest can be defined in the images to let the software extract underlying spectra and peak lists. Nowadays there are many MSI processing tools (ImageQuest (Thermo Fisher Scientific),[166] SCiLS (Bruker),[167] High Definition Imaging (Waters),[168] SpectralAnalysis,[169] EXIMS,[170] massPix[171]) including some that offer more complicated data analysis like, e.g., principal component analysis and other statistical methods for multivariate data analysis.[163] One example that highlights the advantage of common data formats (imzML[172]) in combination with a big database to store and share MSI results is METASPACE.[173] Researchers can upload their MSI data to the platform subsequently outputting MS images that are already assigned to metabolites and lipids from databases. In that course, images of isotopic species are excluded and the adducts (e.g. Na^+ or K^+ adducts) of particular species are grouped in overviews. Assignments are evaluated by a so-called metabolite-signal match score (MSM) that considers spatial chaos, the similarity of measured and theoretical isotope patterns, as well as the similarity of isotope signal images. Basically, spatial chaos is measured by calculating if the image is structured or displays a random distribution of spectral noise.[173]

With the aid of sophisticated data analysis, MALDI-MSI is a powerful tool for targeted or non-targeted bioanalytical studies to gain insight into biochemical processes by investigating local relative concentrations in biological samples. This has been demonstrated for numerous sample types including plants[174,175], and organ and whole-body sections of mammals,[176] reptiles,[177] fish,[178,179] insects[180,181] and parasites.[182,183] By development of specialized workflows with matrix-precoated sample holders it is possible to use MALDI-MSI in a timeframe of surgical pathology.[184] In a recent publication, the lipid signatures of atherosclerotic plaque features have been studied in 106 plaque sections of human carotid artery parts that were surgically removed from 12 patients.[185] By statistical data analysis, the large MSI dataset was compressed in six components (clusters) with distinct spatial distributions. Each component possessed a spectral profile of lipid signals with a correlating spatial distribution. Comparing the derived MS image features with histologically identified plaque regions revealed a colocalization of SMs and oxidized CEs in necrotic core regions, as well as of DGs and TGs in fibrin-rich regions. Fibrin is a thrombosis-associated protein, indicating intraplaque bleeding which can be a precursor of plaque rupture and an impending heart attack. Specific lipids can be derived as potential markers for high-risk atherosclerotic plaques by decompressing the clustered data.[185] Instead

of exclusively looking at symptomatic (severe) plaques, Greco et al. compared lipid profiles of symptomatic and asymptomatic ones. They presented a whole workflow including the histology-/immunofluorescence-supported *in-silico* annotation of tissue regions and the subsequent data processing by multivariate data analysis. Applying this workflow, the authors were able to clearly discern between symptomatic and asymptomatic plaques by uncovering regiospecific lipidomic differences.[186]

Despite the great progress in MALDI-MSI instrumentation and data analysis, many substances of interest are inaccessible or not distinguishable for MS with common MALDI sample preparation. Sample washing [142], the application of internal standards[150] and on-tissue enzymatic digestion[187,188] are methodologies for a more sensitive and specific MALDI-MS analysis. These are complemented by on-tissue chemical derivatization (OTCD) strategies.

1.7. On-tissue derivatization and isomer-resolving MSI

OTCD methods can facilitate the detection of species that are hard to ionize, prone to suppression or matrix-background interferences and the differentiation of isomeric species that cannot be resolved by MS without chemical modifications.[189,190] Whereas chemical derivatization is well-established as in-solution reactions for other disciplines like electrophoresis, GC, and LC, the on-tissue version for MSI experiments is still challenging. Issues are associated with (1) analyte delocalization because excessive sample wetting by reagent solutions can occur, (2) undesired reactions or interferences with the reagent can complicate resulting mass spectra, and (3) low OTCD efficiencies due to insufficient solvation of the analytes or too short reaction time frames can counteract the intended benefits. Ideally, an OTCD reagent needs to react with the target analytes very efficiently and selectively while not affecting their lateral distribution. Spraying is the most common method to apply the derivatization reagent without wash-out effects but also vapor deposition and precoating of the MALDI targets are strategies to avoid derivatization-caused analyte delocalization.[189,190]

In the following, some sensitivity-enhancing methodologies are summarized. With reagent-precoated MALDI targets, Manier et al. enhanced the MALDI-MSI of neurotransmitters in pig adrenal glands and rat brain using an aldehyde reagent that forms Schiff´s bases (hydrazones) with primary amines under mild conditions (Scheme 3A).[191] Amines are popular derivatization targets because they are reactive and present in most metabolites, amino acids and neurotransmitters that can be veiled in the crowd of matrix-derived ions in the low *m*/*z* range. Attaching a derivatization reagent to an analyte shifts its mass into higher *m*/*z* regimes and can also enhance ionization efficiencies by introducing a charge (Scheme 3B).[192] Girard´s T reagent (GirT), for example, contains a charged ammonium group and its hydrazine moiety forms stable hydrazones with carbonyls (Scheme 3C). This compound has been used

to study the distributions of steroids that are hard to detect with MALDI-MS. Employing GirT-derivatization (GirT-precoated sample holders), Cobice et al. analyzed the steroid turnover to monitor the performance of the inhibitor for an dementia-associated enzyme.[193] Another group sprayed GirT onto samples to discriminate and image steroid isomers in human adrenal gland tissue surgically dissected from kidney cancer patients. They found elevated concentrations of aldosterone in aldosterone-producing cell clusters where cortisone and cortisol exhibited lower concentrations.[194] Precharged reagents can also serve for charge switching of negatively charged analytes like free fatty acids. Sun et al. recently presented a precharged amine reagent that, after spray deposition, reacts with carboxyl-containing compounds to form amides that are positively charged (Scheme 3D). Using their derivatization workflow, they imaged free fatty acids, citric acid cycle metabolites and PCs parallelly in the positive-ion mode.[195] Another charge switching OTCD reagent has recently been published that improves the MALDI-MSI of minor-abundant phospholipids in murine brain tissue by tagging phosphate monoesters with a zinc complex. Derivatized sphingosinemonophosphates, ceramidephosphates, PAs and LPAs could readily be imaged in the positive-ion mode whereas the imaging as negative ions of the underivatized species failed.[196]

Considering that OTCD reagents and matrices are often applied the same way (spraying, vapor deposition, sublimation), it is obvious that a combination, i.e., matrices that react with analyte molecules, are not necessarily a drawback like in the detrimental example of DAN that demethylates PCs.[148] Reactive matrices can effectively reduce the sample preparation and the risk of wash-out effects. Andren and coworkers took advantage of pyridinium salts[197] as reactive matrices that convert primary amines to charged pyridinium cations (Scheme 3E). With the use of such a pyridinium matrix, the group investigated the neurotransmitter metabolism in mice after knock-out of the Parkinson´s

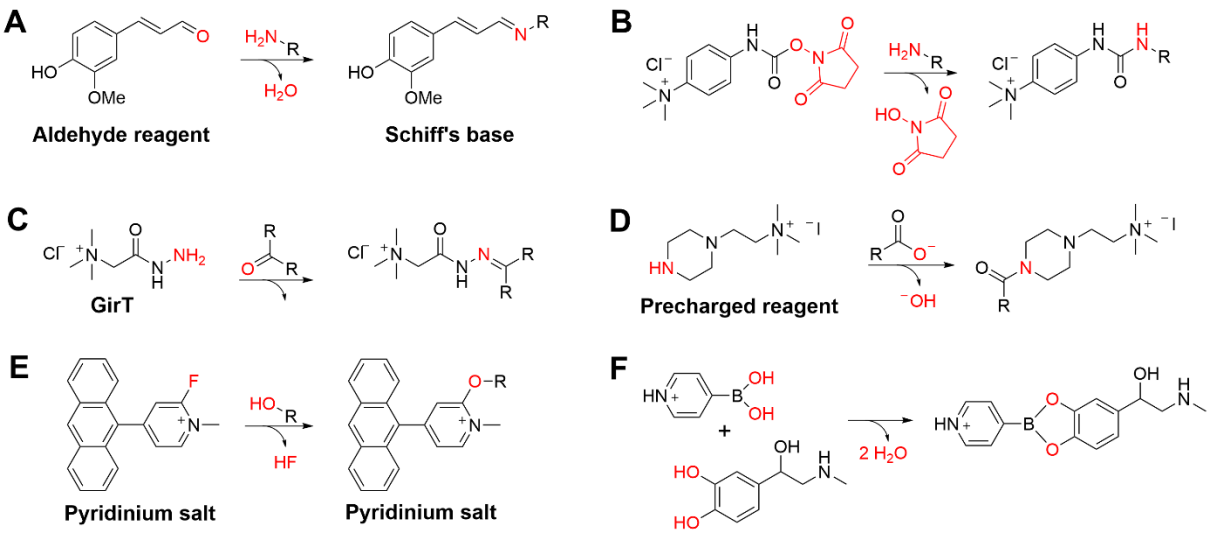

Scheme 3: Reaction schemes of the on-tissue chemical derivatization approaches discussed in this section.

disease-associated receptor GPR37. Lesions with the parkinsonism-inducing neurotoxin 6-hydroxydopamine were found to affect GPR37-knock-out mice stronger than wildtype controls. This has been interpreted as evidence that the presence of active GPR37 impedes the development of Parkinson´s disease.[198] In order to assist neurotransmitter imaging with a reactive matrix, not only the amine group can be derivatized but also the cis-diol function at the catechol backbone (Scheme 3F). By bounding the precharged reactive matrix 4-N-methylpyridinium boronic acid, the catecholamine detection is simplified because of higher ion yields, a higher mass beyond the crowded low *m*/*z* range and the characteristic isotope pattern for boron-containing species.[199]

Besides the presented sensitivity-enhancing OTCD techniques, various functionalization and fragmentation strategies have been developed to enhance specificity of on-tissue analysis, i.e., resolving lipid isomers in MSI experiments. The use of ozone for DBPI and *sn*-isomer identification has been demonstrated above. This has been exploited for DBPI-resolving MSI by employing on-tissue ozonization. It is carried out in an ozone-flushed reaction chamber, wherein the tissue lipids are converted to the Criegee ozonide which is subsequently analyzed by CID-MS^2 to laterally localize DBPIs in human colon sections with a lateral resolution down to 15 µm.[200]

Reactive oxygen species were also used for functionalization in an application by the Laskin group. Herein, singlet oxygen was photochemically generated in situ by UV laser irradiation of nano(D)ESI capillaries, forming hydroperoxides with lipid's DBs that can readily be cleaved by CID, enabling DBPI-resolved imaging with 30 µm pixel size.[201] Epoxidation has also been done on tissue as it was presented by Kuo et al., but the epoxidation with mCPBA was laborious (60 minutes incubation) and the lateral resolution was low (200 µm pixel size).[89]

Bednařík et al. adapted the PB methodology for OTCD and DBPI elucidation of PCs, PSs and glycosylceramides in mouse brain sections.[202] The PB reagent, benzaldehyde, was vaporized and introduced into a reaction chamber where it condensed onto the cooled tissue sample that was simultaneously irradiated by 254 nm UV light. Resulting PB products were ionized with a MALDI-2 source and subsequent CID allowed to map DBPIs of PC 36:1 and PS 36:2 (25 µm pixel size) in one MS^2I run. This was done because these are isobars (sharing the same nominal mass) that were co-isolated but could be distinguished by high-resolution MS. Post-ionization by the second laser of the MALDI-2 source ensured the efficient ionization of the PS that was suppressed by the PC species in conventional MALDI.

2. Aim of this work

The identification of lipidomic variations caused by diseases can help to understand the underlying biochemical processes and changes. For example, varied DBPI compositions in diseased tissue compared to healthy samples can unveil changed activities of distinct enzymes responsible for structural changes of lipids. In order to discover lipid DBPIs and their lateral distribution in tissue samples, this work had the intention to develop a direct on-tissue PB functionalization approach for DBPI-resolved MALDI-MS^2I analysis.

Based on earlier research with the in-solution PB reactions of acetophenone (AcPh) with unsaturated lipids,[108] the initial target was to use the known reagent directly on-tissue. Pure AcPh or AcPh:solvent mixtures were applied on tissue slides as thin films while the sample was irradiated with 254 nm UV light. In order to achieve the film, two approaches were tested: (1) Pneumatic spraying of the reagent and (2) dropping the reagent onto the tissue and covering it with an UV-permeable quartz cover slip. Because of low functionalization yields and the time-consuming sample treatment, another approach was considered. The new aim was to combine PB reagent and MALDI matrix and establish the concept of PB-reactive MALDI matrices. BPh was tested as reactive matrix because of three reasons: (1) The PB reactivity was shown in solution,[203] (2) BPh allows highly efficient ISC to the triplet state that is assumed to play a key role in the PB reaction[99,204] (3) the chromophores were expected to assist both the photochemical activation for the PB reaction and the absorption of the MALDI laser light. Since BPh performed as both MALDI matrix and PB reagent, the next goal was to develop and optimize an on-tissue sample preparation ensuring to homogenously cover the sample with small BPh-crystals without sample washout effects. The method of choice was pneumatic spraying, and the parameters to optimize were mainly the solvent composition and the sprayed volume of BPh solution. During spraying, the sample was UV-irradiated to excite the photochemical PB reaction. Data of later light-exclusion experiments suggested that the main part of the PB yield did not rely on UV-lamp irradiation but was caused by the UV-MALDI laser pulses. Finally, to establish BPh as a new matrix, the imaging results had to be compared to a common matrix, the scope of DBPI-analyzable lipid classes were elucidated, and the new DBPI-resolved imaging technique had to be tested. The MSI and DBPI-resolved MS^2I abilities were evaluated by using well-known mouse cerebellum tissue but also the lateral DBPI-distributions in *Schistosoma mansoni* were investigated.

After the proof-of-principle with BPh, the aim was to improve the PB-reactive matrix approach in terms of ion and PB yields as well as the scope of lipids that can be analyzed. Hence, BPh derivatives were screened and conclusions were drawn about PB-reactivity trends of tested compounds, inter alia, that pyridine-based matrices especially BzPy provide good PB yields and boost ionization because of the

basic nitrogen. The screening experiments raised the question if a systematic study of different reactive matrices and lipid substrates can provide reactivity trends to improve the MALDI-laser-initiated PB functionalization. Reactivity trends were thus evaluated for halogen-substituted BPh-derivatives, as well as for lipids possessing various head groups and various degrees of unsaturation. Furthermore, DBPI analysis was performed for lipid standards of 13 lipid classes in both polarities. The long-term goal of DBPI-resolving MS^2I is the application to biological and medical problems. BzPy was therefore employed for MALDI-MSI and -MS^2I studies of various healthy and diseased organ tissue types including, e.g., brain, kidney and pancreas of wildtype (wt), diabetic and cardiovascularly diseased mice.

3. Results

The goal of this work was to bring lipidomic MALDI-MS imaging on the DBPI level, i.e., to reach the mass spectrometric differentiation of DBPIs in MALDI-MS^{2}I experiments. To achieve this target, the PB methodology developed for shotgun MS during my master thesis was adapted for on-tissue functionalization. For this purpose, the following needed to be considered: An efficient derivatization requires the analyte extraction from tissues. In contrast to the reaction of whole-tissue extracts, on-tissue methods for MSI must retain the endogenous location of analytes. An optimized workflow balances analyte extraction and diffusion for sufficient solvation without the risk of wash-out effects. This means to carefully adjust PB-reagent/solvent mixture composition, overall applied volume and application speed.

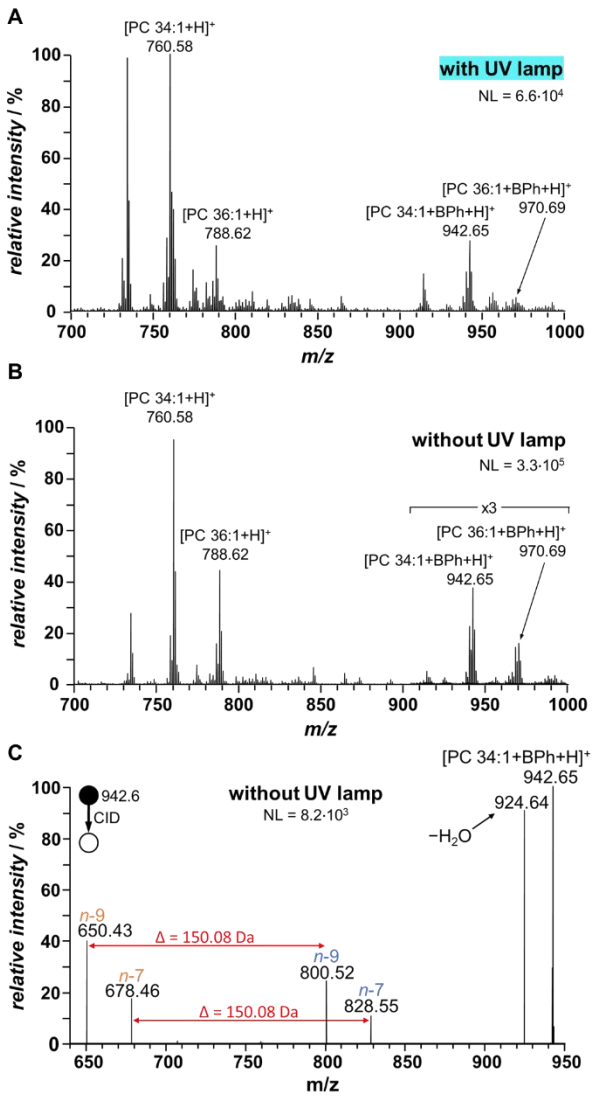

Figure 5: MALDI mass spectra recorded from BPh-covered mouse brain sections (A) with (B) without UV lamp irradiation. (C) MALDI-MS^2 spectrum of [PC 34:1+BPh+H]$^+$. NL = normalized level. Reprinted with permission from reference 206 © 2019 American Chemical Society.

AcPh performed well as PB reagent in nanoESI experiments.[108] To transfer this performance to an on-tissue method, pure AcPh or AcPh/methanol (MeOH) mixtures were applied to tissue sections while the sample was irradiated by a mercury-vapor UV pencil lamp. Despite using various application techniques (droplet-application and pneumatic spraying) and optimizing their parameters, AcPh did not yield sufficient PB functionalization. Benzaldehyde was anticipated to be more reactive than AcPh but also failed as PB reagent for our DBPI-resolving MS^{2}I approach. 2,5-Dihydroxyacetophenone (DHAP) is known to perform as MALDI matrix[205] and motivated by the fact that AcPh in principle enables DBPI analysis, the dihydroxy-derivative was tested as PB-reactive matrix. To promote the photoreaction, the sample was UV-irradiated during the pneumatic spraying procedure of DHAP. Excellent ion intensities were observed, better than with the previously used matrix DHB, but no PB product. In contrast, BPh was shown to be PB-reactive and to be effective as MALDI matrix.

In the first publication of the project[206] the results of implementing BPh as new PB-reactive MALDI matrix for high-resolution MALDI-MSI and DBPI-resolved MALDI-MS^2I are presented. Before using BPh as MALDI matrix, it was tested as on-tissue PB reagent in combination with DHB as MALDI matrix that was applied after PB-functionalization. BPh outperformed the low yields of AcPh and benzaldehyde. In contrast to the droplet-application, BPh-spraying provided homogenous reagent deposition by exploiting the advantage of small solvent volumes (spray droplets), ensuring the analyte extraction for efficient derivatization while preventing lateral analyte delocalization. Optimization of the BPh concentration and the solvent mix composition enabled to acquire the first DBPI-resolved MALDI-MS^2 images that display histological tissue structures in mouse cerebellum.

After BPh was observed to be a good on-tissue PB reagent for DBPI resolution in MS^2I, it was tested as reactive matrix by omitting DHB as additional matrix. The resulting MALDI-MS and -MS^2 spectra are shown in Figure 5. Comparing the signal intensities in spectra of tissue with and without additional DHB showed only one order of magnitude lower signal with BPh as exclusive matrix. It is worth noting that much cleaner spectra, i.e., fewer noise peaks were obtained with only BPh. Most likely this is because the mutual ionization of DHB and BPh yielding matrix cluster ions is prevented. With the objective to introduce BPh as PB-reactive matrix allowing high lateral resolution DBPI-specific MALDI-MS^2I, homogenous BPh-coverage of tissues with matrix crystals possessing sizes below 15 µm was required. Parameters of the matrix spraying setup and protocol that had to be optimized were the concentration of BPh and the ionization-assisting trifluoracetic acid (TFA), the solvent composition, the UV irradiation time, the overall sprayed volume, the spraying flowrate, the sample-to-spraying-needle distance, the sample-to-UV lamp distance, the strength of the nebulizing-gas flow (N_2) and the rotational speed of the sample holder. As their influence on the PB yield, the BPh crystal size and crystal homogeneity was negligible, the sample's rotation velocity (5 rotations per second), the UV lamp distance (3 mm) and irradiation time (3 minutes) were set after short optimization and held constant. The sample-to-spraying-needle distance is defined by the size of the spraying chamber. To avoid the laborious construction of several spray chambers, this parameter was set (66 mm) and held constant while adapting the other parameters. The spraying flowrate was optimized for minimal sample preparation time while not causing sample wash-out. Low flowrates (<10 µL/min) were considered to maximize the PB yield by providing a thinner solvent film that allows more photons to reach the BPh molecules in close vicinity to the analytes. This effect was not confirmed. As higher flowrates caused wash-out effects, 10 µL/min was determined as the optimum. The N_2-flow must be strong enough to nebulize the matrix-solution to a fine spray. At the same time a too strong gas stream leads to wash-out caused by too fast impacting solution droplets. Optimal conditions were found with a fully opened valve and a pressure regulator setting of 0.5 bar. Besides improving the ion yield, the addition of TFA to the spraying solutions turned out to affect the BPh matrix layer quality as well. After using 0.2% TFA

in the optimization experiments, higher concentrations were tested for better ionization and 0.5% was selected as a maximum of ionization-assistance without impacting the quality of the matrix layer.

Fast BPh crystallization is beneficial for matrix quality because it prevents sample wetting and it favors small crystallites over bigger crystals due to kinetic trapping of small crystals. However, it was hypothesized that too fast crystallization does not allow BPh to react with the analytes in the solution phase. In the best case, the tissue is covered by small, isolated solution droplets in that lipids are extracted and PB-derivatized to subsequently co-crystallize with BPh. In order to support fast crystallization, solutions with high BPh concentrations (near saturation) have been prepared in volatile solvent mixtures. Because it is difficult to predict the effects of variations of the BPh concentration and the solvent composition, numerous combinations were empirically tested in order to find the optimized spraying workflow described above. The BPh concentration was first varied between 5 and 90 mg/mL. After these initial experiments, a smaller concentration range between 5 and 30 mg/mL was set for the screening with numerous solvent mixtures. Concentrations exceeding 30 mg/mL were too often prone to clogging the sprayer. The tested solvents fulfilled different roles as explained hereafter: Acetonitrile (AcN) and MeOH were selected because they readily dissolve BPh and lipids. 2-Propanol (6.00 kPa)[207] and water (3.07 kPa)[208] exhibit lower vapor-pressures (values in brackets) than AcN (11.8 kPa)[209] and MeOH (16.9 kPa)[209] and were employed to achieve mixtures with moderate volatility. Ethanol (7.87 kPa)[207] was tested in some mixtures as it is of intermediate solvation performance and volatility like 2-propanol, but the latter was superior in this discipline. MeOH easily solved lipids and BPh but was replaced by AcN because of the lower vapor-pressure at similar solvation ability. The optimized spraying solution was 20 mg/mL BPh in 6:3:1 AcN/2-propanol/water with additional 0.5% TFA. To protect analytes from direct laser impacts and consequent fragmentation, a MALDI matrix excess is necessary. Although, a too high matrix excess prevents matrix suppression and leads to intense matrix ion background in MS spectra. The matrix layer thickness is determined by the overall sprayed matrix solution volume and its concentration. Varying the volume between 100 and 400 µL revealed 230 µL to be the optimum for high PB yields and lipid ion intensity with the above-described spraying solution.

Due to the detection of PB products after BPh coating without UV irradiation (Figure 5), light exclusion experiments were undertaken to eliminate the PB activation by ambient UV light. Still, PB products were detected by MALDI-MS suggesting that the reaction is activated by the UV laser of the MALDI source. To examine this hypothesis, multiple mouse cerebellum tissue sections were BPh-coated under light exclusion, the samples were scratched from the sample holder, lipids were extracted with a methyl-*tert*-butylether extraction protocol[210] and the extract was analyzed by HPLC-ESI-MS. This experiment still identified lipid PB derivatives but in much lower yields (0.03% versus 12%). On the one

hand this shows how highly reactive BPh is and on the other hand supports the assumption that the UV laser initiates the PB functionalization. Further support for the latter was found in measurements of the PB yield as a function of energy per MALDI laser pulse that ascertained a direct correlation (Figure 6). Without UV irradiation during the matrix spraying, higher normalized levels were observed (Figure 5). Although the PB yield (12% vs. 21%) was lower than with UV irradiation, the absolute ion count of PB products was higher. Consequently, no more UV-irradiation via Hg-lamp was required during the sample preparation workflow.

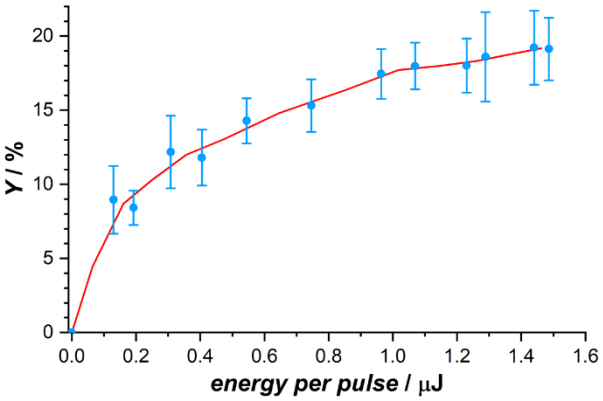

Figure 6: PB reaction yield (*Y*) of $[PC\ 34:1+BPh+H]^+$ from a BPh-covered mouse brain tissue section as a function of the energy per MALDI laser pulse. Blue dots represent the mean *Y* value from 100 individual measurements. The error bars are the corresponding standard deviation and the two-point floating average of *Y* (red line) is depicted as a guide to the eye. Reprinted with permission from reference 206 © 2019 American Chemical Society.

After workflow optimization, the analytical scope of the new matrix was evaluated by DB position analysis of various lipid standards and of endogenous lipids from mouse cerebellum tissue. Indeed, DB positions of PC, PE, PI, PA, PG, and SM standards and ten PCs directly from tissue were inferred. In order to assess the matrix performance aside its functionalization ability, the imaging results were compared to those with a DHB-coated sample. BPh allows MSI with a good lateral resolution of 15 µm pixel size and the lipid coverage as well as the lipid distributions were similar using BPh and DHB as matrix (Figure 7). Comparing the lists of annotated lipid signals (92 with DHB and 74 with BPh as matrix), BPh appeared to promote protonated species while alkali metal adducts were less intense or absent for some species that were better detected by DHB. In turn, some protonated species were exclusively detected using BPh.

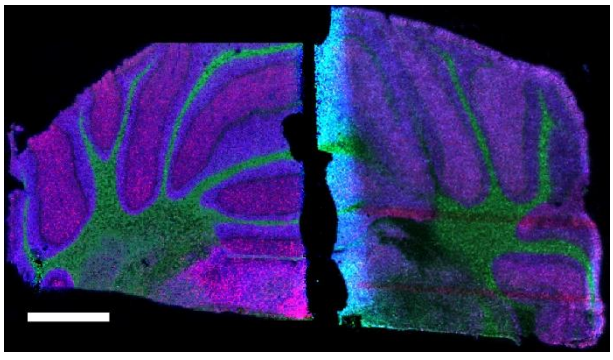

Figure 7: RGB MALDI-MS images of mouse cerebellum acquired with 15 µm pixel size in the full pixel mode using (left) BPh and (right) DHB as matrix. The laterally resolved signal intensities of three selected lipids are superimposed: $[PE\ 36:0+H]^+$ (red, *m/z* 748.585), $[PC\ 36:1+H]^+$ (green, *m/z* 788.617), and $[PC\ 32:0+H]^+$ (blue, *m/z* 734.570). The scale bar reflects 1 mm. Reprinted with permission from reference 206 © 2019 American Chemical Society.

Following the matrix evaluation in DBPI analysis and as a MALDI-MSI matrix, the capabilities for DBPI-resolved MALDI-MS^2I were examined. Mouse cerebellum MALDI-MS^2 images were acquired for PCs with lateral resolutions down to 15 µm pixel size which enable the resolution of

small histological tissue regions (Figure 8) in the range of murine neuronal cell size.[211,212] In accordance with previous reports, the abundances of the *n*-9 DBPIs of PC 34:1 and PC 36:1 were elevated in the white matter whereas the *n*-7 DBPIs showed a complementary elevation in the gray matter of the cerebellum.

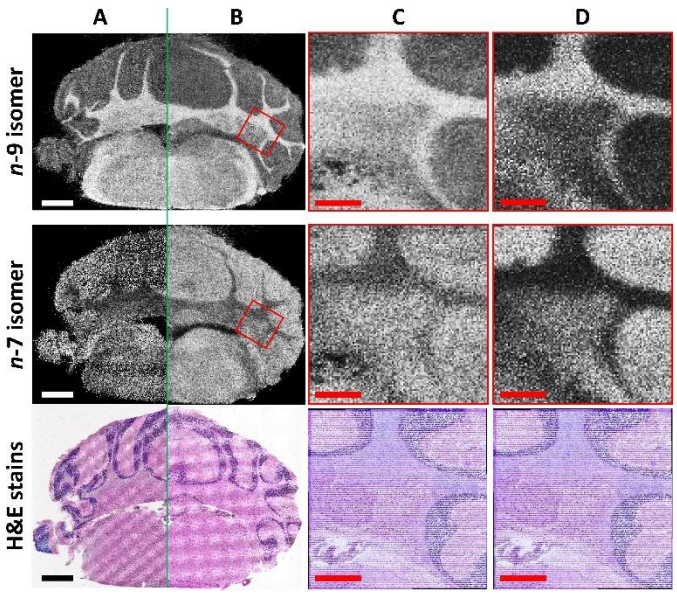

Figure 8: MALDI-MS² images of the DBPI-diagnostic fragment ions of (A) PC 36:1 and (B–D) PC 34:1 acquired from mouse cerebellum sections with (A,B) 25 µm and (C,D) 15 µm pixel size. Signal intensities were (A–C) TIC normalized or (D) relative intensities (*n*-9/*n*-7 and *n*-7/*n*-9) are used. The red square in B highlights the region measured in C and D. Lower row: Optical microscope images of post-MALDI-MS²I hematoxylin and eosin (H&E) stained tissue sections. Scale bars reflect (A,B) 1 mm and (C,D) 0.4 mm. Reprinted with permission from reference 206 © 2019 American Chemical Society.

In order to test the new PB-reactive matrix for its use in studying unknown samples, DBPI-distributions of PC 34:1 in a whole parasitic worm (*S. mansoni*) were imaged using the 3D-autofocusing mode of the AP-SMALDI[5] AF ion source (Figure 9). Fragment ions of DBs in three different positions were detected (*n*-9, *n*-7, *n*-13). Whereas homogenous distributions were found for the *n*-9 and *n*-7 isomers, the data revealed an elevation of the unusual *n*-13 DBPI in the head- and the tail-region of the parasite. Localization of the DBPI in these regions suggests a local function of it or that it is the product of a local metabolic process.

The described methodology was developed with an atmospheric pressure AP-SMALDI[5] AF source. To test the application to other ion source systems, BPh-covered mouse cerebellum tissue was analyzed employing an intermediate pressure MALDI-2 ion source[159,160] of the Dreisewerd group. Both the varied pressure domain and varied ionization technique did not inhibit the MALDI-laser-induced PB derivatization (Figure 10).

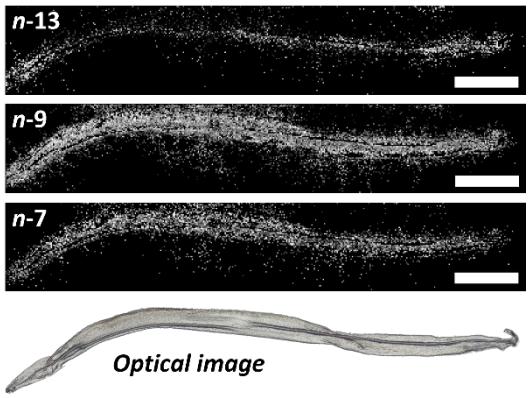

Figure 9: MALDI-MS² images of DBPI-diagnostic fragment ions of PC 34:1, acquired from a male *S. mansoni* worm with 20 µm pixel size. Signal intensities were TIC normalized. The lower row shows an optical microscopy image before the measurement. Scale bars reflect 1 mm. Reprinted with permission from reference 206 © 2019 American Chemical Society.

The second publication of the project[213] describes the results of the efforts to improve the PB-reactive MALDI matrix performance. A screening of twelve BPh-related compounds as PB-reactive matrices was performed to enhance the PB yield, the ionization efficiency, and the scope of analyzable lipid classes. For the screening, a PC 18:1 (*n*-9)/18:1 (*n*-9) standard

and one of the potential matrices were consecutively deposited onto teflon-coated microscope slides by dried-droplet deposition. The resulting samples were measured by MALDI-MS to evaluate ionization and matrix-attachment, followed by MALDI-MS^2 to confirm the attachments as PB products. In Figure 11 a bar diagram shows blue and red bars for the normalized level of the $[PC\ 18:1/18:1+H]^+$ (ion yield) and the matrix-attachment yield (*Y*), respectively. Amino- and hydroxy derivatives increased the PC ion signal by a factor of up to 27 compared to BPh but the attachment yields were low, and the fragmentation spectra of lipid-matrix adducts did not contain any DB-fragments. It was concluded that electron donating groups diminish the matrices' PB reactivity. Extension of the aromatic system has this negative effect as well. In contrast, pyridinyl derivatives of BPh were found to improve PB reactivity.

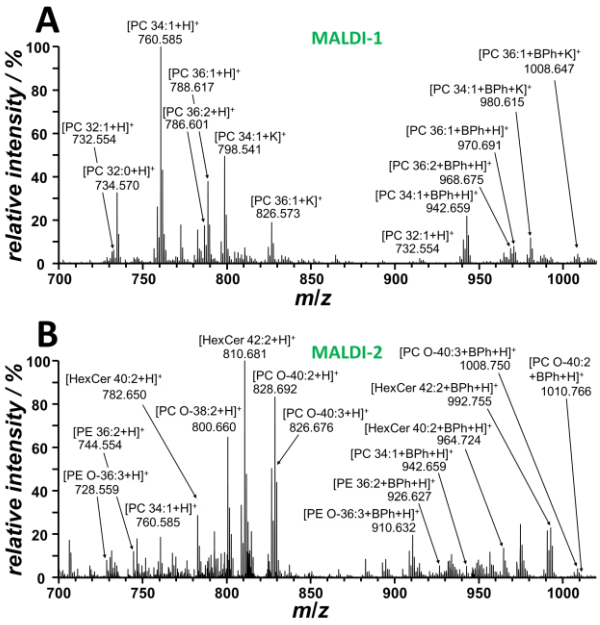

Figure 10: (A) MALDI-1-MS and (B) MALDI-2-MS spectrum of mouse cerebellum using an intermediate pressure MALDI-2 ion source and BPh as PB-reactive MALDI-matrix.

In order to further examine the effect of electron structure variations in the aromatic system, BPh and 4-halogenobenzophenone derivatives with fluorine, chlorine, bromine and iodine were used to systematically decrease the electron density of the reactive matrix. 4-Fluorobenzophenone slightly increased the PB yield compared to BPh but all other 4-halogenobenzophenone caused lower yields. Most likely, this is due to the electron donating mesomeric effect that negates the electron withdrawing inductive effect and consequently results in electron donation by Cl, Br, and I substitution.

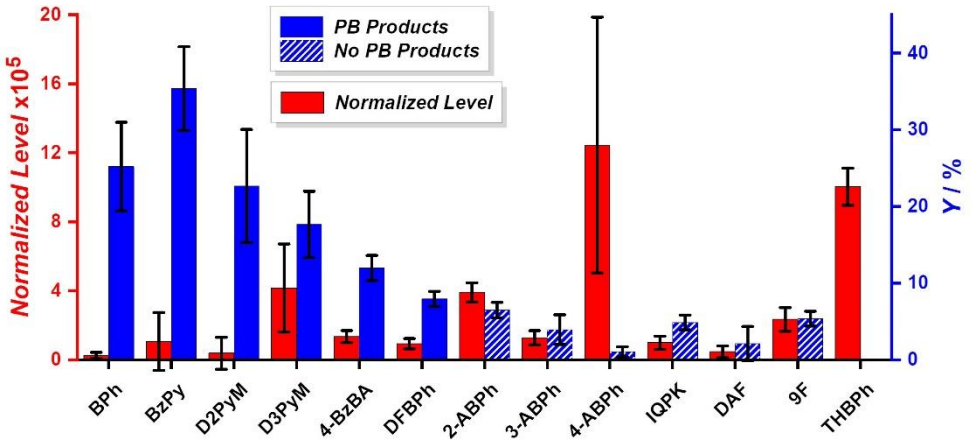

Figure 11: Normalized levels of the PC 18:1/18:1 standard (red bars) and the matrix-attachment yield, *Y*, (blue bars) for each matrix of the screening. MS^2-confirmed PB product formation and absent PB reactivity are indicated by full blue and hashed blue bars, respectively. Reprinted with permission from reference 213 © 2020 American Chemical Society.

To investigate the effect of varying the lipid's head group and unsaturation, PB functionalization with BPh was tested for PC, PA, PG, PE, PI, PS (each with the FA-combination 16:0/18:1) and PC 16:0/18:1, PC 18:1/18:1, PC 18:2/18:2, PC 16:0/20:4, respectively. The PB yield showed to be very similar for the different head groups and to be higher for more unsaturated FAs. At the same time, the yield did not change by adding a DB while the number of DBs per FA was maintained, i.e., same yields were recorded for PC 16:0/18:1 and PC 18:1/18:1.

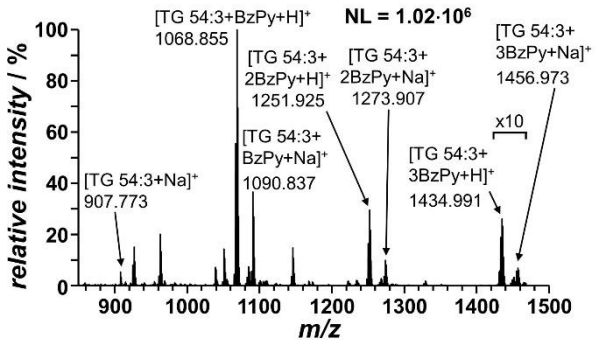

Figure 12: MALDI mass spectrum of a TG 54:3 standard using BzPy as PB-reactive MALDI matrix. Reprinted with permission from reference 213 © 2020 American Chemical Society.

Among the screened matrices, the highest PB reactivity was found for BzPy that outperforms BPh by roughly 10% higher PB yields. Pyridine moieties have the additional advantage of a basic nitrogen that can boost the ion intensity of protonated BzPy-adducted lipids in the positive-ion mode. In experiments that were done to test the lipidomic scope of the new matrix compound, protonated species of PG, cardiolipin (CL), and TG standards were exclusively detected after BzPy-attachment (Figure 12). These experiments furthermore showed the extended field of lipid classes that can be analyzed on the DBPI level. Whereas DB positions were pinpointed in PC, PE, PI, PA, PG, and SM standards with BPh, BzPy adds FAs, SHexCers, PSs, HexCers, CLs, TGs, and plasmalogen PCs to this list. Especially the entries of FAs and SHexCers are noteworthy because these represent the first examples of unveiling DB positions by MALDI-MS^2 in the negative-ion mode.

BzPy is a dual-polarity matrix and can therefore cover many compounds of various lipid classes which has been demonstrated by the annotation of 133/58 lipids in positive/negative-ion mode MSI of mouse cerebellum. The 37/11 lipids that were exclusively detected as BzPy adducts highlight the additional benefit of the pyridine-based reactive matrix. BzPy makes possible a more than doubled lateral resolution (7 µm) compared to BPh (15 µm) which was used to

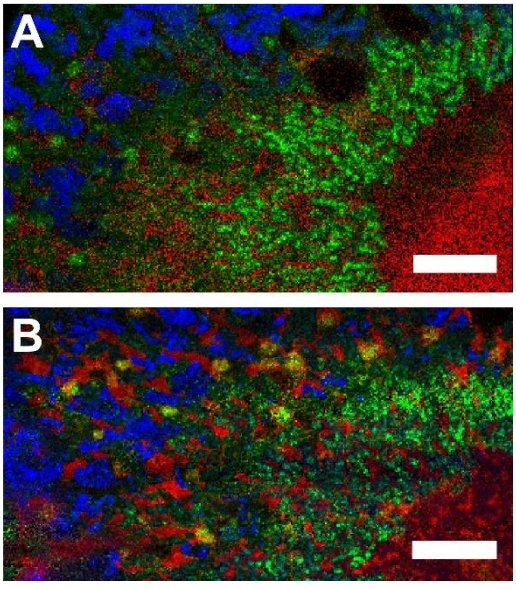

Figure 13: RGB MALDI-MS images of the mouse kidney acquired in (A) the positive- and (B) negative-ion mode with 7 µm step size. The TIC-normalized laterally resolved signal intensities of $[PS\ O\text{-}36{:}1+H]^+$ (red, *m/z* 776.581), $[SM\ 34{:}1+H]^+$ (green, *m/z* 703.575), and $[PE\ 38{:}0+K]^+$ (blue, *m/z* 814.573) in the positive-ion mode and $[PA\ 36{:}1-H]^-$ (red, *m/z* 701.513), $[PE\text{-}Cer\ 36{:}1-H]^-$ (green, *m/z* 687.544), and $[SHexCer\ 42{:}2-H]^-$ (blue, *m/z* 888.623) in the negative-ion mode were superimposed. The scale bars reflect 0.4 mm. Reprinted with permission from reference 213 © 2020 American Chemical Society.

image fine structures in mouse kidney sections in both MS ion modes (Figure 13). Comparing the acquired MS images with post-MSI microscopy images shows that histological structures are well reflected by BzPy-based MALDI-MSI and that the sample preparation does not cause sample wash-out.

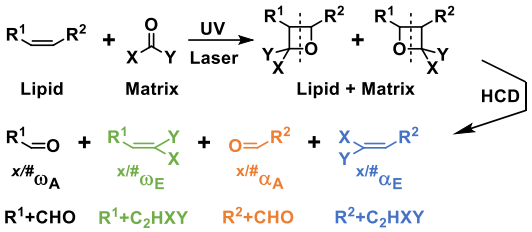

Scheme 4: PB functionalization and HCD of functionalized lipids. R^1 and R^2 are the residues containing the FA carbon chain and the lipid head group, respectively.

BzPy was also applied in DBPI-analysis directly from mouse pancreas tissue and in contrast to BPh, BzPy facilitates DBPI-resolution of a SHexCer from tissue in the negative-ion mode. As shown in Scheme 4, the DB fragment ions are labeled as α or ω ions depending on whether they contain the head group or the remaining FA residue. "A" and "E" in the subscript indicate if the fragment contains an **a**ldehyde or an alk**e**ne moiety, respectively. The superscript *x* reflects the DB position in the FA and # the overall number of DBs in the FA. Figure 14A and B show MS^2 spectra of $[PC\ 34:1+BzPy+H]^+$ and $[PC\ 36:2+BzPy+H]^+$ from mouse pancreas which reveal DB position isomerism for both lipids. Fragmentation of $[PC\ 34:1+BzPy+H]^+$ yielded DBPI-diagnostic fragment ions for PC 34:1 (*n*-9) and PC 34:1 (*n*-7). PC 36:2 was identified as containing either one di-unsaturated FA (with *n*-6 and *n*-9 DBs) and one saturated FA or two mono-unsaturated FAs (with a *n*-9 or a *n*-7 DB). Compared to BPh (15 µm), the lateral resolution of MS^2I experiments has been improved to 10 µm pixel size (Figure 14C and D). After the MALDI-MS^2I measurements, immunofluorescence staining was successfully performed as indicated by the fluorescence microscopy image in Figure 14E. The islets of Langerhans, which mainly consist of β-cells in mouse pancreas, were stained in red. In sum, the α fragment ions of four selected PC *m/z* values were imaged in pancreas tissue sections. No isomeric α ions were detected for PC 36:4 and PC 34:2 but distinct lateral distributions were found for the above-mentioned isomers of PC 34:1 and PC 36:2 (Figure 14C, D and 14F–I). PC 34:1 (*n*-9) and PC 34:1 (*n*-7) have a converse distribution in the pancreatic islets where they possessed elevation and depletion, respectively (Figure 14C and D). A homogenous distribution was found for the diagnostic fragment ions of the di-unsaturated DBPI of PC 36:2 (Figure 14F and G) whereas its mono-unsaturated DBPIs were both enriched in the tissue regions that were characterized as islets of Langerhans (Figure 14H and I).

In addition to the already published results, some measurements were done for the long-term goal of applying DBPI-resolving MS^2I to biological and medical issues as well as in routine analytical workflows. To test the developed methodology in medical research, it has been employed for investigations in organ tissue sections of disease-model mice. As a follow-up study of the results in pancreas described above, pancreas tissue sections of diabetic (db/db) and wt mice were studied and the DBPI ratios of PC 34:1 in the islets of Langerhans were compared. Diabetic mouse pancreatic islets exhibited a

significant decrease of the *n*-9/*n*-7 ratio indicating a diminished importance of the *n*-9 isomer or a more relevant role of the *n*-7 isomer.

Also, the cardiovascular disease mouse model (B6.129P2-Apoe^{tm1Unc}/J) has been studied to decipher characteristic lipidomic changes in pro-atherosclerotic mice. High-resolution (15 µm pixel size) MS- and MS^2-images were acquired for apolipoprotein-E KO (apoE$^{-/-}$) and wt mouse lung tissue (Figure 15) and lipid annotations as well as lipid distributions were compared. The annotations include underivatized lipids and BzPy-adducted ones. BzPy-adducts dominate the positive-ion mode annotations which again highlights the advantage of BzPy's basicity exerting a protonation boost after PB or non-covalent attachment compared to endogenous lipids. Altogether, in the positive/negative-ion mode 243/186 and 192/214 lipids were assigned in wt and apoE$^{-/-}$ mouse lung tissue, respectively. Comparing the apoE$^{-/-}$ to the wt annotations, an elevation of GP signals and a depletion of sphingolipid and GL signals in apoE$^{-/-}$ tissue were observed. The lateral distributions of lipids that were found in mutant and wt were scanned for local variations. After assignment of the latter to histological features in microscopy

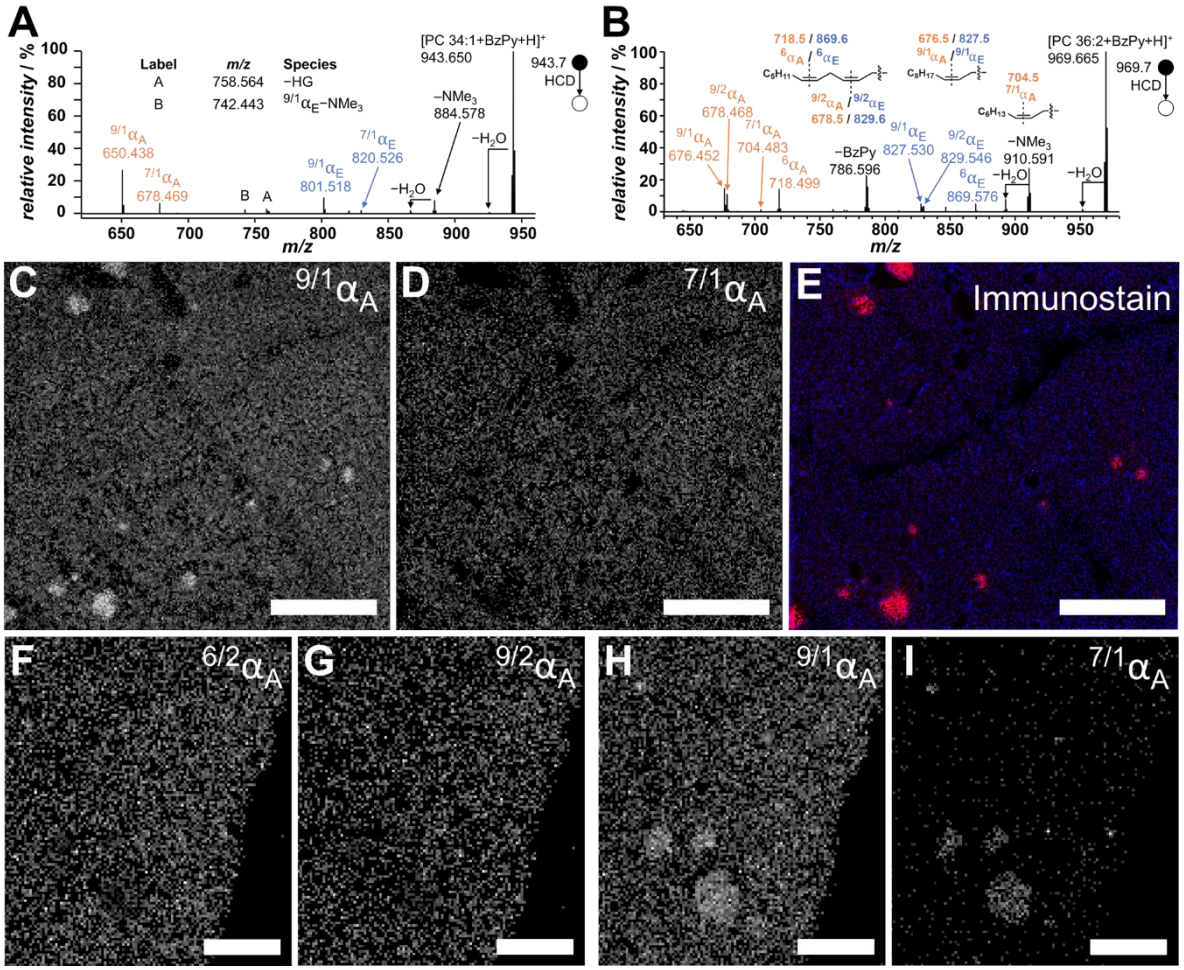

Figure 14: MALDI-MS^2 and -MS^{2}I from mouse pancreas tissue sections: HCD-MALDI-MS^2 spectra of (A) [PC 34:1+BzPy+H]$^+$ and (B) [PC 36:2+BzPy+H]$^+$. MALDI-MS^2 images are shown for the DBPI-diagnostic fragment ions of (C, D) PC 34:1 and (F–I) PC 36:2, acquired with 10 and 20 µm pixel size, respectively. Signal intensities were TIC normalized. E shows a fluorescence microscopy image of the post-MALDI-MS^{2}I-immunofluorescence-stained pancreas tissue section of C and D. Scale bars reflect 0.6 mm. Reprinted with permission from reference 213 © 2020 American Chemical Society.

images, the distributions in apoE$^{-/-}$ and wt tissue were compared. In both cases, elevation and depletion were foremost identified in tissue regions of bronchi and blood vessels. In detail, the sites of higher intensity were sorted in five categories, (1) surrounding bronchi and blood vessels, (2) surrounding bronchi, (3) in bronchi and blood vessels, (4) in bronchi, and (5) in blood vessels, like exemplified for wt tissue in Figure 16A, B, C, D, and E, respectively. Table 1 summarizes the lipids assigned to the five categories.

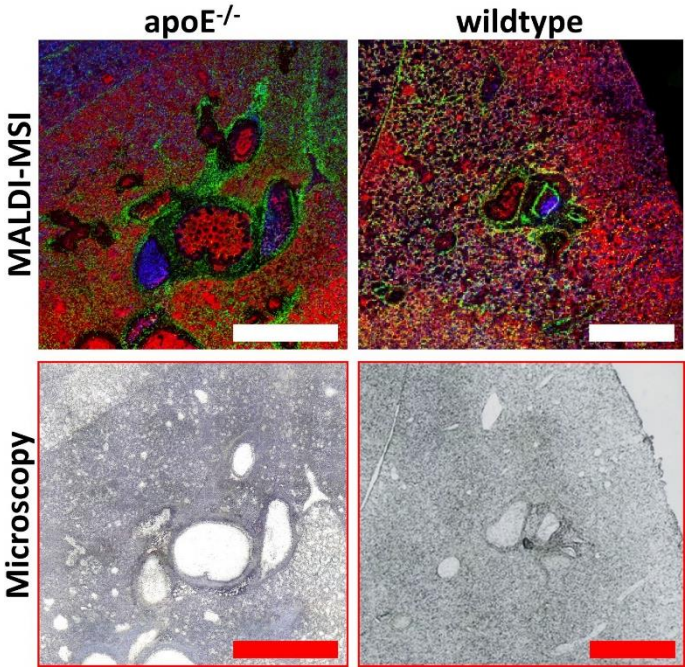

Figure 15: Upper row: RGB MALDI-MS images of the apoE$^{-/-}$ and wt mouse lung acquired with 10 and 15 µm pixel size, respectively. The TIC normalized laterally resolved signal intensities of $[PC\ 34:3+H]^+$ (red, *m/z* 756.551), $[SM\ 34:1+K]^+$ (green, *m/z* 741.529), and $[PC\ 34:0+H]^+$ (blue, *m/z* 762.583) were superimposed. Lower row: Optical microscope images of post-MALDI-MSI tissue sections. The scale bars reflect 1 mm.

Category (1) comprises various SMs that are absent in the other categories except one example in (5). Ether-PSs that were assigned to (1) bear rather long-chain FAs (∑C-atoms ≥ 36) compared to category (4)-assigned ether-PSs (∑C-atoms ≤ 34). Furthermore, only unsaturated lipids were assigned to category (1). As it was observed in an earlier work,[213] PC 34:0 was found enriched in blood vessels and consequently listed in (5). Whereas the annotations in the categories (1) and (5) are similar for apoE$^{-/-}$ and wt tissue, annotations differ greatly in the categories (2), (3) and (4). PAs, for example, were only present in bronchi of apoE$^{-/-}$ lung and acyl-PSs were only found in wt lung. The tendency of longer FA chains in category (1) compared to category (4) is again observed for acyl-PSs with ≥ 36 C-atoms versus 34 C-atoms, respectively. Annotations in category (3) differ the most between apoE$^{-/-}$ and wt lung having only PC 32:0 in common. Category (3) of apoE$^{-/-}$ tissue additionally comprises PS O-34:0 and PS O-36:3, whereas wt annotations are more diverse with HexCer 36:1, PE O-34:0 and the additional PC 32:1. Exclusive enrichment around the bronchi (category

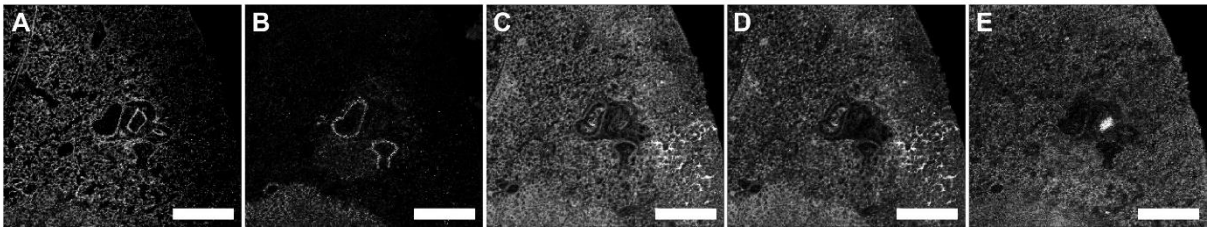

Figure 16: TIC-normalized MALDI-MS images of wt mouse lung acquired with 15 µm pixel size. (A) $[SM\ 34:1+K]^+$ (*m/z* 741.531), (B) $[PS\ 38:3+H]^+$ (*m/z* 814.558), (C) $[PC\ 32:0+Na]^+$ (*m/z* 756.552), (D) $[PC\ 30:0+Na]^+$ (*m/z* 728.521), and (E) $[PC\ 34:0+H]^+$ (*m/z* 762.600). The scale bars reflect 1 mm.

(2)) is only observed in wt lung tissue. In detail, category (2) is filled with PCs of various chain lengths (32 – 38 C-atoms), PE 36:1, PS O-36:1 and various long chain PSs (36 – 42 C-atoms).

Table 1: Lipids annotated in apoE$^{-/-}$ and wt mouse lung tissue and assigned to five categories of sites of higher concentrations: (1) surrounding bronchi and blood vessels, (2) surrounding bronchi, (3) in bronchi and blood vessels, (4) in bronchi, and (5) in blood vessels.

Annotated lipids		**Category**
apoE$^{-/-}$	**wt**	
	PC 34:1	(1)
	PS 36:2	(1)
PC 36:4		(1)
PS O-36:2	**PS O-36:2**	(1)
	PS O-36:3	(1)
	PS O-38:2	(1)
	PS O-38:3	(1)
	PS O-38:4	(1)
SM 34:1	**SM 34:1**	(1)
	SM 34:2	(1)
SM 36:1	**SM 36:1**	(1)
SM 40:1		(1)
	SM 42:1	(1)
	SM 42:2	(1)
	PC 32:0	(2)
	PC 32:1	(2)
	PC 34:2	(2)
	PC 34:3	(2)
	PC 36:1	(2)
	PC 38:5	(2)
	PE 36:1	(2)
	PS 36:0	(2)
	PS 36:1	(2)
	PS 36:2	(2)
	PS 38:3	(2)
	PS 42:4	(2)
	PS 42:5	(2)
	PS O-36:1	(2)

Annotated lipids		**Category**
apoE$^{-/-}$	**wt**	
	HexCer 36:1	(3)
PC 32:0	**PC 32:0**	(3)
	PC 32:1	(3)
	PE O-34:0	(3)
PS O-34:0		(3)
PS O-36:3		(3)
	DG 30:1	(4)
DG O-32:2		(4)
	HexCer 36:2	(4)
PA 32:1		(4)
PA 34:1		(4)
PA 34:2		(4)
PC 30:0	**PC 30:0**	(4)
PC 30:1	**PC 30:1**	(4)
PC 32:1		(4)
	PC 32:2	(4)
PC 36:5		(4)
PE 34:0		(4)
	PE O-32:0	(4)
	PS 34:1	(4)
	PS 34:2	(4)
PS O-32:1	**PS O-32:1**	(4)
PS O-34:1	**PS O-34:1**	(4)
PS O-34:2	**PS O-34:2**	(4)
	PS O-34:3	(4)
PC 34:0	**PC 34:0**	(5)
	PE 36:0	(5)
	SM 40:1	(5)

Besides endogenous lipids, PB functionalized lipids or non-covalent BzPy-adducts were imaged and the lateral distributions showed good agreement with those of underivatized counterparts. This indicates that the chosen sample preparation procedure prevents wash-out effects during reaction and that the PB products as well as the downstream DB-associated fragments reflect the endogenous lateral distributions.

DBPI-resolved MS^2 images of wt and $apoE^{-/-}$ lung reveal diverse distributions for the *n*-9 and the *n*-7 isomer of PC 34:1 (Figure 17). Except for the intensity gaps at the lumen of the bronchi, DB-derived fragments of PC 34:1 *n*-9 were almost homogenously detected throughout the measured tissue area. On the contrary, PC 34:1 *n*-7 was found enriched in the bronchi epithelial cells, protruding in the lumen of the bronchi.

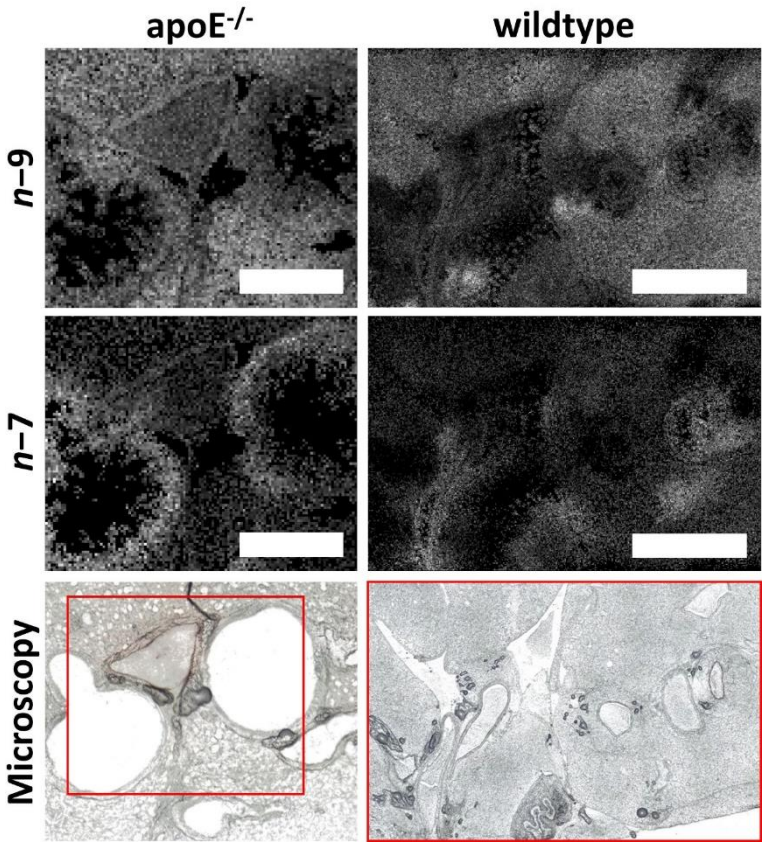

Figure 17: MALDI-MS^2 images of the DBPI-diagnostic fragment ions of PC 34:1 (*n*-9) and PC 34:1 (*n*-7) in $apoE^{-/-}$ and wt mouse lung tissue. Pixel sizes: 15 µm ($apoE^{-/-}$) and 20 µm (wildtype). Signal intensities were TIC normalized. Lower row: Optical microscopic images of tissue sections before measurement. Scale bars reflect 0.6 mm ($apoE^{-/-}$) and 2 mm (wildtype).

4. Conclusion

The aim of this work was to develop a workflow for the on-tissue PB functionalization of lipids to shed light on DBPI distributions by MALDI-MS^2I experiments in biological tissue samples. PB reagents were applied as MALDI matrices onto samples and were photo-activated by the MALDI-laser irradiation, triggering the PB functionalization of the lipid DBs. Subsequent collisional activation of the PB products enabled the acquisition of DBPI-resolved MALDI-MS^2 images with down to 10 µm lateral resolution.

The approach to fulfill the initial goal of using AcPh as an on-tissue PB reagent was the application of AcPh thin films onto UV-irradiated tissue samples. Although the optimization of the reagent deposition reduced wash-out effects and led to the observation of PB functionalization, the PB yield was too low for MS^2I. Neither benzaldehyde nor 2,5-dihydroxyacetophenone produced sufficient amounts of PB derivatized lipids. That is why BPh was tested next and indeed, dropping BPh-solutions onto samples and subsequent UV irradiation gave higher PB yields of 20% (compared to 5.6% with AcPh). The next target was to tackle wash-out issues and to achieve homogenous BPh application. It was achieved by pneumatic spraying of BPh solutions onto UV-irradiated samples. After few optimizations of the BPh concentration and the solvent mixture, the pneumatic-spraying-based PB method yielded a DBPI-resolved MALDI-MS^2 image of histological tissue features in mouse cerebellum. In an experiment without DHB as supporting MALDI matrix, BPh was shown to function as a MALDI matrix itself. Spectra with only one order of magnitude lower intensities than with DHB were obtained that were at the same time cleaner regarding interfering matrix-derived signals. BPh was therefore used as PB-reactive matrix, avoiding the need for any additional MALDI matrix. Consequently, the aim was now to optimize the BPh spraying protocol for maximal lateral resolution and PB yield. The spraying parameters (the concentration of BPh and the ionization-assisting trifluoracetic acid (TFA), the solvent composition, the UV irradiation time, the overall sprayed volume, the spraying flowrate, the sample-to-spraying-needle distance, the sample-to-UV-lamp distance, the strength of the nebulizing-gas flow (N_2) and the rotational speed of the sample holder) were optimized, enabling small matrix crystals (∼15 µm) and high ionization- (∼10^5 normalized level) and derivatization-efficiencies (> 15%).

During the optimization of the spraying protocol, PB products were found in spectra of samples that were not irradiated with a UV lamp. HPLC-ESI-MS measurements of the extracts of samples that were prepared the same way did only show very low PB yields. This and a discovered correlation between PB yield and the applied MALDI laser energy supported the assumption of the PB functionalization being activated by the MALDI laser. The normalized levels in spectra of samples prepared without UV-lamp irradiation were higher than those with a UV lamp. As a consequence, absolute PB product ion counts were higher without UV irradiation unless the PB yield is lower. The UV lamp was thus removed

from the sample preparation setup. In the first publication of the project, BPh was introduced as a novel PB-reactive MALDI matrix that enables lipid DBPI resolution. Besides showing BPh's suitability for the DBPI analysis of standards of 6 lipid classes (PC, PE, PI, PA, PG, and SM), BPh was shown to be sufficient for high resolution (15 µm pixel size) MSI and DBPI-resolving MS^2I. Comparing the MS images of mouse cerebellum with BPh versus DHB as matrix revealed similar lipid coverages and lateral distributions. In sum, 92/74 lipids were assigned in mouse cerebellum by using DHB/BPh as matrix and BPh was observed to promote protonated signals whereas DHB showed more alkali metal adducts. MS^2 images of whole *S. mansoni* worms uncovered elevated concentrations of the special *n*-13 isomer in the parasite's head and tail region.

Intending to improve the PB-reactive matrix approach, various BPh derivatives were screened and compared in terms of ionization and functionalization efficiency. In the second publication of the project, the results of the screening were presented and BzPy was introduced as new PB-reactive matrix that outperforms BPh in the above-defined analytical figures of merit. Whereas hydroxy- and amino derivatives of BPh provided high ion intensities but no PB products, pyridine derivatives like BzPy enhanced ion intensities and PB yields. Furthermore, the basic pyridine moieties facilitated protonation of lipid-matrix adducts. So, protonated BzPy-adducts of PG, CL and TG standards can be detected while no signals appeared for $[PG+H]^+$, $[CL+H]^+$ or $[TG+H]^+$ without BzPy attachment. Complementing the scope of BPh (6 lipid classes), BzPy additionally enabled the DBPI analysis of FAs, SHexCers, PSs, HexCers, CLs, TGs, and plasmalogen PCs (13 lipid classes). Localizing DBs in the negative-ion mode was shown for the first time for FA and SHexCer standards and for a SHexCer from tissue. Replacing BPh by BzPy improved the lateral resolution (15 µm versus 7 µm) in MALDI-MS images and with BzPy as a dual-polarity matrix, 133/58 lipids were assigned for mouse cerebellum tissue in the positive/negative-ion mode, respectively. Higher resolutions (10 µm) of DBPI-resolved MS^2 images allowed to unveil the lateral distributions of the DBPIs of various unsaturated lipids in the islets of Langerhans in mouse pancreas tissue sections.

In the final part of the project, the long-term goal of medical and routine application has been addressed by studying diabetes- and cardiovascular-disease-model mouse tissue. Because of the found differences of lateral DBPI distributions in pancreatic islets, DBPI ratios in these regions of wt and diabetic-mouse pancreas tissue were investigated and compared. The *n*-9/*n*-7 ratio of PC 34:1 was lower in diabetic islets of Langerhans, suggesting altered roles of the isomers. Another medical application was the study of lipid profiles in lung tissue of $apoE^{-/-}$ mice which are model mice for atherosclerosis research. Lipids were annotated by means of accurate *m*/*z* measurements in the MSI data and the images were examined for signal elevations and depletions that were then matched to histological regions. Regions of higher and lower lipid signal intensities were identified to be blood

vessels and bronchi. In these histological structures, also the abundances of distinct DBPIs varied: The PC 34:1 *n*-7 isomer showed higher concentrations in the epithelium of the bronchi than in the surrounding tissue, whereas the PC 34:1 *n*-9 isomer was homogenously distributed.

Matrix screening experiments indicated that electron donating substituents like hydroxy and amino groups hinder the PB functionalization of lipids, whereas BPh derivatives with lower electron density in the aromatic system are more reactive than BPh. These trends can help further screening experiments to find more reactive matrices and matrices with other desired advantages for structural lipid analysis.

5. Outlook

It was shown in this work that the PB functionalization of lipids is compatible with MALDI-MSI by using PB-reactive matrices. The developed sample preparation method enables dual-polarity MALDI-MSI and DBPI-resolved MS^2I from biological samples. Due to this multifunctionality, the matrix can be deployed for common lipidomics without DBPI resolution while it also provides the option to fragment PB products for DBPI imaging. Especially, BzPy can support common MS^1I because of the protonation boost effect exerted by the basic nitrogen. This can help future lipidomics studies to image, e.g., TGs that are hard to detect without BzPy-adduction. In principle, the protonation boost can be applied to all molecules that form adducts with BzPy. In follow up studies, reactive matrices should be screened to find more of such sensitivity-enhancing matrices for lipids and other biochemical species. Matrices showing high ion yields in preceding screening experiments but were discarded for the lack of PB reactivity, should be reviewed for their ionization ability in other applications than PB functionalization.

Because the DBPI-resolved MS^2I often fails due to low PB product intensities, new matrices with higher ionization and/or functionalization efficiency would enable the DBPI resolution of less abundant lipids. Apart from that, optimized sample preparation methods as, e.g., recrystallization of the matrix layer or additional washing steps have to be considered to extend the lipid class scope that is accessible in MSI experiments with DBPI resolution. The already used ammonium formate washing could be complemented or replaced by other procedures that, for example, wash away polar and charged lipids to avoid the suppression of unpolar lipids like TGs. Recrystallization is expected to enhance the ionization efficiency of lipids when they co-crystallize with the matrix.[143] The development of a recrystallization protocol requires to optimize the composition of the recrystallization solution, the recrystallization time and the pressure of the recrystallization chamber.

Analyzing DBPIs in the negative-ion mode is challenging because the intensities of DB fragmentation-derived ions is low. Although it has been demonstrated that DB positions can be uncovered with the aid of BzPy as PB-reactive matrix, the fragment ion intensities did not suffice for DBPI-resolved MS^2I yet. To address this, PB-reactive matrices that boost negative-ion intensities, such as negatively charged matrix materials, are needed. By using the charged matrix BzPy, ω_E-fragments (remaining FA chain residue coupled to the charged matrix) were observed in this work. Negatively charged matrices could allow detecting this fragment type in the negative-ion mode. DBPI analysis of favorable negatively charged lipids such as FAs, SHexCers, PIs, etc. could be accessible by using ω_E-fragments in future projects. 4-Benzoylbenzoic acid, for example, was already tested in the screening experiments of this work and showed approximately 12% PB yield with a PC 18:1/18:1 standard in the positive-ion

mode. As 4-benzoylbenzoic acid is readily deprotonated, this PB-reactive matrix could help to overcome the challenge of DBPI-resolved MS^2I in the negative-ion mode.

In the conducted shotgun lipidomics experiments, many lipids could not be analyzed by MS^2 because their signals were superimposed by more abundant or more-readily ionized lipids. Combining shotgun lipidomics with parallel HPLC-MS and -MS^2 runs to confirm shotgun annotations and to find additional species would allow a more complete lipidomic picture of tissue samples. Routine methods including (A) imaging and (B) HPLC protocols should be the long-term goal to transfer the methodology from specialized laboratories to routine analysis, performed by briefly trained technicians. The protocols should cover all parameters, pitfalls and troubleshooting of (A) embedding, sectioning, washing steps, matrix application, MS measurement, image processing as well as the annotation of lipid species and (B) lipid extraction, HPLC (column, eluent, gradient, etc.) and MS measurement.

The search for new matrices would benefit from a comprehensive understanding of the processes occurring in the MALDI-triggered PB reaction observed in this work. Mechanistic details of the PB reaction are still discussed and new questions arose during the course of our studies: Does the reaction happen in the solid- or gas-phase or in matrix-analyte clusters of the MALDI plume? Can the found regioselectivity contribute to the understanding of the PB reaction? Can our data complement the available data for PB reactions of pyridine-substituted carbonyls? When electron-donating substitution lowers the PB reactivity of the matrix – why is this the case? Turro et al. consider two mechanistic paths for the carbonyl's $n\pi^*$ state reacting in the PB reaction: (1) The semi-occupied π^* orbital reacts as a nucleophile or (2) the semi-occupied non-binding n_p orbital of the carbonyl oxygen reacts as an electrophile.[214] Our experiments indicate that higher electron density led to lower PB reactivity. Consequently, path (2) is suggested to be the favored path. Other explanations could be that the electron donating groups vary the energy of the carbonyl's HOMO in an unfavorable manner or that they impede the ISC of the excited carbonyl. In order to answer these questions, more experiments using BPh derivatives with systematically varied electronic structure are needed. The used halogen-substituted BPh derivatives led to ambiguous results most likely because electron-donating mesomeric effects masked electron-withdrawing inductive effects. This could be tackled by employing trihalogenomethyl-substituted derivatives instead of halogen-substituted ones because the former cannot exert a mesomeric effect. Furthermore, theoretical calculations, i.e., computational chemistry should also be considered to support the mechanistic studies like Guerra et al. recently did for the PB reaction of formaldehyde and ethylene.[215]

In a preceding study, PB functionalization with AcPh and UVPD-MS^2 were combined. Compared to CID-MS^2, UVPD showed higher selectivity for DB fragmentation. Consequently, it is worth testing the UVPD-fragmentation performance with BPh- or BzPy-functionalized lipids. If the higher selectivity of UVPD is

observed here too and DB fragment ion intensities are increased, this could help to image DBPIs of low-abundance lipids as well. The Brodbelt group lately published a UVPD workflow with a subsequent precursor exclusion to enhance the signal-to-noise ratio of DB fragment ions.[216] By applying a wide isolation window including the fragment ion but excluding the precursor, the orbitrap is loaded with less ions which, according to the authors, reduces space-charging and dephasing[217] effects. This can easily be adapted to the developed PB methodology by using an MS^n-capable ion-trap mass spectrometer.

Because neither in CID nor in UVPD DB-fragmentation is the main fragmentation path, other more intense fragment ions like head group losses disturb DBPI analysis. If the oxetane of the PB functionalization remains intact after head group detachment, it can be fragmented in an MS^3 step to finally yield DB-derived fragment ions. Apart from this, Cao et al. showed that *sn*-isomerism can be resolved by CID of head group loss fragments of lipids that were PB-functionalized with 2-AcPy.[110] These findings motivate to apply the CID-MS^3 workflow to the BzPy-functionalized lipids used in the work at hand.

Besides the method optimization for higher lateral resolution, increased ionization and functionalization efficiency and more lipid classes accessible for DBPI analysis, the developed technique has to be applied to biochemical and medical issues. Initial results for $apoE^{-/-}$ mouse lung tissue and the lateral DBPI distributions in diabetic mouse pancreas call for further surveys to acquire reliable trends for the DBPI ratios in wt compared to diseased tissue. Studying variations in DBPI ratios and lateral distributions can help to infer disease-induced changes of the activities of enzymes and proteins like, for example, desaturases, elongases, FA-binding proteins, acyltransferases and phospholipases.[95,218] Lipid isomers consequently can serve as disease biomarkers to assist diagnosis and precise treatment.

6. References

(1) Blanksby, S. J.; Mitchell, T. W. Advances in mass spectrometry for lipidomics. *Annu. Rev. Anal. Chem.* **2010**, *3*, 433–465. DOI: 10.1146/annurev.anchem.111808.073705.

(2) Vailati-Riboni, M.; Palombo, V.; Loor, J. J. What Are Omics Sciences? In *Periparturient Diseases of Dairy Cows: A Systems Biology Approach*; Ametaj, B. N., Ed.; Springer International Publishing, 2017; pp 1–7. DOI: 10.1007/978-3-319-43033-1_1.

(3) Moss, G. P.; Smith, P. A. S.; Tavernier, D. Glossary of class names of organic compounds and reactivity intermediates based on structure (IUPAC Recommendations 1995). *Pure Appl. Chem.* **1995**, *67* (8-9), 1307–1375. DOI: 10.1351/pac199567081307.

(4) Züllig, T.; Köfeler, H. C. High Resolution Mass Spectrometry in Lipidomics. *Mass Spectrom. Rev.* **2021**, *40* (3), 162–176. DOI: 10.1002/mas.21627. Published Online: Mar. 31, 2020.

(5) Gross, R. W. The evolution of lipidomics through space and time. *BBA-Mol. Cell Biol. L.* **2017**, *1862* (8), 731–739. DOI: 10.1016/j.bbalip.2017.04.006. Published Online: Apr. 28, 2017.

(6) Liebisch, G.; Fahy, E.; Aoki, J.; Dennis, E. A.; Durand, T.; Ejsing, C. S.; Fedorova, M.; Feussner, I.; Griffiths, W. J.; Köfeler, H.; Merrill, A. H.; Murphy, R. C.; O'Donnell, V. B.; Oskolkova, O.; Subramaniam, S.; Wakelam, M. J. O.; Spener, F. Update on LIPID MAPS classification, nomenclature, and shorthand notation for MS-derived lipid structures. *J. Lipid Res.* **2020**, *61* (12), 1539–1555. DOI: 10.1194/jlr.S120001025. Published Online: Oct. 9, 2020.

(7) Phillips, R.; Ursell, T.; Wiggins, P.; Sens, P. Emerging roles for lipids in shaping membrane-protein function. *Nature* **2009**, *459* (7245), 379–385. DOI: 10.1038/nature08147.

(8) Craene, J.-O. de; Bertazzi, D. L.; Bär, S.; Friant, S. Phosphoinositides, Major Actors in Membrane Trafficking and Lipid Signaling Pathways. *Int. J. Mol. Sci.* **2017**, *18* (3). DOI: 10.3390/ijms18030634. Published Online: Mar. 15, 2017.

(9) Coffey, J. W.; Duve, C. de. Digestive Activity of Lysosomes. *J. Biol. Chem.* **1968**, *243* (12), 3255–3263. DOI: 10.1016/S0021-9258(18)93301-6.

(10) Mindell, J. A. Lysosomal acidification mechanisms. *Annu. Rev. Physiol.* **2012**, *74*, 69–86. DOI: 10.1146/annurev-physiol-012110-142317.

(11) Wang, X.; Devaiah, S. P.; Zhang, W.; Welti, R. Signaling functions of phosphatidic acid. *Prog. Lipid Res.* **2006**, *45* (3), 250–278. DOI: 10.1016/j.plipres.2006.01.005. Published Online: Mar. 15, 2006.

(12) Thomas, A. Lipids: defining the shape of things to come. *Nat. Cell Biol.* **1999**, *1* (8), E192. DOI: 10.1038/70219.

(13) Yarwood, R.; Hellicar, J.; Woodman, P. G.; Lowe, M. Membrane trafficking in health and disease. *Dis. Model Mech.* **2020**, *13* (4). DOI: 10.1242/dmm.043448. Published Online: Apr. 30, 2020.

(14) Lee, A. G. Biological membranes: the importance of molecular detail. *Trends Biochem. Sci.* **2011**, *36* (9), 493–500. DOI: 10.1016/j.tibs.2011.06.007. Published Online: Aug. 18, 2011.

(15) Welte, M. A.; Gould, A. P. Lipid droplet functions beyond energy storage. *BBA-Mol. Cell Biol. L.* **2017**, *1862* (10 Pt B), 1260–1272. DOI: 10.1016/j.bbalip.2017.07.006. Published Online: Jul. 19, 2017.

(16) Mellors, A.; Tappel, A. L. Hydrolysis of phospholipids by a lysosomal enzyme. *J. Lipid Res.* **1967**, *8* (5), 479–485. DOI: 10.1016/S0022-2275(20)38905-7.

(17) Piret, J.; Schanck, A.; Delfosse, S.; van Bambeke, F.; Kishore, B. K.; Tulkens, P. M.; Mingeot-Leclercq, M.-P. Modulation of the in vitro activity of lysosomal phospholipase A1 by membrane lipids. *Chem. Phys. Lipids* **2005**, *133* (1), 1–15. DOI: 10.1016/j.chemphyslip.2004.08.002.

(18) Zhang, W.; Qin, C.; Zhao, J.; Wang, X. Phospholipase D alpha 1-derived phosphatidic acid interacts with ABI1 phosphatase 2C and regulates abscisic acid signaling. *Proc. Natl. Acad. Sci. USA* **2004**, *101* (25), 9508–9513. DOI: 10.1073/pnas.0402112101. Published Online: Jun. 14, 2004.

(19) International Diabetes Federation. IDF Diabetes Atlas. *IDF Diabetes Atlas* **2021**, *10*.

(20) Erion, D. M.; Shulman, G. I. Diacylglycerol-mediated insulin resistance. *Nat. Med.* **2010**, *16* (4), 400–402. DOI: 10.1038/nm0410-400.

(21) DeFronzo, R. A.; Ferrannini, E.; Groop, L.; Henry, R. R.; Herman, W. H.; Holst, J. J.; Hu, F. B.; Kahn, C. R.; Raz, I.; Shulman, G. I.; Simonson, D. C.; Testa, M. A.; Weiss, R. Type 2 diabetes mellitus. *Nat. Rev.* **2015**, *1*, 15019. DOI: 10.1038/nrdp.2015.19. Published Online: Jul. 23, 2015.

(22) Shi, H.; Kokoeva, M. V.; Inouye, K.; Tzameli, I.; Yin, H.; Flier, J. S. TLR4 links innate immunity and fatty acid-induced insulin resistance. *J. Clin. Invest.* **2006**, *116* (11), 3015–3025. DOI: 10.1172/JCI28898. Published Online: Oct. 19, 2006.

(23) Sameer, A. S.; Nissar, S. Toll-Like Receptors (TLRs): Structure, Functions, Signaling, and Role of Their Polymorphisms in Colorectal Cancer Susceptibility. *Biomed. Res. Int.* **2021**, *2021*, 1157023. DOI: 10.1155/2021/1157023. Published Online: Sep. 12, 2021.

(24) Choi, C. S.; Savage, D. B.; Abu-Elheiga, L.; Liu, Z.-X.; Kim, S.; Kulkarni, A.; Distefano, A.; Hwang, Y.-J.; Reznick, R. M.; Codella, R.; Zhang, D.; Cline, G. W.; Wakil, S. J.; Shulman, G. I. Continuous fat oxidation in acetyl-CoA carboxylase 2 knockout mice increases total energy expenditure, reduces fat mass, and improves insulin sensitivity. *Proc. Natl. Acad. Sci. USA* **2007**, *104* (42), 16480–16485. DOI: 10.1073/pnas.0706794104. Published Online: Oct. 8, 2007.

(25) Galadari, S.; Rahman, A.; Pallichankandy, S.; Galadari, A.; Thayyullathil, F. Role of ceramide in diabetes mellitus: evidence and mechanisms. *Lipids Health Dis.* **2013**, *12*, 98. DOI: 10.1186/1476-511X-12-98. Published Online: Jul. 8, 2013.

(26) Tuppy, H.; Kreil, G. Cytochrome c. In *Encyclopedia of Biological Chemistry*; Elsevier, 2013; pp 599–601. DOI: 10.1016/B978-0-12-378630-2.00374-1.

(27) Eizirik, D. L.; Pasquali, L.; Cnop, M. Pancreatic β-cells in type 1 and type 2 diabetes mellitus: different pathways to failure. *Nat. Rev.* **2020**, *16* (7), 349–362. DOI: 10.1038/s41574-020-0355-7. Published Online: May. 12, 2020.

(28) Chatterjee, S.; Khunti, K.; Davies, M. J. Type 2 diabetes. *Lancet* **2017**, *389* (10085), 2239–2251. DOI: 10.1016/S0140-6736(17)30058-2.

(29) Gilbert, M. Role of skeletal muscle lipids in the pathogenesis of insulin resistance of obesity and type 2 diabetes. *J. Diabetes Investig.* **2021**, *12* (11), 1934–1941. DOI: 10.1111/jdi.13614. Published Online: Jul. 17, 2021.

(30) Chamroonkiadtikun, P.; Ananchaisarp, T.; Wanichanon, W. The triglyceride-glucose index, a predictor of type 2 diabetes development: A retrospective cohort study. *Prim. Care Diabetes* **2020**, *14* (2), 161–167. DOI: 10.1016/j.pcd.2019.08.004. Published Online: Aug. 26, 2019.

(31) Lu, J.; Lam, S. M.; Wan, Q.; Shi, L.; Huo, Y.; Chen, L.; Tang, X.; Li, B.; Wu, X.; Peng, K.; Li, M.; Wang, S.; Xu, Y.; Xu, M.; Bi, Y.; Ning, G.; Shui, G.; Wang, W. High-Coverage Targeted Lipidomics Reveals Novel Serum Lipid Predictors and Lipid Pathway Dysregulation Antecedent to Type 2 Diabetes Onset in Normoglycemic Chinese Adults. *Diabetes Care* **2019**, *42* (11), 2117–2126. DOI: 10.2337/dc19-0100. Published Online: Aug. 27, 2019.

(32) Mendis, S.; Puska, P.; Norrving, B. *Global atlas on cardiovascular disease prevention and control*; World Health Organization in collaboration with the World Heart Federation and the World Stroke Organization, 2011.

(33) Kuhlmann, I.; Chin, D.; Rimbach, G. *Prävention kardiovaskulärer Erkrankungen und Atherosklerose*; Springer Fachmedien Wiesbaden, 2014. DOI: 10.1007/978-3-658-08359-5.

(34) Bäck, M.; Hansson, G. Basic Mechanisms of Atherosclerosis. In *Chronic Coronary Artery Disease*; Elsevier, 2018; pp 45–54. DOI: 10.1016/B978-0-323-42880-4.00004-2.

(35) Satyanarayana, U. *Biochemistry*, 4th ed.; Elsevier Science & Technology, 2013.

(36) Cui, M.-Z. Lysophosphatidic acid effects on atherosclerosis and thrombosis. *Clin. Lipidol.* **2011**, *6* (4), 413–426. DOI: 10.2217/clp.11.38.

(37) Hayashi, K.; Takahashi, M.; Nishida, W.; Yoshida, K.; Ohkawa, Y.; Kitabatake, A.; Aoki, J.; Arai, H.; Sobue, K. Phenotypic modulation of vascular smooth muscle cells induced by unsaturated lysophosphatidic acids. *Circ. Res.* **2001**, *89* (3), 251–258. DOI: 10.1161/hh1501.094265.

(38) Liu, Y.; Chen, F.; Ji, L.; Zhang, L.; Xu, Y.-J.; Dhalla, N. S. Role of lysophosphatidic acid in vascular smooth muscle cell proliferation. *Can. J. Physiol. Pharmacol.* **2020**, *98* (2), 103–110. DOI: 10.1139/cjpp-2019-0264. Published Online: Aug. 1, 2019.

(39) Damirin, A.; Tomura, H.; Komachi, M.; Liu, J.-P.; Mogi, C.; Tobo, M.; Wang, J.-Q.; Kimura, T.; Kuwabara, A.; Yamazaki, Y.; Ohta, H.; Im, D.-S.; Sato, K.; Okajima, F. Role of lipoprotein-associated lysophospholipids in migratory activity of coronary artery smooth muscle cells. *Am. J. Physiol. Heart Circ. Physiol.* **2007**, *292* (5), H2513-22. DOI: 10.1152/ajpheart.00865.2006. Published Online: Jan. 19, 2007.

(40) Morris, A. J.; Smyth, S. S. Lysophosphatidic acid and cardiovascular disease: seeing is believing. *J. Lipid Res.* **2013**, *54* (5), 1153–1155. DOI: 10.1194/jlr.E037887. Published Online: Mar. 18, 2013.

(41) Bot, I.; Shi, G.-P.; Kovanen, P. T. Mast cells as effectors in atherosclerosis. *Arterioscler. Thromb. Vasc. Biol.* **2015**, *35* (2), 265–271. DOI: 10.1161/ATVBAHA.114.303570. Published Online: Aug. 7, 2014.

(42) Bot, M.; Jager, S. C. A. de; MacAleese, L.; Lagraauw, H. M.; van Berkel, T. J. C.; Quax, P. H. A.; Kuiper, J.; Heeren, R. M. A.; Biessen, E. A. L.; Bot, I. Lysophosphatidic acid triggers mast cell-driven atherosclerotic plaque destabilization by increasing vascular inflammation. *J. Lipid Res.* **2013**, *54* (5), 1265–1274. DOI: 10.1194/jlr.M032862. Published Online: Feb. 10, 2013.

(43) Liu, P.; Zhu, W.; Chen, C.; Yan, B.; Zhu, L.; Chen, X.; Peng, C. The mechanisms of lysophosphatidylcholine in the development of diseases. *Life Sci.* **2020**, *247*, 117443. DOI: 10.1016/j.lfs.2020.117443. Published Online: Feb. 19, 2020.

(44) Matsumoto, T.; Kobayashi, T.; Kamata, K. Role of lysophosphatidylcholine (LPC) in atherosclerosis. *Curr. Med. Chem.* **2007**, *14* (30), 3209–3220. DOI: 10.2174/092986707782793899.

(45) Knuplez, E.; Marsche, G. An Updated Review of Pro- and Anti-Inflammatory Properties of Plasma Lysophosphatidylcholines in the Vascular System. *Int. J. Mol. Sci.* **2020**, *21* (12). DOI: 10.3390/ijms21124501. Published Online: Jun. 24, 2020.

(46) Hou, M.; Xia, M.; Zhu, H.; Wang, Q.; Li, Y.; Xiao, Y.; Zhao, T.; Tang, Z.; Ma, J.; Ling, W. Lysophosphatidylcholine promotes cholesterol efflux from mouse macrophage foam cells via PPARgamma-LXRalpha-ABCA1-dependent pathway associated with apoE. *Cell Biochem. Funct.* **2007**, *25* (1), 33–44. DOI: 10.1002/cbf.1374.

(47) Liu-Wu, Y.; Hurt-Camejo, E.; Wiklund, O. Lysophosphatidylcholine induces the production of IL-1β by human monocytes. *Atherosclerosis* **1998**, *137* (2), 351–357. DOI: 10.1016/S0021-9150(97)00295-5.

(48) Rao, S. P.; Riederer, M.; Lechleitner, M.; Hermansson, M.; Desoye, G.; Hallström, S.; Graier, W. F.; Frank, S. Acyl chain-dependent effect of lysophosphatidylcholine on endothelium-dependent vasorelaxation. *PloS one* **2013**, *8* (5), e65155. DOI: 10.1371/journal.pone.0065155. Published Online: May. 31, 2013.

(49) Stegemann, C.; Drozdov, I.; Shalhoub, J.; Humphries, J.; Ladroue, C.; Didangelos, A.; Baumert, M.; Allen, M.; Davies, A. H.; Monaco, C.; Smith, A.; Xu, Q.; Mayr, M. Comparative lipidomics profiling of human atherosclerotic plaques. *Circ. Cardiovasc. Genet.* **2011**, *4* (3), 232–242. DOI: 10.1161/CIRCGENETICS.110.959098. Published Online: Apr. 21, 2011.

(50) Han, X.; Gross, R. W. Global analyses of cellular lipidomes directly from crude extracts of biological samples by ESI mass spectrometry: a bridge to lipidomics. *J. Lipid Res.* **2003**, *44* (6), 1071–1079. DOI: 10.1194/jlr.R300004-JLR200. Published Online: Apr. 1, 2003.

(51) Lagarde, M.; Géloën, A.; Record, M.; Vance, D.; Spener, F. Lipidomics is emerging. *Biochim. Biophys. Acta* **2003**, *1634* (3), 61. DOI: 10.1016/j.bbalip.2003.11.002.

(52) Malins, D. C.; Mangold, H. K. Analysis of complex lipid mixtures by thin-layer chromatography and complementary methods. *J. Am. Oil Chem. Soc.* **1960**, *37* (11), 576–578. DOI: 10.1007/BF02631604.

(53) Miller, J. M. *Chromatography*:*Concepts and Contrasts*, Second Edition; John Wiley & Sons, Inc, 2009. DOI: 10.1002/9780471980582.

(54) Lange, M.; Ni, Z.; Criscuolo, A.; Fedorova, M. Liquid Chromatography Techniques in Lipidomics Research. *Chromatographia* **2019**, *82* (1), 77–100. DOI: 10.1007/s10337-018-3656-4.

(55) Hinz, C.; Liggi, S.; Griffin, J. L. The potential of Ion Mobility Mass Spectrometry for high-throughput and high-resolution lipidomics. *Curr. Opin. Chem. Biol.* **2018**, *42*, 42–50. DOI: 10.1016/j.cbpa.2017.10.018. Published Online: Nov. 13, 2017.

(56) Gross, J. H. *Massenspektrometrie*; Springer Berlin Heidelberg, 2013. DOI: 10.1007/978-3-8274-2981-0.

(57) March, R. E. An Introduction to Quadrupole Ion Trap Mass Spectrometry. *Org. Mass Spectrom.* **1997**, *32* (4), 351–369. DOI: 10.1002/(SICI)1096-9888(199704)32:4<351:AID-JMS512>3.0.CO;2-Y.

(58) Schwartz, J. C.; Senko, M. W.; Syka, J. E. P. A two-dimensional quadrupole ion trap mass spectrometer. *J. Am. Soc. Mass Spectrom.* **2002**, *13* (6), 659–669. DOI: 10.1016/s1044-0305(02)00384-7.

(59) Makarov. Electrostatic axially harmonic orbital trapping: a high-performance technique of mass analysis. *Anal. Chem.* **2000**, *72* (6), 1156–1162. DOI: 10.1021/ac991131p.

(60) Eliuk, S.; Makarov, A. Evolution of Orbitrap Mass Spectrometry Instrumentation. *Annu. Rev. Anal. Chem.* **2015**, *8*, 61–80. DOI: 10.1146/annurev-anchem-071114-040325.

(61) Yamashita, M.; Fenn, J. B. Electrospray ion source. Another variation on the free-jet theme. *J. Phys. Chem.* **1984**, *88* (20), 4451–4459. DOI: 10.1021/j150664a002.

(62) Karas, M.; Bachmann, D.; Bahr, U.; Hillenkamp, F. Matrix-assisted ultraviolet laser desorption of non-volatile compounds. *Int. J. Mass Spectrom.* **1987**, *78*, 53–68. DOI: 10.1016/0168-1176(87)87041-6.

(63) Karas, M.; Bachmann, D.; Hillenkamp, F. Influence of the wavelength in high-irradiance ultraviolet laser desorption mass spectrometry of organic molecules. *Anal. Chem.* **1985**, *57* (14), 2935–2939. DOI: 10.1021/ac00291a042.

(64) Taylor, G. I.; McEwan, A. D. The stability of a horizontal fluid interface in a vertical electric field. *J. Fluid Mech.* **1965**, *22* (01), 1. DOI: 10.1017/s0022112065000538.

(65) Rayleigh. On the equilibrium of liquid conducting masses charged with electricity. *Phil. Mag.* **1882**, *14* (87), 184–186. DOI: 10.1080/14786448208628425.

(66) Kebarle, P.; Verkerk, U. H. Electrospray: from ions in solution to ions in the gas phase, what we know now. *Mass Spectrom. Rev.* **2009**, *28* (6), 898–917. DOI: 10.1002/mas.20247.

(67) Hsu, F.-F. Mass spectrometry-based shotgun lipidomics - a critical review from the technical point of view. *Anal. Bioanal. Chem.* **2018**, *410* (25), 6387–6409. DOI: 10.1007/s00216-018-1252-y. Published Online: Aug. 9, 2018.

(68) Hancock, S. E.; Poad, B. L. J.; Batarseh, A.; Abbott, S. K.; Mitchell, T. W. Advances and unresolved challenges in the structural characterization of isomeric lipids. *Anal. Biochem.* **2017**, *524*, 45–55. DOI: 10.1016/j.ab.2016.09.014. Published Online: Sep. 17, 2016.

(69) Heiles, S. Advanced tandem mass spectrometry in metabolomics and lipidomics-methods and applications. *Anal. Bioanal. Chem.* **2021**, *413* (24), 5927–5948. DOI: 10.1007/s00216-021-03425-1. Published Online: Jun. 18, 2021.

(70) Brodbelt, J. S. Photodissociation mass spectrometry: new tools for characterization of biological molecules. *Chem. Soc. Rev.* **2014**, *43* (8), 2757–2783. DOI: 10.1039/c3cs60444f. Published Online: Jan. 30, 2014.

(71) Murphy, R. C. *Tandem Mass Spectrometry of Lipids*; Royal Society of Chemistry, 2014. DOI: 10.1039/9781782626350.

(72) Klein, D. R.; Brodbelt, J. S. Structural Characterization of Phosphatidylcholines Using 193 nm Ultraviolet Photodissociation Mass Spectrometry. *Anal. Chem.* **2017**, *89* (3), 1516–1522. DOI: 10.1021/acs.analchem.6b03353. Published Online: Jan. 23, 2017.

(73) Williams, P. E.; Klein, D. R.; Greer, S. M.; Brodbelt, J. S. Pinpointing Double Bond and sn-Positions in Glycerophospholipids via Hybrid 193 nm Ultraviolet Photodissociation (UVPD) Mass Spectrometry. *J. Am. Chem. Soc.* **2017**, *139* (44), 15681–15690. DOI: 10.1021/jacs.7b06416. Published Online: Oct. 25, 2017.

(74) Macias, L. A.; Brodbelt, J. S. Enhanced Characterization of Cardiolipins via Hybrid 193 nm Ultraviolet Photodissociation Mass Spectrometry. *Anal. Chem.* **2022**, *94* (7), 3268–3277. DOI: 10.1021/acs.analchem.1c05071. Published Online: Feb. 8, 2022.

(75) Ryan, E.; Nguyen, C. Q. N.; Shiea, C.; Reid, G. E. Detailed Structural Characterization of Sphingolipids via 193 nm Ultraviolet Photodissociation and Ultra High Resolution Tandem Mass Spectrometry. *J. Am. Soc. Mass Spectrom.* **2017**, *28* (7), 1406–1419. DOI: 10.1007/s13361-017-1668-1. Published Online: Apr. 28, 2017.

(76) Becher, S.; Esch, P.; Heiles, S. Relative Quantification of Phosphatidylcholine sn-Isomers Using Positive Doubly Charged Lipid-Metal Ion Complexes. *Anal. Chem.* **2018**, *90* (19), 11486–11494. DOI: 10.1021/acs.analchem.8b02731. Published Online: Sep. 21, 2018.

(77) Campbell, J. L.; Baba, T. Near-complete structural characterization of phosphatidylcholines using electron impact excitation of ions from organics. *Anal. Chem.* **2015**, *87* (11), 5837–5845. DOI: 10.1021/acs.analchem.5b01460. Published Online: May. 20, 2015.

(78) Baba, T.; Campbell, J. L.; Le Blanc, J. C. Y.; Baker, P. R. S. In-depth sphingomyelin characterization using electron impact excitation of ions from organics and mass spectrometry. *J. Lipid Res.* **2016**, *57* (5), 858–867. DOI: 10.1194/jlr.M067199. Published Online: Mar. 22, 2016.

(79) Baba, T.; Campbell, J. L.; Le Blanc, J. C. Y.; Baker, P. R. S. Structural identification of triacylglycerol isomers using electron impact excitation of ions from organics (EIEIO). *J. Lipid Res.* **2016**, *57* (11), 2015–2027. DOI: 10.1194/jlr.M070177. Published Online: Jul. 25, 2016.

(80) Baba, T.; Campbell, J. L.; Le Blanc, J. C. Y.; Baker, P. R. S. Distinguishing Cis and Trans Isomers in Intact Complex Lipids Using Electron Impact Excitation of Ions from Organics Mass Spectrometry. *Anal. Chem.* **2017**, *89* (14), 7307–7315. DOI: 10.1021/acs.analchem.6b04734. Published Online: Jun. 28, 2017.

(81) Deimler, R. E.; Sander, M.; Jackson, G. P. Radical-induced fragmentation of phospholipid cations using metastable atom-activated dissociation mass spectrometry (MAS-MS). *Int. J. Mass Spectrom.* **2015**, *390*, 178–186. DOI: 10.1016/j.ijms.2015.08.009.

(82) Pham, H. T.; Ly, T.; Trevitt, A. J.; Mitchell, T. W.; Blanksby, S. J. Differentiation of complex lipid isomers by radical-directed dissociation mass spectrometry. *Anal. Chem.* **2012**, *84* (17), 7525–7532. DOI: 10.1021/ac301652a. Published Online: Aug. 22, 2012.

(83) Pham, H. T.; Julian, R. R. Radical delivery and fragmentation for structural analysis of glycerophospholipids. *Int. J. Mass Spectrom.* **2014**, *370*, 58–65. DOI: 10.1016/j.ijms.2014.06.022.

(84) Pham, H. T.; Julian, R. R. Characterization of glycosphingolipid epimers by radical-directed dissociation mass spectrometry. *Analyst* **2016**, *141* (4), 1273–1278. DOI: 10.1039/c5an02383a.

(85) Zhao, X.; Zhang, W.; Zhang, D.; Liu, X.; Cao, W.; Chen, Q.; Ouyang, Z.; Xia, Y. A lipidomic workflow capable of resolving sn- and Cdouble bond, length as m-dashC location isomers of phosphatidylcholines. *Chem. Sci.* **2019**, *10* (46), 10740–10748. DOI: 10.1039/c9sc03521d. Published Online: Oct. 7, 2019.

(86) Zhao, X.; Xia, Y. Characterization of Fatty Acyl Modifications in Phosphatidylcholines and Lysophosphatidylcholines via Radical-Directed Dissociation. *J. Am. Soc. Mass Spectrom.* **2021**, *32* (2), 560–568. DOI: 10.1021/jasms.0c00407. Published Online: Jan. 14, 2021.

(87) Lin, Q.; Li, P.; Jian, R.; Xia, Y. Localization of Intrachain Modifications in Bacterial Lipids Via Radical-Directed Dissociation. *J. Am. Soc. Mass Spectrom.* **2022.** DOI: 10.1021/jasms.2c00011. Published Online: Feb. 23, 2022.

(88) Randolph, C. E.; Blanksby, S. J.; McLuckey, S. A. Toward Complete Structure Elucidation of Glycerophospholipids in the Gas Phase through Charge Inversion Ion/Ion Chemistry. *Anal. Chem.* **2020**, *92* (1), 1219–1227. DOI: 10.1021/acs.analchem.9b04376. Published Online: Dec. 9, 2019.

(89) Kuo, T.-H.; Chung, H.-H.; Chang, H.-Y.; Lin, C.-W.; Wang, M.-Y.; Shen, T.-L.; Hsu, C.-C. Deep Lipidomics and Molecular Imaging of Unsaturated Lipid Isomers: A Universal Strategy Initiated by mCPBA Epoxidation. *Anal. Chem.* **2019**, *91* (18), 11905–11915. DOI: 10.1021/acs.analchem.9b02667. Published Online: Aug. 26, 2019.

(90) Cao, W.; Ma, X.; Li, Z.; Zhou, X.; Ouyang, Z. Locating Carbon-Carbon Double Bonds in Unsaturated Phospholipids by Epoxidation Reaction and Tandem Mass Spectrometry. *Anal. Chem.* **2018**, *90* (17), 10286–10292. DOI: 10.1021/acs.analchem.8b02021. Published Online: Aug. 23, 2018.

(91) Swiner, D. J.; Kulyk, D. S.; Osae, H.; Durisek Iii, G. R.; Badu-Tawiah, A. K. Reactive Thread Spray Mass Spectrometry for Localization of C═C Bonds in Free Fatty Acids: Applications for Obesity Diagnosis. *Anal. Chem.* **2022**, *94* (5), 2358–2365. DOI: 10.1021/acs.analchem.1c03270. Published Online: Jan. 24, 2022.

(92) Zhang, B.; Wang, Y.; Zhou, B.-W.; Cheng, J.; Xu, Q.; Zhang, L.; Sun, T.-Q.; Zhang, J.; Guo, Y.-L. Chloramine-T-Enabled Mass Spectrometric Analysis of C═C Isomers of Unsaturated Fatty Acids and Phosphatidylcholines in Human Thyroids. *Anal. Chem.* **2022**, *94* (16), 6216–6224. DOI: 10.1021/acs.analchem.1c05607. Published Online: Apr. 14, 2022.

(93) Thomas, M. C.; Mitchell, T. W.; Harman, D. G.; Deeley, J. M.; Nealon, J. R.; Blanksby, S. J. Ozone-induced dissociation: elucidation of double bond position within mass-selected lipid ions. *Anal. Chem.* **2008**, *80* (1), 303–311. DOI: 10.1021/ac7017684. Published Online: Dec. 7, 2007.

(94) Paine, M. R. L.; Poad, B. L. J.; Eijkel, G. B.; Marshall, D. L.; Blanksby, S. J.; Heeren, R. M. A.; Ellis, S. R. Mass Spectrometry Imaging with Isomeric Resolution Enabled by Ozone-Induced Dissociation. *Angew. Chem.* **2018**, *57* (33), 10530–10534. DOI: 10.1002/anie.201802937. Published Online: Jun. 19, 2018.

(95) Young, R. S. E.; Bowman, A. P.; Williams, E. D.; Tousignant, K. D.; Bidgood, C. L.; Narreddula, V. R.; Gupta, R.; Marshall, D. L.; Poad, B. L. J.; Nelson, C. C.; Ellis, S. R.; Heeren, R. M. A.; Sadowski, M. C.; Blanksby, S. J. Apocryphal FADS2 activity promotes fatty acid diversification in cancer. *Cell Rep.* **2021**, *34* (6), 108738. DOI: 10.1016/j.celrep.2021.108738.

(96) Paternò, E.; Chieffi, G. Sintesi in chimica organica per mezzo della luce. Nota II. Composti degli idrocarburi non saturi con aldeidi e chetoni. *Gazz. Chim. Ital.* **1909**, *39*, 341–361.

(97) Büchi, G. Light-Catalyzed Organic Reactions .1. The Reaction of Carbonyl Compounds With 2-Methyl-2-Butene in the Presence of Ultraviolet Light. *J. Am. Chem. Soc.* **1954**, *76* (17), 4327–4331.

(98) Ma, X.; Zhang, W.; Li, Z.; Xia, Y.; Ouyang, Z. Enabling High Structural Specificity to Lipidomics by Coupling Photochemical Derivatization with Tandem Mass Spectrometry. *Acc. Chem. Res.* **2021**, *54* (20), 3873–3882. DOI: 10.1021/acs.accounts.1c00419. Published Online: Sep. 27, 2021.

(99) Fréneau, M.; Hoffmann, N. The Paternò-Büchi reaction—Mechanisms and application to organic synthesis. *J. Photoch. Photobio. C* **2017**, *33*, 83–108. DOI: 10.1016/j.jphotochemrev.2017.10.002.

(100) Palmer, I. J.; Ragazos, I. N.; Bernardi, F.; Olivucci, M.; Robb, M. A. An MC-SCF Study of the (Photochemical) Paterno-Buchi Reaction. *J. Am. Chem. Soc.* **1994**, *116* (5), 2121–2132. DOI: 10.1021/ja00084a058.

(101) Ma, X.; Chong, L.; Tian, R.; Shi, R.; Hu, T. Y.; Ouyang, Z.; Xia, Y. Identification and quantitation of lipid C=C location isomers: A shotgun lipidomics approach enabled by photochemical reaction. *Proc. Natl. Acad. Sci. USA* **2016**, *113* (10), 2573–2578. DOI: 10.1073/pnas.1523356113. Published Online: Feb. 22, 2016.

(102) Ren, H.; Triebl, A.; Muralidharan, S.; Wenk, M. R.; Xia, Y.; Torta, F. Mapping the distribution of double bond location isomers in lipids across mouse tissues. *Analyst* **2021**, *146* (12), 3899–3907. DOI: 10.1039/d1an00449b.

(103) Zhang, W.; Zhang, D.; Chen, Q.; Wu, J.; Ouyang, Z.; Xia, Y. Online photochemical derivatization enables comprehensive mass spectrometric analysis of unsaturated phospholipid isomers. *Nat. Commun.* **2019**, *10* (1), 79. DOI: 10.1038/s41467-018-07963-8. Published Online: Jan. 8, 2019.

(104) Jeck, V.; Korf, A.; Vosse, C.; Hayen, H. Localization of double-bond positions in lipids by tandem mass spectrometry succeeding high-performance liquid chromatography with post-column derivatization. *Rapid Commun. Mass Spectrom.* **2019**, *33 Suppl 1*, 86–94. DOI: 10.1002/rcm.8262. Published Online: Sep. 27, 2018.

(105) Zhao, X.; Chen, J.; Zhang, W.; Yang, C.; Ma, X.; Zhang, S.; Zhang, X. Lipid Alterations during Zebrafish Embryogenesis Revealed by Dynamic Mass Spectrometry Profiling with C=C Specificity. *J. Am. Soc. Mass Spectrom.* **2019**, *30* (12), 2646–2654. DOI: 10.1007/s13361-019-02334-z. Published Online: Oct. 18, 2019.

(106) Deng, J.; Yang, Y.; Liu, Y.; Fang, L.; Lin, L.; Luan, T. Coupling Paternò-Büchi Reaction with Surface-Coated Probe Nanoelectrospray Ionization Mass Spectrometry for In Vivo and Microscale Profiling of Lipid C═C

Location Isomers in Complex Biological Tissues. *Anal. Chem.* **2019**, *91* (7), 4592–4599. DOI: 10.1021/acs.analchem.8b05803. Published Online: Mar. 13, 2019.

(107) Tang, F.; Guo, C.; Ma, X.; Zhang, J.; Su, Y.; Tian, R.; Shi, R.; Xia, Y.; Wang, X.; Ouyang, Z. Rapid In Situ Profiling of Lipid C═C Location Isomers in Tissue Using Ambient Mass Spectrometry with Photochemical Reactions. *Anal. Chem.* **2018**, *90* (9), 5612–5619. DOI: 10.1021/acs.analchem.7b04675. Published Online: Apr. 12, 2018.

(108) Wäldchen, F.; Becher, S.; Esch, P.; Kompauer, M.; Heiles, S. Selective phosphatidylcholine double bond fragmentation and localisation using Paternò-Büchi reactions and ultraviolet photodissociation. *Analyst* **2017**, *142* (24), 4744–4755. DOI: 10.1039/c7an01158j.

(109) Esch, P.; Heiles, S. Charging and Charge Switching of Unsaturated Lipids and Apolar Compounds Using Paternò-Büchi Reactions. *J. Am. Soc. Mass Spectrom.* **2018**, *29* (10), 1971–1980. DOI: 10.1007/s13361-018-2023-x. Published Online: Jul. 16, 2018.

(110) Cao, W.; Cheng, S.; Yang, J.; Feng, J.; Zhang, W.; Li, Z.; Chen, Q.; Xia, Y.; Ouyang, Z.; Ma, X. Large-scale lipid analysis with C=C location and sn-position isomer resolving power. *Nat. Commun.* **2020**, *11* (1), 375. DOI: 10.1038/s41467-019-14180-4. Published Online: Jan. 17, 2020.

(111) Li, Z.; Cheng, S.; Lin, Q.; Cao, W.; Yang, J.; Zhang, M.; Shen, A.; Zhang, W.; Xia, Y.; Ma, X.; Ouyang, Z. Single-cell lipidomics with high structural specificity by mass spectrometry. *Nat. Commun.* **2021**, *12* (1), 2869. DOI: 10.1038/s41467-021-23161-5. Published Online: May. 17, 2021.

(112) Karas, M.; Hillenkamp, F. Laser desorption ionization of proteins with molecular masses exceeding 10,000 daltons. *Anal. Chem.* **1988**, *60* (20), 2299–2301. DOI: 10.1021/ac00171a028.

(113) Tanaka, K.; Waki, H.; Ido, Y.; Akita, S.; Yoshida, Y.; Yoshida, T.; Matsuo, T. Protein and polymer analyses up tom/z 100 000 by laser ionization time-of-flight mass spectrometry. *Rapid Commun. Mass Spectrom.* **1988**, *2* (8), 151–153. DOI: 10.1002/rcm.1290020802.

(114) Ehring, H.; Karas, M.; Hillenkamp, F. Role of photoionization and photochemistry in ionization processes of organic molecules and relevance for matrix-assisted laser desorption lonization mass spectrometry. *Org. Mass Spectrom.* **1992**, *27* (4), 472–480. DOI: 10.1002/oms.1210270419.

(115) Spengler, B.; Dolce, J. W.; Cotter, R. J. Infrared laser desorption mass spectrometry of oligosaccharides: fragmentation mechanisms and isomer analysis. *Anal. Chem.* **1990**, *62* (17), 1731–1737. DOI: 10.1021/ac00216a004.

(116) Spengler, B.; Bahr, U.; Karas, M.; Hillenkamp, F. Postionization of Laser-Desorbed Organic and Inorganic Compounds in a Time of Flight Mass Spectrometer. *Instrum. Sci. Technol.* **1988**, *17* (1-2), 173–193. DOI: 10.1080/10739148808543672.

(117) Knochenmuss, R. Ion formation mechanisms in UV-MALDI. *Analyst* **2006**, *131* (9), 966–986. DOI: 10.1039/b605646f. Published Online: Jul. 27, 2006.

(118) Spengler, B.; Karas, M.; Bahr, U.; Hillenkamp, F. Excimer laser desorption mass spectrometry of biomolecules at 248 and 193 nm. *J. Phys. Chem.* **1987**, *91* (26), 6502–6506. DOI: 10.1021/j100310a016.

(119) Bökelmann, V.; Spengler, B.; Kaufmann, R. Dynamical parameters of ion ejection and ion formation in matrix- assisted laser desorption/ionization. *Eur. J. Mass Spectrom.* **1995**, *1* (1), 81. DOI: 10.1255/ejms.163.

(120) Dreisewerd, K. The desorption process in MALDI. *Chem. Rev.* **2003**, *103* (2), 395–426. DOI: 10.1021/cr010375i.

(121) Zenobi, R.; Knochenmuss, R. Ion formation in MALDI mass spectrometry. *Mass Spectrom. Rev.* **1998**, *17* (5), 337–366. DOI: 10.1002/(SICI)1098-2787(1998)17:5<337:AID-MAS2>3.0.CO;2-S.

(122) Karas, M.; Glückmann, M.; Schäfer, J. Ionization in matrix-assisted laser desorption/ionization: singly charged molecular ions are the lucky survivors. *J. Mass Spectrom.* **2000**, *35* (1), 1–12. DOI: 10.1002/(SICI)1096-9888(200001)35:1<1:AID-JMS904>3.0.CO;2-0.

(123) Karas, M.; Krüger, R. Ion formation in MALDI: the cluster ionization mechanism. *Chem. Rev.* **2003**, *103* (2), 427–440. DOI: 10.1021/cr010376a.

(124) Knochenmuss, R. The Coupled Chemical and Physical Dynamics Model of MALDI. *Annu. Rev. Anal. Chem.* **2016**, *9* (1), 365–385. DOI: 10.1146/annurev-anchem-071015-041750. Published Online: Apr. 6, 2016.

(125) Knochenmuss, R.; Zenobi, R. MALDI Ionization: The Role of In-Plume Processes. *ChemInform* **2003**, *34* (18). DOI: 10.1002/chin.200318288.

(126) Frankevich, V.; Zhang, J.; Dashtiev, M.; Zenobi, R. Production and fragmentation of multiply charged ions in 'electron-free' matrix-assisted laser desorption/ionization. *Rapid Commun. Mass Spectrom.* **2003**, *17* (20), 2343–2348. DOI: 10.1002/rcm.1194.

(127) Niu, S.; Zhang, W.; Chait, B. T. Direct comparison of infrared and ultraviolet wavelength matrix-assisted laser desorption/ionization mass spectrometry of proteins. *J. Am. Soc. Mass Spectrom.* **1998**, *9* (1), 1–7. DOI: 10.1016/s1044-0305(97)00236-5.

(128) Chen, X.; Carroll, J. A.; Beavis, R. C. Near-ultraviolet-induced matrix-assisted laser desorption/ionization as a function of wavelength. *J. Am. Soc. Mass Spectrom.* **1998**, *9* (9), 885–891. DOI: 10.1016/s1044-0305(98)00059-2.

(129) Lu, I.-C.; Lee, C.; Lee, Y.-T.; Ni, C.-K. Ionization Mechanism of Matrix-Assisted Laser Desorption/Ionization. *Annu. Rev. Anal. Chem.* **2015**, *8*, 21–39. DOI: 10.1146/annurev-anchem-071114-040315. Published Online: Jun. 24, 2015.

(130) Jaskolla, T. W.; Karas, M. Compelling evidence for Lucky Survivor and gas phase protonation: the unified MALDI analyte protonation mechanism. *J. Am. Soc. Mass Spectrom.* **2011**, *22* (6), 976–988. DOI: 10.1007/s13361-011-0093-0. Published Online: Mar. 8, 2011.

(131) Spengler, B.; Hubert, M.; Kaufmann, R., Eds. *Proceedings of the 42nd ASMS Conference on Mass Spectrometry and Allied Topics*. p 1041, 1994.

(132) Spengler, B. Mass spectrometry imaging of biomolecular information. *Anal. Chem.* **2015**, *87* (1), 64–82. DOI: 10.1021/ac504543v. Published Online: Dec. 18, 2014.

(133) Taylor, A. J.; Dexter, A.; Bunch, J. Exploring Ion Suppression in Mass Spectrometry Imaging of a Heterogeneous Tissue. *Anal. Chem.* **2018**, *90* (9), 5637–5645. DOI: 10.1021/acs.analchem.7b05005. Published Online: Apr. 9, 2018.

(134) Tomlinson, L.; Fuchser, J.; Fütterer, A.; Baumert, M.; Hassall, D. G.; West, A.; Marshall, P. S. Using a single, high mass resolution mass spectrometry platform to investigate ion suppression effects observed during tissue imaging. *Rapid Commun. Mass Spectrom.* **2014**, *28* (9), 995–1003. DOI: 10.1002/rcm.6869.

(135) Annesley, T. M. Ion suppression in mass spectrometry. *Clin. Chem.* **2003**, *49* (7), 1041–1044. DOI: 10.1373/49.7.1041.

(136) Boskamp, M. S.; Soltwisch, J. Charge Distribution between Different Classes of Glycerophospolipids in MALDI-MS Imaging. *Anal. Chem.* **2020**, *92* (7), 5222–5230. DOI: 10.1021/acs.analchem.9b05761. Published Online: Mar. 18, 2020.

(137) Pirman, D. A.; Kiss, A.; Heeren, R. M. A.; Yost, R. A. Identifying tissue-specific signal variation in MALDI mass spectrometric imaging by use of an internal standard. *Anal. Chem.* **2013**, *85* (2), 1090–1096. DOI: 10.1021/ac3029618. Published Online: Dec. 24, 2012.

(138) Lin, M.; Eberlin, L. S.; Seeley, E. H. Reduced Hemoglobin Signal and Improved Detection of Endogenous Proteins in Blood-Rich Tissues for MALDI Mass Spectrometry Imaging. *J. Am. Soc. Mass Spectrom.* **2022**, *33* (2), 296–303. DOI: 10.1021/jasms.1c00300. Published Online: Jan. 21, 2022.

(139) Clemis, E. J.; Smith, D. S.; Camenzind, A. G.; Danell, R. M.; Parker, C. E.; Borchers, C. H. Quantitation of spatially-localized proteins in tissue samples using MALDI-MRM imaging. *Anal. Chem.* **2012**, *84* (8), 3514–3522. DOI: 10.1021/ac202875d. Published Online: Mar. 26, 2012.

(140) Murphy, R. C.; Hankin, J. A.; Barkley, R. M. Imaging of lipid species by MALDI mass spectrometry. *J. Lipid Res.* **2009**, *50 Suppl*, S317-22. DOI: 10.1194/jlr.R800051-JLR200. Published Online: Dec. 2, 2008.

(141) Zhang, J.; Zenobi, R. Matrix-dependent cationization in MALDI mass spectrometry. *J. Mass Spectrom.* **2004**, *39* (7), 808–816. DOI: 10.1002/jms.657.

(142) Wang, H.-Y. J.; Liu, C. B.; Wu, H.-W. A simple desalting method for direct MALDI mass spectrometry profiling of tissue lipids. *J. Lipid Res.* **2011**, *52* (4), 840–849. DOI: 10.1194/jlr.D013060. Published Online: Jan. 24, 2011.

(143) Bouschen, W.; Schulz, O.; Eikel, D.; Spengler, B. Matrix vapor deposition/recrystallization and dedicated spray preparation for high-resolution scanning microprobe matrix-assisted laser desorption/ionization imaging mass spectrometry (SMALDI-MS) of tissue and single cells. *Rapid Commun. Mass Spectrom.* **2010**, *24* (3), 355–364. DOI: 10.1002/rcm.4401.

(144) van Nuffel, S.; Elie, N.; Yang, E.; Nouet, J.; Touboul, D.; Chaurand, P.; Brunelle, A. Insights into the MALDI Process after Matrix Deposition by Sublimation Using 3D ToF-SIMS Imaging. *Anal. Chem.* **2018**, *90* (3), 1907–1914. DOI: 10.1021/acs.analchem.7b03993. Published Online: Jan. 17, 2018.

(145) Wiegelmann, M.; Dreisewerd, K.; Soltwisch, J. Influence of the Laser Spot Size, Focal Beam Profile, and Tissue Type on the Lipid Signals Obtained by MALDI-MS Imaging in Oversampling Mode. *J. Am. Soc. Mass Spectrom.* **2016**, *27* (12), 1952–1964. DOI: 10.1007/s13361-016-1477-y. Published Online: Aug. 22, 2016.

(146) Eiersbrock, F. B.; Orthen, J. M.; Soltwisch, J. Validation of MALDI-MS imaging data of selected membrane lipids in murine brain with and without laser postionization by quantitative nano-HPLC-MS using laser microdissection. *Anal. Bioanal. Chem.* **2020**, *412* (25), 6875–6886. DOI: 10.1007/s00216-020-02818-y. Published Online: Jul. 25, 2020.

(147) van Amstalden Hove, E. R.; Smith, D. F.; Heeren, R. M. A. A concise review of mass spectrometry imaging. *J. Chromatogr. A* **2010**, *1217* (25), 3946–3954. DOI: 10.1016/j.chroma.2010.01.033. Published Online: Feb. 2, 2010.

(148) Perry, W. J.; Patterson, N. H.; Prentice, B. M.; Neumann, E. K.; Caprioli, R. M.; Spraggins, J. M. Uncovering matrix effects on lipid analyses in MALDI imaging mass spectrometry experiments. *J. Mass Spectrom.* **2020**, *55* (4), e4491. DOI: 10.1002/jms.4491. Published Online: Feb. 11, 2020.

(149) Ellis, S. R.; Bruinen, A. L.; Heeren, R. M. A. A critical evaluation of the current state-of-the-art in quantitative imaging mass spectrometry. *Anal. Bioanal. Chem.* **2014**, *406* (5), 1275–1289. DOI: 10.1007/s00216-013-7478-9. Published Online: Nov. 27, 2013.

(150) Tobias, F.; Hummon, A. B. Considerations for MALDI-Based Quantitative Mass Spectrometry Imaging Studies. *J. Proteome Res.* **2020**, *19* (9), 3620–3630. DOI: 10.1021/acs.jproteome.0c00443. Published Online: Aug. 26, 2020.

(151) Takáts, Z.; Wiseman, J. M.; Gologan, B.; Cooks, R. G. Mass spectrometry sampling under ambient conditions with desorption electrospray ionization. *Science* **2004**, *306* (5695), 471–473. DOI: 10.1126/science.1104404.

(152) Roach, P. J.; Laskin, J.; Laskin, A. Nanospray desorption electrospray ionization: an ambient method for liquid-extraction surface sampling in mass spectrometry. *Analyst* **2010**, *135* (9), 2233–2236. DOI: 10.1039/c0an00312c. Published Online: Jun. 30, 2010.

(153) Unsihuay, D.; Mesa Sanchez, D.; Laskin, J. Quantitative Mass Spectrometry Imaging of Biological Systems. *Annu. Rev. Phys. Chem.* **2021**, *72*, 307–329. DOI: 10.1146/annurev-physchem-061020-053416. Published Online: Jan. 13, 2021.

(154) Yin, R.; Burnum-Johnson, K. E.; Sun, X.; Dey, S. K.; Laskin, J. High spatial resolution imaging of biological tissues using nanospray desorption electrospray ionization mass spectrometry. *Nat. Protoc.* **2019**, *14* (12), 3445–3470. DOI: 10.1038/s41596-019-0237-4. Published Online: Nov. 13, 2019.

(155) Henderson, F.; Jones, E.; Denbigh, J.; Christie, L.; Chapman, R.; Hoyes, E.; Claude, E.; Williams, K. J.; Roncaroli, F.; McMahon, A. 3D DESI-MS lipid imaging in a xenograft model of glioblastoma: a proof of principle. *Sci. Rep.* **2020**, *10* (1), 16512. DOI: 10.1038/s41598-020-73518-x. Published Online: Oct. 5, 2020.

(156) Quartier, J.; Rao, W.; Slade, S.; Métral, F.; Lapteva, M.; Kalia, Y. N. DESI-MS imaging to visualize spatial distribution of xenobiotics and endogenous lipids in the skin. *Int. J. Pharm.* **2021**, *607*, 120967. DOI: 10.1016/j.ijpharm.2021.120967. Published Online: Aug. 2, 2021.

(157) Quartier, J.; Capony, N.; Lapteva, M.; Kalia, Y. N. Cutaneous Biodistribution: A High-Resolution Methodology to Assess Bioequivalence in Topical Skin Delivery. *Pharmaceutics* **2019**, *11* (9). DOI: 10.3390/pharmaceutics11090484. Published Online: Sep. 18, 2019.

(158) Kompauer, M.; Heiles, S.; Spengler, B. Atmospheric pressure MALDI mass spectrometry imaging of tissues and cells at 1.4-µm lateral resolution. *Nat. Methods* **2017**, *14* (1), 90–96. DOI: 10.1038/nmeth.4071. Published Online: Nov. 14, 2016.

(159) Niehaus, M.; Soltwisch, J.; Belov, M. E.; Dreisewerd, K. Transmission-mode MALDI-2 mass spectrometry imaging of cells and tissues at subcellular resolution. *Nat. Methods* **2019**, *16* (9), 925–931. DOI: 10.1038/s41592-019-0536-2. Published Online: Aug. 26, 2019.

(160) Soltwisch, J.; Kettling, H.; Vens-Cappell, S.; Wiegelmann, M.; Müthing, J.; Dreisewerd, K. Mass spectrometry imaging with laser-induced postionization. *Science* **2015**, *348* (6231), 211–215. DOI: 10.1126/science.aaa1051. Published Online: Mar. 5, 2015.

(161) Müller, M. A.; Kompauer, M.; Strupat, K.; Heiles, S.; Spengler, B. Implementation of a High-Repetition-Rate Laser in an AP-SMALDI MSI System for Enhanced Measurement Performance. *J. Am. Soc. Mass Spectrom.* **2021**, *32* (2), 465–472. DOI: 10.1021/jasms.0c00368. Published Online: Dec. 28, 2020.

(162) Kompauer, M.; Heiles, S.; Spengler, B. Autofocusing MALDI mass spectrometry imaging of tissue sections and 3D chemical topography of nonflat surfaces. *Nat. Methods* **2017**, *14* (12), 1156–1158. DOI: 10.1038/nmeth.4433. Published Online: Sep. 18, 2017.

(163) Buchberger, A. R.; DeLaney, K.; Johnson, J.; Li, L. Mass Spectrometry Imaging: A Review of Emerging Advancements and Future Insights. *Anal. Chem.* **2018**, *90* (1), 240–265. DOI: 10.1021/acs.analchem.7b04733. Published Online: Dec. 13, 2017.

(164) Paschke, C.; Leisner, A.; Hester, A.; Maass, K.; Guenther, S.; Bouschen, W.; Spengler, B. Mirion—a software package for automatic processing of mass spectrometric images. *J. Am. Soc. Mass Spectrom.* **2013**, *24* (8), 1296–1306. DOI: 10.1007/s13361-013-0667-0. Published Online: Jun. 13, 2013.

(165) Robichaud, G.; Garrard, K. P.; Barry, J. A.; Muddiman, D. C. MSiReader: an open-source interface to view and analyze high resolving power MS imaging files on Matlab platform. *J. Am. Soc. Mass Spectrom.* **2013**, *24* (5), 718–721. DOI: 10.1007/s13361-013-0607-z. Published Online: Mar. 28, 2013.

(166) Dueñas, M. E.; Larson, E. A.; Lee, Y. J. Toward Mass Spectrometry Imaging in the Metabolomics Scale: Increasing Metabolic Coverage Through Multiple On-Tissue Chemical Modifications. *Front. Plant. Sci.* **2019**, *10*, 860. DOI: 10.3389/fpls.2019.00860. Published Online: Jul. 12, 2019.

(167) Geier, B.; Sogin, E. M.; Michellod, D.; Janda, M.; Kompauer, M.; Spengler, B.; Dubilier, N.; Liebeke, M. Spatial metabolomics of in situ host-microbe interactions at the micrometre scale. *Nat. Microbiol.* **2020**, *5* (3), 498–510. DOI: 10.1038/s41564-019-0664-6. Published Online: Feb. 3, 2020.

(168) Tata, A.; Woolman, M.; Ventura, M.; Bernards, N.; Ganguly, M.; Gribble, A.; Shrestha, B.; Bluemke, E.; Ginsberg, H. J.; Vitkin, A.; Zheng, J.; Zarrine-Afsar, A. Rapid Detection of Necrosis in Breast Cancer with Desorption Electrospray Ionization Mass Spectrometry. *Sci. Rep.* **2016**, *6*, 35374. DOI: 10.1038/srep35374. Published Online: Oct. 13, 2016.

(169) Race, A. M.; Palmer, A. D.; Dexter, A.; Steven, R. T.; Styles, I. B.; Bunch, J. SpectralAnalysis: Software for the Masses. *Anal. Chem.* **2016**, *88* (19), 9451–9458. DOI: 10.1021/acs.analchem.6b01643. Published Online: Sep. 22, 2016.

(170) Wijetunge, C. D.; Saeed, I.; Boughton, B. A.; Spraggins, J. M.; Caprioli, R. M.; Bacic, A.; Roessner, U.; Halgamuge, S. K. EXIMS: an improved data analysis pipeline based on a new peak picking method for EXploring Imaging Mass Spectrometry data. *Bioinformatics* **2015**, *31* (19), 3198–3206. DOI: 10.1093/bioinformatics/btv356. Published Online: Jun. 10, 2015.

(171) Bond, N. J.; Koulman, A.; Griffin, J. L.; Hall, Z. massPix: an R package for annotation and interpretation of mass spectrometry imaging data for lipidomics. *Metabolomics* **2017**, *13* (11), 128. DOI: 10.1007/s11306-017-1252-5. Published Online: Sep. 21, 2017.

(172) Schramm, T.; Hester, Z.; Klinkert, I.; Both, J.-P.; Heeren, R. M. A.; Brunelle, A.; Laprévote, O.; Desbenoit, N.; Robbe, M.-F.; Stoeckli, M.; Spengler, B.; Römpp, A. imzML—a common data format for the flexible exchange and processing of mass spectrometry imaging data. *J. Proteomics* **2012**, *75* (16), 5106–5110. DOI: 10.1016/j.jprot.2012.07.026. Published Online: Jul. 26, 2012.

(173) Palmer, A.; Phapale, P.; Chernyavsky, I.; Lavigne, R.; Fay, D.; Tarasov, A.; Kovalev, V.; Fuchser, J.; Nikolenko, S.; Pineau, C.; Becker, M.; Alexandrov, T. FDR-controlled metabolite annotation for high-

resolution imaging mass spectrometry. *Nat. Methods* **2017**, *14* (1), 57–60. DOI: 10.1038/nMeth.4072. Published Online: Nov. 14, 2016.

(174) Dreisbach, D.; Petschenka, G.; Spengler, B.; Bhandari, D. R. 3D-surface MALDI mass spectrometry imaging for visualising plant defensive cardiac glycosides in Asclepias curassavica. *Anal. Bioanal. Chem.* **2021**, *413* (8), 2125–2134. DOI: 10.1007/s00216-021-03177-y. Published Online: Feb. 5, 2021.

(175) Korte, A. R.; Yandeau-Nelson, M. D.; Nikolau, B. J.; Lee, Y. J. Subcellular-level resolution MALDI-MS imaging of maize leaf metabolites by MALDI-linear ion trap-Orbitrap mass spectrometer. *Anal. Bioanal. Chem.* **2015**, *407* (8), 2301–2309. DOI: 10.1007/s00216-015-8460-5. Published Online: Jan. 25, 2015.

(176) Chaurand, P.; Cornett, D. S.; Angel, P. M.; Caprioli, R. M. From whole-body sections down to cellular level, multiscale imaging of phospholipids by MALDI mass spectrometry. *Molecular & cellular proteomics : MCP* **2011**, *10* (2), O110.004259. DOI: 10.1074/mcp.O110.004259. Published Online: Aug. 23, 2010.

(177) Ghezellou, P.; Heiles, S.; Kadesch, P.; Ghassempour, A.; Spengler, B. Venom Gland Mass Spectrometry Imaging of Saw-Scaled Viper, Echis carinatus sochureki, at High Lateral Resolution. *J. Am. Soc. Mass Spectrom.* **2021**, *32* (4), 1105–1115. DOI: 10.1021/jasms.1c00042. Published Online: Mar. 16, 2021.

(178) Bian, Y.; He, M.-Y.; Ling, Y.; Wang, X.-J.; Zhang, F.; Feng, X.-S.; Zhang, Y.; Xing, S.-G.; Li, J.; Qiu, X.; Li, Y.-R. Tissue distribution study of perfluorooctanoic acid in exposed zebrafish using MALDI mass spectrometry imaging. *Environ. Pollut.* **2022**, *293*, 118505. DOI: 10.1016/j.envpol.2021.118505. Published Online: Nov. 13, 2021.

(179) Liu, W.; Nie, H.; Liang, D.; Bai, Y.; Liu, H. Phospholipid imaging of zebrafish exposed to fipronil using atmospheric pressure matrix-assisted laser desorption ionization mass spectrometry. *Talanta* **2020**, *209*, 120357. DOI: 10.1016/j.talanta.2019.120357. Published Online: Sep. 16, 2019.

(180) Bhandari, D. R.; Schott, M.; Römpp, A.; Vilcinskas, A.; Spengler, B. Metabolite localization by atmospheric pressure high-resolution scanning microprobe matrix-assisted laser desorption/ionization mass spectrometry imaging in whole-body sections and individual organs of the rove beetle Paederus riparius. *Anal. Bioanal. Chem.* **2015**, *407* (8), 2189–2201. DOI: 10.1007/s00216-014-8327-1. Published Online: Nov. 26, 2014.

(181) Khalil, S. M.; Römpp, A.; Pretzel, J.; Becker, K.; Spengler, B. Phospholipid Topography of Whole-Body Sections of the Anopheles stephensi Mosquito, Characterized by High-Resolution Atmospheric-Pressure Scanning Microprobe Matrix-Assisted Laser Desorption/Ionization Mass Spectrometry Imaging. *Anal. Chem.* **2015**, *87* (22), 11309–11316. DOI: 10.1021/acs.analchem.5b02781. Published Online: Nov. 2, 2015.

(182) Ferreira, M. S.; Oliveira, D. N. de; Oliveira, R. N. de; Allegretti, S. M.; Vercesi, A. E.; Catharino, R. R. Mass spectrometry imaging: a new vision in differentiating Schistosoma mansoni strains. *J. Mass Spectrom.* **2014**, *49* (1), 86–92. DOI: 10.1002/jms.3308.

(183) Mokosch, A. S.; Gerbig, S.; Grevelding, C. G.; Haeberlein, S.; Spengler, B. High-resolution AP-SMALDI MSI as a tool for drug imaging in Schistosoma mansoni. *Anal. Bioanal. Chem.* **2021**, *413* (10), 2755–2766. DOI: 10.1007/s00216-021-03230-w. Published Online: Mar. 15, 2021.

(184) Basu, S. S.; Regan, M. S.; Randall, E. C.; Abdelmoula, W. M.; Clark, A. R.; Gimenez-Cassina Lopez, B.; Cornett, D. S.; Haase, A.; Santagata, S.; Agar, N. Y. R. Rapid MALDI mass spectrometry imaging for surgical pathology. *NPJ Precis. Oncol.* **2019**, *3*, 17. DOI: 10.1038/s41698-019-0089-y. Published Online: Jul. 4, 2019.

(185) Moerman, A. M.; Visscher, M.; Slijkhuis, N.; van Gaalen, K.; Heijs, B.; Klein, T.; Burgers, P. C.; Rijke, Y. B. de; van Beusekom, H. M. M.; Luider, T. M.; Verhagen, H. J. M.; van der Steen, A. F. W.; Gijsen, F. J. H.; van der Heiden, K.; van Soest, G. Lipid signature of advanced human carotid atherosclerosis assessed by mass spectrometry imaging. *J. Lipid Res.* **2021**, *62*, 100020. DOI: 10.1194/jlr.RA120000974. Published Online: Jan. 6, 2021.

(186) Greco, F.; Quercioli, L.; Pucci, A.; Rocchiccioli, S.; Ferrari, M.; Recchia, F. A.; McDonnell, L. A. Mass Spectrometry Imaging as a Tool to Investigate Region Specific Lipid Alterations in Symptomatic Human Carotid Atherosclerotic Plaques. *Metabolites* **2021**, *11* (4). DOI: 10.3390/metabo11040250. Published Online: Apr. 18, 2021.

(187) Cillero-Pastor, B.; Heeren, R. M. A. Matrix-assisted laser desorption ionization mass spectrometry imaging for peptide and protein analyses: a critical review of on-tissue digestion. *J. Proteome Res.* **2014**, *13* (2), 325–335. DOI: 10.1021/pr400743a. Published Online: Nov. 27, 2013.

(188) Heijs, B.; Holst, S.; Briaire-de Bruijn, I. H.; van Pelt, G. W.; Ru, A. H. de; van Veelen, P. A.; Drake, R. R.; Mehta, A. S.; Mesker, W. E.; Tollenaar, R. A.; Bovée, J. V. M. G.; Wuhrer, M.; McDonnell, L. A. Multimodal Mass Spectrometry Imaging of N-Glycans and Proteins from the Same Tissue Section. *Anal. Chem.* **2016**, *88* (15), 7745–7753. DOI: 10.1021/acs.analchem.6b01739. Published Online: Jul. 14, 2016.

(189) Zhou, Q.; Fülöp, A.; Hopf, C. Recent developments of novel matrices and on-tissue chemical derivatization reagents for MALDI-MSI. *Anal. Bioanal. Chem.* **2021**, *413* (10), 2599–2617. DOI: 10.1007/s00216-020-03023-7. Published Online: Nov. 19, 2020.

(190) Merdas, M.; Lagarrigue, M.; Vanbellingen, Q.; Umbdenstock, T.; Da Violante, G.; Pineau, C. On-tissue chemical derivatization reagents for matrix-assisted laser desorption/ionization mass spectrometry imaging. *Org. Mass Spectrom.* **2021**, *56* (10), e4731. DOI: 10.1002/jms.4731. Published Online: Jun. 2, 2021.

(191) Manier, M. L.; Spraggins, J. M.; Reyzer, M. L.; Norris, J. L.; Caprioli, R. M. A derivatization and validation strategy for determining the spatial localization of endogenous amine metabolites in tissues using MALDI imaging mass spectrometry. *Org. Mass Spectrom.* **2014**, *49* (8), 665–673. DOI: 10.1002/jms.3411.

(192) Toue, S.; Sugiura, Y.; Kubo, A.; Ohmura, M.; Karakawa, S.; Mizukoshi, T.; Yoneda, J.; Miyano, H.; Noguchi, Y.; Kobayashi, T.; Kabe, Y.; Suematsu, M. Microscopic imaging mass spectrometry assisted by on-tissue chemical derivatization for visualizing multiple amino acids in human colon cancer xenografts. *Proteomics* **2014**, *14* (7-8), 810–819. DOI: 10.1002/pmic.201300041. Published Online: Oct. 1, 2013.

(193) Cobice, D. F.; Livingstone, D. E. W.; McBride, A.; MacKay, C. L.; Walker, B. R.; Webster, S. P.; Andrew, R. Quantification of 11β-hydroxysteroid dehydrogenase 1 kinetics and pharmacodynamic effects of inhibitors in brain using mass spectrometry imaging and stable-isotope tracers in mice. *Biochem. Pharmacol.* **2018**, *148*, 88–99. DOI: 10.1016/j.bcp.2017.12.013. Published Online: Dec. 15, 2017.

(194) Takeo, E.; Sugiura, Y.; Uemura, T.; Nishimoto, K.; Yasuda, M.; Sugiyama, E.; Ohtsuki, S.; Higashi, T.; Nishikawa, T.; Suematsu, M.; Fukusaki, E.; Shimma, S. Tandem Mass Spectrometry Imaging Reveals Distinct Accumulation Patterns of Steroid Structural Isomers in Human Adrenal Glands. *Anal. Chem.* **2019**, *91* (14), 8918–8925. DOI: 10.1021/acs.analchem.9b00619. Published Online: Jun. 26, 2019.

(195) Sun, C.; Liu, W.; Geng, Y.; Wang, X. On-Tissue Derivatization Strategy for Mass Spectrometry Imaging of Carboxyl-Containing Metabolites in Biological Tissues. *Anal. Chem.* **2020**, *92* (18), 12126–12131. DOI: 10.1021/acs.analchem.0c02303. Published Online: Aug. 26, 2020.

(196) Iwama, T.; Kano, K.; Saigusa, D.; Ekroos, K.; van Echten-Deckert, G.; Vogt, J.; Aoki, J. Development of an On-Tissue Derivatization Method for MALDI Mass Spectrometry Imaging of Bioactive Lipids Containing Phosphate Monoester Using Phos-tag. *Anal. Chem.* **2021**, *93* (8), 3867–3875. DOI: 10.1021/acs.analchem.0c04479. Published Online: Feb. 12, 2021.

(197) Shariatgorji, M.; Nilsson, A.; Fridjonsdottir, E.; Vallianatou, T.; Källback, P.; Katan, L.; Sävmarker, J.; Mantas, I.; Zhang, X.; Bezard, E.; Svenningsson, P.; Odell, L. R.; Andrén, P. E. Comprehensive mapping of neurotransmitter networks by MALDI-MS imaging. *Nat. Methods* **2019**, *16* (10), 1021–1028. DOI: 10.1038/s41592-019-0551-3. Published Online: Sep. 23, 2019.

(198) Zhang, X.; Mantas, I.; Fridjonsdottir, E.; Andrén, P. E.; Chergui, K.; Svenningsson, P. Deficits in Motor Performance, Neurotransmitters and Synaptic Plasticity in Elderly and Experimental Parkinsonian Mice Lacking GPR37. *Front. Aging Neurosci.* **2020**, *12*, 84. DOI: 10.3389/fnagi.2020.00084. Published Online: Mar. 27, 2020.

(199) Kaya, I.; Brülls, S. M.; Dunevall, J.; Jennische, E.; Lange, S.; Mårtensson, J.; Ewing, A. G.; Malmberg, P.; Fletcher, J. S. On-Tissue Chemical Derivatization of Catecholamines Using 4-(N-Methyl)pyridinium Boronic Acid for ToF-SIMS and LDI-ToF Mass Spectrometry Imaging. *Anal. Chem.* **2018**, *90* (22), 13580–13590. DOI: 10.1021/acs.analchem.8b03746. Published Online: Nov. 5, 2018.

(200) Bednařík, A.; Preisler, J.; Bezdeková, D.; Machálková, M.; Hendrych, M.; Navrátilová, J.; Knopfová, L.; Moskovets, E.; Soltwisch, J.; Dreisewerd, K. Ozonization of Tissue Sections for MALDI MS Imaging of Carbon-Carbon Double Bond Positional Isomers of Phospholipids. *Anal. Chem.* **2020**, *92* (9), 6245–6250. DOI: 10.1021/acs.analchem.0c00641. Published Online: Apr. 25, 2020.

(201) Unsihuay, D.; Su, P.; Hu, H.; Qiu, J.; Kuang, S.; Li, Y.; Sun, X.; Dey, S. K.; Laskin, J. Imaging and Analysis of Isomeric Unsaturated Lipids through Online Photochemical Derivatization of Carbon–Carbon Double Bonds**. *Angew. Chem.* **2021**, *133* (14), 7637–7641. DOI: 10.1002/ange.202016734.

(202) Bednařík, A.; Bölsker, S.; Soltwisch, J.; Dreisewerd, K. An On-Tissue Paternò-Büchi Reaction for Localization of Carbon-Carbon Double Bonds in Phospholipids and Glycolipids by Matrix-Assisted Laser-Desorption-Ionization Mass-Spectrometry Imaging. *Angew. Chem.* **2018**, *57* (37), 12092–12096. DOI: 10.1002/anie.201806635. Published Online: Aug. 20, 2018.

(203) Xu, T.; Pi, Z.; Song, F.; Liu, S.; Liu, Z. Benzophenone used as the photochemical reagent for pinpointing C=C locations in unsaturated lipids through shotgun and liquid chromatography-mass spectrometry approaches. *Anal. Chim. Acta* **2018**, *1028*, 32–44. DOI: 10.1016/j.aca.2018.04.046. Published Online: Apr. 21, 2018.

(204) Yuan, W. Z.; Shen, X. Y.; Zhao, H.; Lam, J. W. Y.; Tang, L.; Lu, P.; Wang, C.; Liu, Y.; Wang, Z.; Zheng, Q.; Sun, J. Z.; Ma, Y.; Tang, B. Z. Crystallization-Induced Phosphorescence of Pure Organic Luminogens at Room Temperature. *J. Phys. Chem. C* **2010**, *114* (13), 6090–6099. DOI: 10.1021/jp909388y.

(205) Wenzel, T.; Sparbier, K.; Mieruch, T.; Kostrzewa, M. 2,5-Dihydroxyacetophenone: a matrix for highly sensitive matrix-assisted laser desorption/ionization time-of-flight mass spectrometric analysis of proteins using manual and automated preparation techniques. *Rapid Commun. Mass Spectrom.* **2006**, *20* (5), 785–789. DOI: 10.1002/rcm.2378.

(206) Wäldchen, F.; Spengler, B.; Heiles, S. Reactive Matrix-Assisted Laser Desorption/Ionization Mass Spectrometry Imaging Using an Intrinsically Photoreactive Paternò-Büchi Matrix for Double-Bond Localization in Isomeric Phospholipids. *J. Am. Chem. Soc.* **2019**, *141* (30), 11816–11820. DOI: 10.1021/jacs.9b05868. Published Online: Jul. 22, 2019.

(207) Daubert, T. E.; Danner, R. P. *Physical and thermodynamic properties of pure chemicals*:*Data compilation*; Taylor & Francis, 1989.

(208) Bridgeman, O. C.; Aldrich, E. W. Vapor Pressure Tables for Water. *J. Heat Tranfer* **1964**, *86* (2), 279–286. DOI: 10.1115/1.3687121.

(209) Boublík, T.; Fried, V.; Hála, E. *The vapour pressures of pure substances*:*Selected values of the temperature dependence of the vapour pressures of some pure substances in the normal and low pressure region*, Reprint; Elsevier, 1975.

(210) Matyash, V.; Liebisch, G.; Kurzchalia, T. V.; Shevchenko, A.; Schwudke, D. Lipid extraction by methyl-tert-butyl ether for high-throughput lipidomics. *J. Lipid Res.* **2008**, *49* (5), 1137–1146. DOI: 10.1194/jlr.D700041-JLR200. Published Online: Feb. 16, 2008.

(211) van Diepen, M. T.; Parsons, M.; Downes, C. P.; Leslie, N. R.; Hindges, R.; Eickholt, B. J. MyosinV controls PTEN function and neuronal cell size. *Nat. Cell Biol.* **2009**, *11* (10), 1191–1196. DOI: 10.1038/ncb1961. Published Online: Sep. 20, 2009.

(212) Lawson, S. N. The postnatal development of large light and small dark neurons in mouse dorsal root ganglia: a statistical analysis of cell numbers and size. *J. Neurocytol.* **1979**, *8* (3), 275–294. DOI: 10.1007/BF01236123.

(213) Wäldchen, F.; Mohr, F.; Wagner, A. H.; Heiles, S. Multifunctional Reactive MALDI Matrix Enabling High-Lateral Resolution Dual Polarity MS Imaging and Lipid C═C Position-Resolved MS2 Imaging. *Anal. Chem.* **2020**, *92* (20), 14130–14138. DOI: 10.1021/acs.analchem.0c03150. Published Online: Sep. 28, 2020.

(214) Turro, N. J.; Dalton, J. C.; Dawes, K.; Farrington, G.; Hautala, R.; Morton, D.; Niemczyk, M.; Schore, N. Molecular photochemistry. L. Molecular photochemistry of alkanones in solution. .alpha.-Cleavage, hydrogen abstraction, cycloaddition, and sensitization reactions. *Acc. Chem. Res.* **1972**, *5* (3), 92–101. DOI: 10.1021/ar50051a002.

(215) Guerra, C.; Ayarde-Henríquez, L.; Duque-Noreña, M.; Chamorro, E. Unraveling the Bonding Nature Along the Photochemically Activated Paterno-Büchi Reaction Mechanism. *ChemPhysChem* **2021**, *22* (22), 2342–2351. DOI: 10.1002/cphc.202100594. Published Online: Sep. 28, 2021.

(216) Shields, S. W. J.; Sanders, J. D.; Brodbelt, J. S. Enhancing the Signal-to-Noise of Diagnostic Fragment Ions of Unsaturated Glycerophospholipids via Precursor Exclusion Ultraviolet Photodissociation Mass

Spectrometry (PEx-UVPD-MS). *Anal. Chem.* **2022.** DOI: 10.1021/acs.analchem.2c02128. Published Online: Aug. 2, 2022.

(217) Makarov, A.; Denisov, E. Dynamics of ions of intact proteins in the Orbitrap mass analyzer. *J. Am. Soc. Mass Spectrom.* **2009**, *20* (8), 1486–1495. DOI: 10.1016/j.jasms.2009.03.024. Published Online: Apr. 5, 2009.

(218) Young, R. S. E.; Bowman, A. P.; Tousignant, K. D.; Poad, B. L. J.; Gunter, J. H.; Philp, L. K.; Nelson, C. C.; Ellis, S. R.; Heeren, R. M. A.; Sadowski, M. C.; Blanksby, S. J. Isomeric lipid signatures reveal compartmentalized fatty acid metabolism in cancer. *J. Lipid Res.* **2022**, *63* (6), 100223. DOI: 10.1016/j.jlr.2022.100223. Published Online: May. 7, 2022.

First Publication of the Project

Reactive Matrix-Assisted Laser Desorption/Ionization Mass Spectrometry Imaging Using an Intrinsically Photoreactive Paternò-Büchi Matrix for Double-Bond Localization in Isomeric Phospholipids

Fabian Wäldchen, Bernhard Spengler, and Sven Heiles

Journal of the American Chemical Society, **2019**, 141, 11816-11820

DOI: 10.1021/jacs.9b05868

JACS
JOURNAL OF THE AMERICAN CHEMICAL SOCIETY
Cite This: J. Am. Chem. Soc. 2019, 141, 11816−11820
Communication
pubs.acs.org/JACS

Reactive Matrix-Assisted Laser Desorption/Ionization Mass Spectrometry Imaging Using an Intrinsically Photoreactive Paternò−Büchi Matrix for Double-Bond Localization in Isomeric Phospholipids

Fabian Wäldchen, Bernhard Spengler, and Sven Heiles*

Institute of Inorganic and Analytical Chemistry, Analytical Chemistry, Justus Liebig University Giessen, Heinrich Buff Ring 17, 35392 Giessen, Germany

Supporting Information

ABSTRACT: The location and identity of phospholipids (PLs) within tissues can serve as diagnostic markers for tissue types or diseases. Whereas mass spectrometry imaging (MSI) has emerged as a powerful bioanalytical tool to visualize PL distributions, inferring PL identities from MSI experiments is challenging. Especially, C=C double-bond (DB) positions are not identifiable in most MSI experiments. Herein, we introduce benzophenone (BPh) as a novel reactive matrix for matrix-assisted laser desorption/ionization (MALDI). BPh promotes desorption/ionization and simultaneously serves as derivatization reagent that allows functionalization of unsaturated PLs during the MALDI process via a laser-light driven Paternò−Büchi (PB) reaction without the need for additional equipment. Using BPh, PB product ions of numerous PL classes are readily generated to pinpoint the location of DBs. High lateral resolution MSI results of DB-position isomers are presented, highlighting the capabilities of BPh as a PB-reactive MALDI matrix to potentially unveil the impact of DB-position isomers in PL metabolism.

Lipids fulfill significant roles in energy storage,[1] cell signaling[2] and are the building blocks of cell membranes.[3] As details of lipid functions are closely connected to their molecular makeup, structural lipid analysis helps to decipher specifics of metabolic transformations[4] and to reveal disease biomarkers.[5]

Mass spectrometry (MS), tandem MS (MS^n) and ion mobility MS have emerged as important bioanalytical tools to study lipid structures.[6] For example, direct infusion, or "shotgun" MS[7] has recently been used to show that energy homeostasis in mitochondria is modulated by cardiolipins.[8] Automated structure assignment of lipids was successfully implemented for shotgun and liquid chromatography MS to facilitate high throughput structure-resolved lipidomics.[9]

Despite the impressive capabilities of MS-based lipidomics, not all structural features of lipids are readily deciphered via collision-induced dissociation (CID). In particular, assignment of stereospecific numbering (*sn*) and DB-positions necessitate comparison to authentic standards in most MS^2 methods. Therefore, novel MS^n and functionalization strategies have been developed. Ultraviolet photodissociation, ozonolysis and UV light induced PB functionalization were shown to allow DB-positions and/or *sn*-isomers assignment.[10,11]

However, local variations of lipid abundances and structures are only accessible when using MSI. Sophisticated MSI instruments have been developed to discriminate DB-position and *sn*-isomers of PLs.[12−14] All these studies revealed an unexpectedly high level of PL isomer organization in specific histological regions that heralds the importance of underlying metabolic processes.

We herein present BPh as a PB reactive MALDI matrix, in order to allow researchers to study PL DB-position isomers and their changes in tissue with access to MALDI-MSI equipment. Upon UV laser (343 nm) irradiation during the normal laser desorption/ionization process, BPh reacts with unsaturated PLs in a [2+2] PB reaction enabling assignment of DB-positions in MS^2 and MS^2I experiments.

To simplify PB functionalization of PLs for MALDI-MSI applications, compounds that can simultaneously serve as crystalline MALDI matrix and PB functionalization reagent were screened. Our investigations commenced with BPh because it readily crystallizes, absorbs typical MALDI laser wavelengths[15] (Figure S1) and was shown to efficiently react with olefins in in-solution PB reactions.[16] PB-functionalized PLs are 182.07 Da higher in mass per functionalized DB than their unfunctionalized counterparts (Scheme 1). CID of PB

Scheme 1. PB Reaction Scheme of a Hypothetical PL with BPh and Subsequent CID Fragmentation[a]

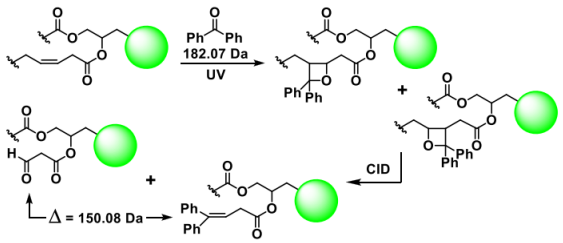

[a]Head group as well as charge state are abbreviated by a green circle.

Received: June 1, 2019
Published: July 18, 2019

DOI: 10.1021/jacs.9b05868
J. Am. Chem. Soc. 2019, 141, 11816−11820

product ions results in formation of two fragment ions for every DB-position in a retro-PB reaction. The fragment ions corresponding to the same DB-position are separated by 150.08 Da.

The optimized application protocol was used to cover mouse brain sections by pneumatic matrix deposition (Supporting Protocol 1, Figure S2A). During BPh application the sample surface was, in first experiments, irradiated by a mercury-UV lamp (Figure S2B). The resulting MALDI mass spectrum is shown in Figure 1A. The mass spectrum between

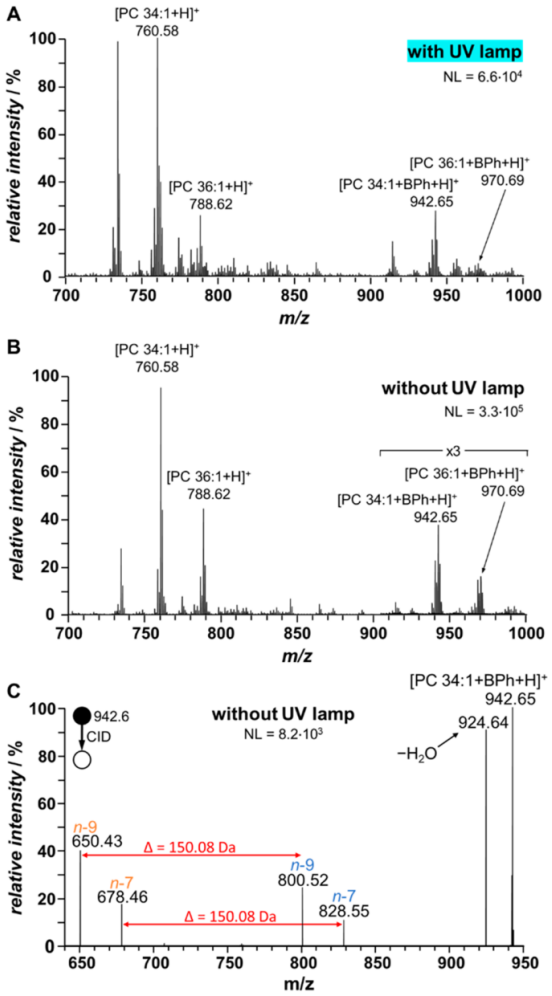

Figure 1. (A) MALDI-MS recorded from BPh-covered mouse brain section with UV lamp irradiation. (B) MALDI-MS recorded from BPh-covered mouse brain section without UV lamp irradiation. (C) MALDI-MS^2 spectrum of $[PC\ 34{:}1{+}BPh{+}H]^+$. NL = normalized level.

m/z 700−900 contains signals assigned to protonated PLs. Two selected protonated PCs, namely PC 34:1 and PC 36:1, are highlighted. A complete list of detected PLs with BPh as matrix are listed and compared to results with the standard matrix 2,5-dihydroxybenzoic acid (DHB) in Table S1 and Figure S3. Assignment of ions detected between m/z 900−1000 to endogenous PLs was not possible. However, the mass differences between ions from this higher m/z range and assigned endogenous PLs are in line with addition of BPh to PLs and these ions are absent in MALDI mass spectra when using DHB as matrix (Figure S4). For example, for protonated PC 34:1 and PC 36:1, associated signals 182.07 Da higher in mass are detected with an apparent reaction yield, Y, of 21% and 17%, respectively (Figure 1A).

To investigate if ions between m/z 900−1000 form as a result of UV lamp irradiation, BPh was applied under light exclusion onto mouse brain sections. The resulting MALDI mass spectrum is shown in Figure 1B. The spectra in Figure 1A and Figure 1B are unexpectedly similar. The major difference between the spectra being the absolute MS signal intensity. Without UV lamp irradiation the signals for $[PC\ 34{:}1{+}H]^+$ and $[PC\ 34{:}1{+}BPh{+}H]^+$ were 5.0 and 2.5 times higher than the same signals with UV irradiation during matrix application, respectively. The PB reaction yields for PC 34:1 and PC 36:1 were 12% and 11% (Figure 1B). This suggests that the majority of product ions are not due to UV lamp irradiation. However, CID of BPh-attached PL ions with and without the use of mercury-UV light yielded identical fragment ions. Typical CID mass spectra are shown in Figure 1C and Figure S5. $[PC\ 34{:}1{+}BPh{+}H]^+$ fragment ions assigned to retro-PB reactions of DBs located at n-7 and n-9 are consistent with recently published results (Figure 1C).[13,14] The fact that the majority of BPh-attached PLs do not originate from UV lamp irradiation while tandem MS results indicate the presence of PB product ions, supports the idea that PB product ions are formed as a result of MALDI laser irradiation of the BPh-covered sample surface. Comparable results for relative ion intensities, matrix crystals sizes and Y values were obtained when sublimating BPh onto mouse brain tissue (Figure S6). MALDI mass spectra of BPh-covered mouse brain resulted in a total of 19 signals that were assigned to PB-functionalized unsaturated PLs (Table S2).

In order to corroborate that MALDI laser light initiates the PB reaction, extracts of BPh-coated mouse brain sections were analyzed via liquid chromatography (LC)-MS^2. The PB product yields were only about 0.03% (Figure S7). This demonstrates that the large majority of PB products are formed upon UV laser irradiation. A second piece of evidence comes from MALDI MS measurements with varying laser pulse energy. If the PB reaction is initiated by MALDI laser light, increasing laser fluence is expected to result in increased PB yields. As evident from Figure S8, Y for $[PC\ 34{:}1{+}BPh{+}H]^+$ increases from 9.0 ± 2.3% for 0.13 μJ/pulse to 19.2 ± 2.5% for 1.44 μJ/pulse. Our findings are supported by results reported by Yuan et al., which showed that the $^3(n\pi^*)$ phosphorescence quantum yield of BPh, the state involved in PB reactivity, at room temperature is increased from 0.001% in solution to 15.9% in BPh crystals.[15] This combined evidence strongly suggests that MALDI laser light initiates PB reactions between BPh and PLs.

To evaluate the analytical capabilities of BPh as a MALDI matrix for pinpointing PL DB-positions, different PL classes with varying degrees of unsaturation were investigated, and results are shown in Figures S9 and S10. In accordance with previous reports for other PB reagents, DBs were successfully localized in PC, PE, PI, PA, PG and SM lipids. DBs were successfully determined for 10 PCs directly from mouse cerebellum (Table S3). The relative ion intensity of PB product ions from mouse brain tissue increases with increasing DB number in line with in-solution experiments (Table S4).[11]

DOI: 10.1021/jacs.9b05868
J. Am. Chem. Soc. 2019, 141, 11816−11820

Intensities for PB product ions of other lipid classes from mouse brain tissue were too low for DB-localization, most likely due to the known ion suppression effect exerted by PCs and SMs.[17] In addition to qualitative PL DB-position analysis, relative quantification of DB-position isomers was successfully performed (Figure S11).

Following BPh performance evaluation as MALDI matrix (Figures S12–S14), the BPh matrix was employed for DB-position resolved MALDI-MS^{2}I experiments. Results for PC 34:1 and PC 36:1 in mouse cerebellum sections are shown in Figures 2, S15 and S16. As previously demonstrated, PC 34:1

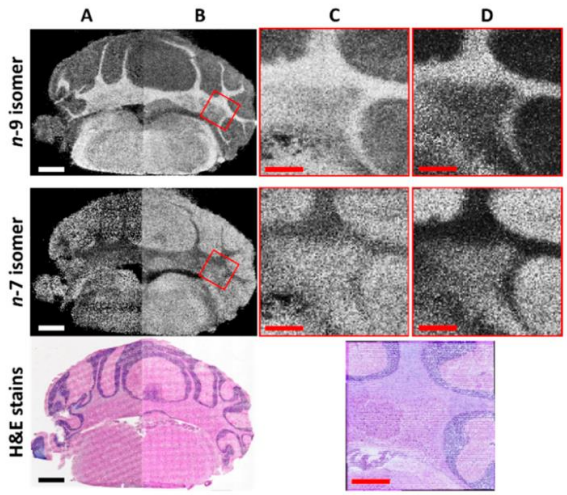

Figure 2. MALDI-MS^2 images of diagnostic retro-PB aldehyde fragment ions of (A) PC 36:1 and (B–D) PC 34:1 acquired from mouse cerebellum sections with (A,B) 25 μm and (C,D) 15 μm pixel size. TIC normalized (A–C) *n*-9, (A–C) *n*-7 and relative intensity (D) *n*-9/*n*-7 and (D) *n*-7/*n*-9 MS images. The red square in column B highlights the region measured in column C+D. (lower row) Microscope images of H&E stained tissue sections after MALDI-MS^{2}I. Scale bars are (A,B) 1 mm and (C,D) 400 μm. TIC – total ion current.

and PC 36:1 mainly consist of PC 16:0_18:1(*n*-9)/PC 16:0_18:1(*n*-7) and PC 16:0_20:1(*n*-9)/PC 16:0_20:1(*n*-7)/PC 18:0_18:1(*n*-9)/PC 18:0_18:1(*n*-7), respectively.[13,14] Consistently, we solely detected *n*-9 and *n*-7 associated fragment ions and the distribution of these DB-position isomers within mouse cerebellum tissue differed (Figure 2). The TIC normalized lateral distributions of *n*-9 for PC 36:1 (Figure 2A) and PC 34:1 (Figure 2B) with 25 μm pixel resolution reveal increased abundance of *n*-9 in the white matter of the cerebellum compared to surrounding tissue. In contrast to the *n*-9 distributions, the distributions of *n*-7 of PC 36:1 and PC 34:1 (Figure 2, A+B) exhibit depleted *n*-7 isomer abundance in white brain matter compared to gray brain matter. Our results are in line with previous reports.[13,14] Comparison between 25 μm MS^{2}I results and H&E stained microscopy images acquired after MS^{2}I experiments (Figure 2) confirm that regions with increased *n*-9 and *n*-7 abundance correlate with white and gray brain matter, respectively. DB-position isomer resolved MS^{2}I results of PC 34:1 in mouse cerebellum with 15 μm pixel resolution are shown in Figure 2C. In accordance with 25 μm MS^{2}I results and histological regions identified via microscopy, DB-position isomer abundances differ between tissue regions. The abundance of *n*-9 is higher in white compared to gray matter, whereas *n*-7 shows a complementary intensity distribution. Visualization of this organizational preference of DB-position isomers is pronounced by plotting the intensity ratios *n*-9/*n*-7 and *n*-7/*n*-9 (Figure 2D). Taking into account that the average diameter of neuronal cells in mouse brain is between 10–20 μm,[18] the separation between histological regions based on DB-position isomer abundances down to 15 μm suggests that specific PL isomer abundances are preserved down to the single cell level.

Next, we studied DB-resolved PL surface distributions of male *Schistosoma mansoni* to demonstrate the applicability of our workflow to study unknown samples. *S. mansoni* is a mammalian trematode causing the human disease schistosomiasis (bilharzia).[19,20] The parasite is known for its unique PL metabolism, but specifics of DB-position isomerism are largely unknown. DB-position resolved MALDI-MS^{2}I experiments for PC 34:1 and PC 36:1 from *S. mansoni* surfaces are shown in Figures 3, S17, S18 and S19, respectively. PC 34:1 in male *S.*

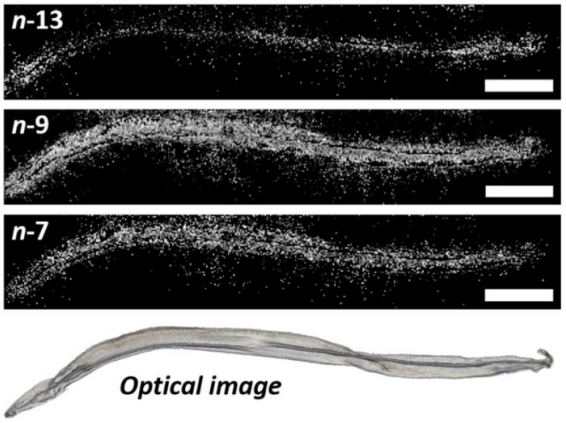

Figure 3. MALDI-MS^2 images of diagnostic retro-PB aldehyde fragment ions of PC 34:1 acquired from male *S. mansoni* tegument with 20 μm pixel size (TIC normalized). (lower row) Optical microscopy image before measurement. The scale bars reflect 1 mm.

mansoni tegument, i.e., the worm surface, does not only consist of *n*-7 and *n*-9 DB-positions but also contains the *n*-13 DB-position (Figure 3) in line with previous studies.[19] Shotgun PB-MS^2 of male *S. mansoni* extracts revealed that PC 34:1 mainly consists of the isomers PC 16:0_18:1(*n*-7), PC 16:0_18:1(*n*-9) and PC 16:0_18:1(*n*-13) (Figures S20 and S21). However, the three DB-position isomers are not uniformly distributed across the parasite surface. While *n*-7 and *n*-9 isomers are located across the entire *S. mansoni* surface, *n*-13 associated fragment ions show increased abundance in head and tail in comparison to the intermediate region of the parasitic organism's tegument (Figures 3 and S17). This might indicate an accumulation or specific function of PC 16:0_18:1(*n*-13) in these regions. Male *S. mansoni* PC 36:1 was found to be composed of FA 16:0, FA 18:0, FA 18:1 and FA 20:1 (Figure S20). The most abundant DB-position fragment ion corresponds to a DB at position *n*-9, but low intensity signals for *n*-7 and *n*-13 were also present (Figure S21). Even though no pronounced accumulations of DB-position isomers in tegumental structures were observed

DOI: 10.1021/jacs.9b05868
J. Am. Chem. Soc. 2019, 141, 11816–11820

(Figure S18), our MALDI-MS^{2}I method using BPh as matrix permitted the identification of the unusual FA 18:1(*n*-13)/FA 20:1(*n*-13) in PC 36:1 from male *S. mansoni* tegument.

In conclusion, we have demonstrated that pneumatically sprayed and sublimated BPh crystal layers can undergo a PB reaction with unsaturated PLs initiated by 343 nm laser light during laser desorption/ionization. To the best of our knowledge, this is the first report of a structure-diagnostic photochemical reaction during MALDI. We have exploited the resulting PB reaction products to perform MALDI-MS^{2}I experiments with the highest reported pixel resolution of 15 μm, enabling the discrimination of DB-position PL isomer lateral distributions using commercially available MSI equipment. As only BPh and laser light of 330−370 nm is required to perform DB-position resolved MALDI-MS^{2}I experiments, our methodology can be used by all researchers in life science or medicine with access to modern commercial MALDI-MSI equipment. In order to improve the PB reaction yield, our future research efforts will focus on testing other PB reactive solid matrix compounds with various MALDI laser wavelengths and mixtures of PB reactive with conventional matrices.[21]

■ ASSOCIATED CONTENT

Supporting Information

The Supporting Information is available free of charge on the ACS Publications website at DOI: 10.1021/jacs.9b05868.

Detailed description of experimental methods, nomenclature and protocols; MSI results using BPh as MALDI matrix; assigned PLs in MALDI-MSI in experiments with the BPh matrix; MALDI-MS^2 for authentic PL standards; relative quantification by MALDI-MS^2 of PL DB-position isomers; microscopic image of BPh crystal layer; assigned PB reaction products from mouse brain; confirmed DB-positions from mouse brain sections of PLs using MALDI-MS^{2}I; additional DB-position resolved MALDI-MS^{2}I results for mouse brain sections and male *S. mansoni* (PDF)

■ AUTHOR INFORMATION

Corresponding Author

*Sven.Heiles@anorg.chemie.uni-giessen.de

ORCID

Bernhard Spengler: 0000-0003-0179-5653

Sven Heiles: 0000-0003-3779-8071

Notes

The authors declare the following competing financial interest(s): Bernhard Spengler is a consultant of TransMIT GmbH, Giessen, Germany. The other authors declare no competing financial interests.

■ ACKNOWLEDGMENTS

S.H. thanks the Fonds der chemischen Industrie for financial support through a Liebig fellowship. The authors thank D. Lüke for collecting shotgun and LC-MS^2 data of *S. mansoni* as well as mouse brain extracts and H. F. König for some authentic standard measurements. Financial support by the Bundesministerium für Bildung und Forschung, BMBF (project 0313442) and by the Deutsche Forschungsgemeinschaft (Sp 314/12-1, Sp 314/13-1, INST 162/500-1 FUGG and HE 8521/1-1) is gratefully acknowledged. All authors thank Prof. Dr. W. Kummer (Institute of Anatomy and Cell Biology, Justus Liebig University Giessen, Germany) as well as Prof. Dr. C. G. Grevelding (Institute for Parasitology, Justus Liebig University Giessen, Germany) and their groups for providing mouse brain as well as *S. mansoni* samples.

■ REFERENCES

(1) Walther, T. C.; Farese, R. V. Lipid droplets and cellular lipid metabolism. *Annu. Rev. Biochem.* **2012**, *81*, 687−714.

(2) Corda, D.; De Matteis, M. A. Lipid signalling in health and disease. *FEBS J.* **2013**, *280*, 6280.

(3) (a) van Meer, G.; Voelker, D. R.; Feigenson, G. W. Membrane lipids: Where they are and how they behave. *Nat. Rev. Mol. Cell Biol.* **2008**, *9*, 112−124. (b) Brügger, B. Inconspicuous Little Allies: How Membrane Lipids Help Modulate Protein Function. *ACS Cent. Sci.* **2018**, *4*, 530−531.

(4) Vriens, K.; Christen, S.; Parik, S.; Broekaert, D.; Yoshinaga, K.; Talebi, A.; Dehairs, J.; Escalona-Noguero, C.; Schmieder, R.; Cornfield, T.; Charlton, C.; Romero-Pérez, L.; Rossi, M.; Rinaldi, G.; Orth, M. F.; Boon, R.; Kerstens, A.; Kwan, S. Y.; Faubert, B.; Méndez-Lucas, A.; Kopitz, C. C.; Chen, T.; Fernandez-Garcia, J.; Duarte, J. A. G.; Schmitz, A. A.; Steigemann, P.; Najimi, M.; Hägebarth, A.; van Ginderachter, J. A.; Sokal, E.; Gotoh, N.; Wong, K.-K.; Verfaillie, C.; Derua, R.; Munck, S.; Yuneva, M.; Beretta, L.; DeBerardinis, R. J.; Swinnen, J. V.; Hodson, L.; Cassiman, D.; Verslype, C.; Christian, S.; Grünewald, S.; Grünewald, T. G. P.; Fendt, S.-M. Evidence for an alternative fatty acid desaturation pathway increasing cancer plasticity. *Nature* **2019**, *566*, 403−406.

(5) (a) Ståhlman, M.; Pham, H. T.; Adiels, M.; Mitchell, T. W.; Blanksby, S. J.; Fagerberg, B.; Ekroos, K.; Borén, J. Clinical dyslipidaemia is associated with changes in the lipid composition and inflammatory properties of apolipoprotein-B-containing lipoproteins from women with type 2 diabetes. *Diabetologia* **2012**, *55*, 1156−1166. (b) Hirsch, H. A.; Iliopoulos, D.; Joshi, A.; Zhang, Y.; Jaeger, S. A.; Bulyk, M.; Tsichlis, P. N.; Shirley Liu, X.; Struhl, K. A transcriptional signature and common gene networks link cancer with lipid metabolism and diverse human diseases. *Cancer Cell* **2010**, *17*, 348−361. (c) Santos, C. R.; Schulze, A. Lipid metabolism in cancer. *FEBS J.* **2012**, *279*, 2610−2623.

(6) (a) Han, X. *Lipidomics: Comprehensive mass spectrometry of lipids*; John Wiley & Sons Inc: Hoboken, NJ, 2016. (b) Murphy, R. C. *Tandem Mass Spectrometry of Lipids*; Royal Society of Chemistry: Cambridge, 2014. (c) Groessl, M.; Graf, S.; Knochenmuss, R. High resolution ion mobility-mass spectrometry for separation and identification of isomeric lipids. *Analyst* **2015**, *140*, 6904−6911. (d) Maccarone, A. T.; Duldig, J.; Mitchell, T. W.; Blanksby, S. J.; Duchoslav, E.; Campbell, J. L. Characterization of acyl chain position in unsaturated phosphatidylcholines using differential mobility-mass spectrometry. *J. Lipid Res.* **2014**, *55*, 1668−1677. (e) Bowman, A. P.; Abzalimov, R. R.; Shvartsburg, A. A. Broad Separation of Isomeric Lipids by High-Resolution Differential Ion Mobility Spectrometry with Tandem Mass Spectrometry. *J. Am. Soc. Mass Spectrom.* **2017**, *28*, 1552−1561.

(7) (a) Brügger, B.; Erben, G.; Sandhoff, R.; Wieland, F. T.; Lehmann, W. D. Quantitative analysis of biological membrane lipids at the low picomole level by nano-electrospray ionization tandem mass spectrometry. *Proc. Natl. Acad. Sci. U. S. A.* **1997**, *94*, 2339−2344. (b) Eggers, L. F.; Müller, J.; Marella, C.; Scholz, V.; Watz, H.; Kugler, C.; Rabe, K. F.; Goldmann, T.; Schwudke, D. Lipidomes of lung cancer and tumour-free lung tissues reveal distinct molecular signatures for cancer differentiation, age, inflammation, and pulmonary emphysema. *Sci. Rep.* **2017**, *7*, 11087.

(8) Sustarsic, E. G.; Ma, T.; Lynes, M. D.; Larsen, M.; Karavaeva, I.; Havelund, J. F.; Nielsen, C. H.; Jedrychowski, M. P.; Moreno-Torres, M.; Lundh, M.; Plucinska, K.; Jespersen, N. Z.; Grevengoed, T. J.; Kramar, B.; Peics, J.; Hansen, J. B.; Shamsi, F.; Forss, I.; Neess, D.; Keipert, S.; Wang, J.; Stohlmann, K.; Brandslund, I.; Christensen, C.; Jørgensen, M. E.; Linneberg, A.; Pedersen, O.; Kiebish, M. A.;

Qvortrup, K.; Han, X.; Pedersen, B. K.; Jastroch, M.; Mandrup, S.; Kjær, A.; Gygi, S. P.; Hansen, T.; Gillum, M. P.; Grarup, N.; Emanuelli, B.; Nielsen, S.; Scheele, C.; Tseng, Y.-H.; Færgeman, N. J.; Gerhart-Hines, Z. Cardiolipin Synthesis in Brown and Beige Fat Mitochondria Is Essential for Systemic Energy Homeostasis. *Cell Metab.* **2018**, *28*, 159−174.e11.

(9) (a) Bird, S. S.; Marur, V. R.; Sniatynski, M. J.; Greenberg, H. K.; Kristal, B. S. Lipidomics profiling by high-resolution LC-MS and high-energy collisional dissociation fragmentation: Focus on characterization of mitochondrial cardiolipins and monolysocardiolipins. *Anal. Chem.* **2011**, *83*, 940−949. (b) Hartler, J.; Triebl, A.; Ziegl, A.; Trötzmüller, M.; Rechberger, G. N.; Zeleznik, O. A.; Zierler, K. A.; Torta, F.; Cazenave-Gassiot, A.; Wenk, M. R.; Fauland, A.; Wheelock, C. E.; Armando, A. M.; Quehenberger, O.; Zhang, Q.; Wakelam, M. J. O.; Haemmerle, G.; Spener, F.; Köfeler, H. C.; Thallinger, G. G. Deciphering lipid structures based on platform-independent decision rules. *Nat. Methods* **2017**, *14*, 1171−1174. (c) Guijas, C.; Montenegro-Burke, J. R.; Domingo-Almenara, X.; Palermo, A.; Warth, B.; Hermann, G.; Koellensperger, G.; Huan, T.; Uritboonthai, W.; Aisporna, A. E.; Wolan, D. W.; Spilker, M. E.; Benton, H. P.; Siuzdak, G. METLIN: A Technology Platform for Identifying Knowns and Unknowns. *Anal. Chem.* **2018**, *90*, 3156−3164.

(10) (a) Williams, P. E.; Klein, D. R.; Greer, S. M.; Brodbelt, J. S. Pinpointing Double Bond and sn-Positions in Glycerophospholipids via Hybrid 193 nm Ultraviolet Photodissociation (UVPD) Mass Spectrometry. *J. Am. Chem. Soc.* **2017**, *139*, 15681−15690. (b) Becher, S.; Esch, P.; Heiles, S. Relative Quantification of Phosphatidylcholine sn-Isomers Using Positive Doubly Charged Lipid-Metal Ion Complexes. *Anal. Chem.* **2018**, *90*, 11486−11494. (c) Ryan, E.; Nguyen, C. Q. N.; Shiea, C.; Reid, G. E. Detailed Structural Characterization of Sphingolipids via 193 nm Ultraviolet Photodissociation and Ultra High Resolution Tandem Mass Spectrometry. *J. Am. Soc. Mass Spectrom.* **2017**, *28*, 1406−1419. (d) Pham, H. T.; Maccarone, A. T.; Thomas, M. C.; Campbell, J. L.; Mitchell, T. W.; Blanksby, S. J. Structural characterization of glycerophospholipids by combinations of ozone- and collision-induced dissociation mass spectrometry: The next step towards "top-down" lipidomics. *Analyst* **2014**, *139*, 204−214. (e) Poad, B. L. J.; Zheng, X.; Mitchell, T. W.; Smith, R. D.; Baker, E. S.; Blanksby, S. J. Online Ozonolysis Combined with Ion Mobility-Mass Spectrometry Provides a New Platform for Lipid Isomer Analyses. *Anal. Chem.* **2018**, *90*, 1292−1300. (f) Murphy, R. C.; Okuno, T.; Johnson, C. A.; Barkley, R. M. Determination of Double Bond Positions in Polyunsaturated Fatty Acids Using the Photochemical Paternò-Büchi Reaction with Acetone and Tandem Mass Spectrometry. *Anal. Chem.* **2017**, *89*, 8545−8553. (g) Ma, X.; Xia, Y. Pinpointing double bonds in lipids by Paternò-Büchi reactions and mass spectrometry. *Angew. Chem., Int. Ed.* **2014**, *53*, 2592−2596. (h) Wäldchen, F.; Becher, S.; Esch, P.; Kompauer, M.; Heiles, S. Selective phosphatidylcholine double bond fragmentation and localisation using Paternò-Büchi reactions and ultraviolet photodissociation. *Analyst* **2017**, *142*, 4744−4755. (i) Korf, A.; Jeck, V.; Schmid, R.; Helmer, P. O.; Hayen, H. Lipid Species Annotation at Double Bond Position Level with Custom Databases by Extension of the MZmine 2 Open-Source Software Package. *Anal. Chem.* **2019**, *91*, 5098−5105.

(11) Esch, P.; Heiles, S. Charging and Charge Switching of Unsaturated Lipids and Apolar Compounds Using Paternò-Büchi Reactions. *J. Am. Soc. Mass Spectrom.* **2018**, *29*, 1971−1980.

(12) (a) Klein, D. R.; Feider, C. L.; Garza, K. Y.; Lin, J. Q.; Eberlin, L. S.; Brodbelt, J. S. Desorption Electrospray Ionization Coupled with Ultraviolet Photodissociation for Characterization of Phospholipid Isomers in Tissue Sections. *Anal. Chem.* **2018**, *90*, 10100−10104. (b) Porta Siegel, T.; Ekroos, K.; Ellis, S. R. Reshaping Lipid Biochemistry by Pushing Barriers in Structural Lipidomics. *Angew. Chem., Int. Ed.* **2019**, *58*, 6492−6501.

(13) Bednařík, A.; Bölsker, S.; Soltwisch, J.; Dreisewerd, K. An On-Tissue Paternò-Büchi Reaction for Localization of Carbon-Carbon Double Bonds in Phospholipids and Glycolipids by Matrix-Assisted Laser-Desorption-Ionization Mass-Spectrometry Imaging. *Angew. Chem., Int. Ed.* **2018**, *57*, 12092−12096.

(14) Paine, M. R. L.; Poad, B. L. J.; Eijkel, G. B.; Marshall, D. L.; Blanksby, S. J.; Heeren, R. M. A.; Ellis, S. R. Mass Spectrometry Imaging with Isomeric Resolution Enabled by Ozone-Induced Dissociation. *Angew. Chem., Int. Ed.* **2018**, *57*, 10530−10534.

(15) Yuan, W. Z.; Shen, X. Y.; Zhao, H.; Lam, J. W. Y.; Tang, L.; Lu, P.; Wang, C.; Liu, Y.; Wang, Z.; Zheng, Q.; Sun, J. Z.; Ma, Y.; Tang, B. Z. Crystallization-Induced Phosphorescence of Pure Organic Luminogens at Room Temperature. *J. Phys. Chem. C* **2010**, *114*, 6090−6099.

(16) Xu, T.; Pi, Z.; Song, F.; Liu, S.; Liu, Z. Benzophenone used as the photochemical reagent for pinpointing C = C locations in unsaturated lipids through shotgun and liquid chromatography-mass spectrometry approaches. *Anal. Chim. Acta* **2018**, *1028*, 32−44.

(17) (a) Wang, J.; Wang, C.; Han, X. Enhanced coverage of lipid analysis and imaging by matrix-assisted laser desorption/ionization mass spectrometry via a strategy with an optimized mixture of matrices. *Anal. Chim. Acta* **2018**, *1000*, 155−162. (b) Taylor, A. J.; Dexter, A.; Bunch, J. Exploring Ion Suppression in Mass Spectrometry Imaging of a Heterogeneous Tissue. *Anal. Chem.* **2018**, *90*, 5637−5645.

(18) (a) van Diepen, M. T.; Parsons, M.; Downes, C. P.; Leslie, N. R.; Hindges, R.; Eickholt, B. J. MyosinV controls PTEN function and neuronal cell size. *Nat. Cell Biol.* **2009**, *11*, 1191−1196. (b) Lawson, S. N. The postnatal development of large light and small dark neurons in mouse dorsal root ganglia: A statistical analysis of cell numbers and size. *J. Neurocytol.* **1979**, *8*, 275−294.

(19) Brouwers, J. F.; Versluis, C.; van Golde, L. M.; Tielens, A. G. 5-Octadecenoic acid: Evidence for a novel type of fatty acid modification in schistosomes. *Biochem. J.* **1998**, *334* (Pt 2), 315−319.

(20) (a) van der Kleij, D.; Latz, E.; Brouwers, J. F. H. M.; Kruize, Y. C. M.; Schmitz, M.; Kurt-Jones, E. A.; Espevik, T.; de Jong, E. C.; Kapsenberg, M. L.; Golenbock, D. T.; Tielens, A. G. M.; Yazdanbakhsh, M. A novel host-parasite lipid cross-talk. Schistosomal lyso-phosphatidylserine activates toll-like receptor 2 and affects immune polarization. *J. Biol. Chem.* **2002**, *277*, 48122−48129. (b) Colley, D. G.; Bustinduy, A. L.; Secor, W. E.; King, C. H. Human schistosomiasis. *Lancet* **2014**, *383*, 2253−2264.

(21) Leopold, J.; Popkova, Y.; Engel, K. M.; Schiller, J. Recent Developments of Useful MALDI Matrices for the Mass Spectrometric Characterization of Lipids. *Biomolecules* **2018**, *8*, 173.

DOI: 10.1021/jacs.9b05868
J. Am. Chem. Soc. 2019, 141, 11816−11820

Second Publication of the Project

Multifunctional Reactive MALDI Matrix Enabling High-Lateral Resolution Dual Polarity MS Imaging and Lipid C=C Position-Resolved MS^2 Imaging

Fabian Wäldchen, Franziska Mohr, Andreas H. Wagner, and Sven Heiles

Analytical Chemistry, **2020**, 92, 14130-14138

DOI: 10.1021/acs.analchem.0c03150

analytical chemistry

pubs.acs.org/ac Article

Multifunctional Reactive MALDI Matrix Enabling High-Lateral Resolution Dual Polarity MS Imaging and Lipid C=C Position-Resolved MS^2 Imaging

Fabian Wäldchen, Franziska Mohr, Andreas H. Wagner, and Sven Heiles*

Cite This: *Anal. Chem.* 2020, 92, 14130−14138 Read Online

ACCESS | Metrics & More | Article Recommendations | Supporting Information

ABSTRACT: Local lipid variations in tissues are readily revealed with mass spectrometry imaging (MSI) methods, and the resulting lipid distributions serve as bioanalytical signatures to reveal cell- or tissue-specific lipids. Comprehensive MSI lipid mapping requires measurements in both ion polarities. Additionally, structural lipid characterization is necessary to link the lipid structure to lipid function. Whereas some structural elements of lipids are readily derived from high-resolution mass spectrometry (MS) and tandem-MS (MS^n), the localization of C=C double bonds (DBs) requires specialized fragmentation and/or functionalization methods. In this work, we identify a multifunctional matrix-assisted laser desorption/ionization (MALDI) matrix for spatially resolved lipidomics investigations that reacts with lipids in Paternò−Büchi (PB) reactions during laser irradiation facilitating DB-position assignment and allows dual-polarity high-resolution MALDI-MSI and MALDI MS^2I studies. By screening 12 compounds for improved ionization efficiency in positive-/negative-ion mode and the functionalization yield compared to the previously introduced reactive MALDI matrix benzophenone, 2-benzoylpyridine (BzPy) is identified as the best candidate. The new matrix enables DB localization of authentic standards belonging to 12 lipid classes and helps to assign 133/58 lipid features in positive-/negative-ion mode from mouse cerebellum tissue. The analytical capabilities of BzPy as a multifunctional MALDI-MSI matrix are demonstrated by imaging endogenous and PB-functionalized lipids in mouse kidney sections with 7 μm lateral resolution in both ion modes. Tracking diagnostic lipid DB-position fragment ions in mouse pancreatic tissue with down to 10 μm pixel size allows us to identify the islets of Langerhans associated with lipid isomer upregulation and depletion.

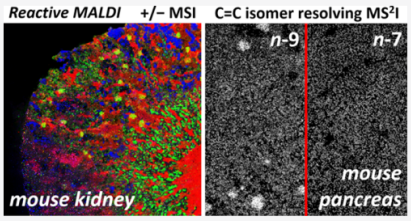

INTRODUCTION

In-depth lipid characterization of cells, tissues, or body fluids is at the heart of lipidomics that promises novel insights into lipid biology and aims to use lipid biomarkers or lipid signatures as diagnostic probes to monitor disease progression.[1,2] Lipid analysis requires not only comprehensive charting of expressed lipids but also a detailed characterization of lipid distribution and structures.[3] This is because disease-associated lipid abundance alterations or implications of subtle structural changes are often unpredictable as most of the intertwined enzymatic processes involved in lipid metabolism are yet to be unraveled.[4−6] For example, the unfolded protein response (UPR) of eukaryotic cells increases when the level of saturated lipids in the cell membrane of the endoplasmic reticulum increases. This suggests that the UPR regulatory machinery can sense cell membrane composition offering a potential connecting to reports about endoplasmic reticulum stress induced by obesity, high-fat diets, or type 2 diabetes.[7,8] The mechanism of lipid composition sensing, however, remains unclear. This demonstrates that many details of lipid metabolism in the context of biology and medicine will benefit from bioanalytical methods that can provide a comprehensive picture of lipid composition and distribution and also can investigate lipid structure variations to reveal unexpected effects in lipid biology.

One of the most widely used untargeted bioanalytical tools in lipidomics is mass spectrometry (MS).[2] This is because direct infusion measurements, often using electrospray ionization (ESI),[9] desorption ESI (DESI),[10] and matrix-assisted laser desorption/ionization (MALDI),[11] allow us to distinguish a multitude of lipids by accurate mass-to-charge (m/z) values and assign their sum formulae when employing state-of-the-art mass spectrometers. Tandem MS (MS^n), first and foremost collision-induced dissociation (CID), reveals lipid fatty acid composition and lipid classes.[12] Hyphenated techniques such as liquid chromatography (LC) or ion-mobility spectrometry can further improve the performance of MS-based lipidomics by separating isobaric and isomeric lipid compounds.[13] However, the assignment of mass spectrometric features to specific lipid structures, especially for glycerolipids,

Received: July 24, 2020
Accepted: September 12, 2020
Published: September 12, 2020

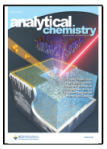

https://dx.doi.org/10.1021/acs.analchem.0c03150
Anal. Chem. 2020, 92, 14130−14138

glycerophospholipids, sphingolipids, and glycolipids, remains challenging. Therefore, recent years have seen a surge in novel MS^n methods that allow us to distinguish structural features of isomeric lipids. Especially for C=C (DB) position assignment, many novel mass spectrometric tools, for example, ultraviolet (UV) photodissociation mass spectrometry,[14−17] radical-directed dissociation,[18,19] ozone-induced dissociation (OzID),[20] and infrared (IR) action spectroscopy of ultracold ions,[21] have been reported. In-solution functionalization via epoxidation[22,23] or photochemical Paternò−Büchi (PB) functionalization prior ESI is also capable of identifing lipid DB positions.[24−28] The latter functionalization scheme, pioneered by Ma and Xia,[29] has been used by numerous groups to assign DB positions in direct infusion and LC−MS workflows.[30,31] Lipid DB isomer assignment from surfaces or local alterations of lipid isomer abundances in tissues, however, require desorption-based ionization methods.[14,20,23,32] For example, MALDI-MS and MALDI-MS imaging (MSI) tools were developed that enable pinpointing lipid DB positions. MALDI-MSI and OzID were combined by Paine et al. to visualize DB-position isomer distributions in rat brain sections with down to 80 μm lateral resolution.[20] Bednařík et al. developed on-tissue PB and ozonolysis functionalization methods for lipids to track lateral DB-position isomer variations in the brain and colon tissue with MALDI2-MS^2I and MALDI-MS^2I with down to 25 and 15 μm, respectively.[33,34] In one of our recent studies, we identified benzophenone (BPh) as a compound that can act as a MALDI matrix and reacts with lipids in a PB reaction during laser irradiation, a process termed PB-reactive MALDI.[35] This enabled in situ derivatization, DB-position assignment, and imaging of lipids in mouse brain sections and parasites with a pixel size down to 15 μm. These studies have revealed that some DB-position isomers are associated with distinct histological features and that lipid isomer abundances can change upon disease progression. As the biochemical origin of these organizational preferences is largely unknown, charting of spatially resolved lipid DB-position maps are required to develop a refined picture of local lipid metabolism.[36] In order to develop a comprehensive map of lipid abundances and DB-position expression in tissues, MALDI methods are required that facilitate high-lateral-resolution measurements (below 20 μm), allow DB-position assignment, and cover a broad range of lipid classes. Aside from appropriate MALDI equipment, the MALDI matrix is particularly important.[37,38] The matrix needs to enable high-lateral-resolution measurements, allow DB-position assignment, and enable dual-polarity measurements to cover a broad range of the chemically diverse class of lipids. MALDI matrices typically used for high-resolution MSI measurements, such as 2,5-dihydroxybenzoic acid[39] or 9-aminoacridine,[40] yield best results in positive- or negative-ion mode. Novel tailormade matrices, like acid/base bifunctional MALDI matrices, improve the detection of positive/negative ions.[41] MALDI matrices for low-molecular-weight compounds were recently reviewed.[42] However, simultaneous detection of lipids in both ion modes, DB-position assignment, and high-resolution MALDI-MSI has not been achieved yet.

Here, we evaluated the ability of 12 BPh derivatives to serve as a PB-reactive MALDI matrix and improve lipid coverage, DB-position assignment, as well as the lateral resolution in MALDI-MSI and -MS^2I compared with BPh. The reactive PB matrix with the best-combined performance characteristics in terms of MS ion signal intensity and MS^2 DB-diagnostic fragment ion intensities is demonstrated to allow dual-polarity MALDI-MSI with down to 7 μm lateral resolution, to increase the lipid class coverage compared with BPh results, to facilitate DB-position assignment of 12 lipid classes in positive- or negative-ion mode, and to enable DB-position-resolved MALDI-MS^2I with down to 10 μm pixel size. The capabilities of this novel PB-reactive matrix are showcased by imaging histological features of mouse kidney/pancreas tissue. In particular, glomeruli in the kidney are imaged in both ion polarities in MALDI-MSI experiments, and DB-position-resolved MALDI-MS^2I results of the Langerhans islets of the murine pancreas are presented.

EXPERIMENTAL SECTION

Materials and Lipid Nomenclature. Lipid standards and lipid extracts were purchased from Avanti Polar Lipids (Alabama, USA) and NOF Corporation (New York, USA). BPh, 2-benzoylpyridine (BzPy), di(pyridine-2-yl)methanone (D2PyM), di(pyridine-3-yl)methanone (D3PyM), 4-benzoylbenzoic acid (4-BzBA), 4,4′-difluorobenzophenone (DFBPh), 2-aminobenzophenone (2-ABPh), 3-aminobenzophenone (3-ABPh), 4-aminobenzophenone (4-ABPh), 1-isoquinolinyl phenyl ketone (IQPK), diazafluorenone (DAF), 9-fluorenone (9F), and 2,2′,4,4′-tetrahydroxybenzophenone (THBPh) (Figure S1) used in screening experiments were purchased from Sigma-Aldrich. All chemicals (analytical purity) were used without further purification. The lipid nomenclature introduced by Liebisch et al.[43] is adapted in this manuscript except for the DB-position notation for which the *n*-nomenclature is employed, where a DB at position *x* counted from the aliphatic end of the hydrocarbon residue (ω-carbon) is noted as "*n-x*". Consequently, a ω-6 fatty acid with 18 C-atoms and one DB is abbreviated as FA 18:1 (*n*-6).

Tissue and Sample Preparation. Cryotome (HM525; Thermo Scientific, Dreieich, Germany) sectioning of the mouse brain (C57BL6/N male and female mice, 12−20 weeks of age), mouse kidney (wt/wt male mouse, 39 weeks of age), and mouse pancreas (wt/wt female mouse, 12 weeks of age) samples was done at −20 °C, and the resulting tissue sections (20 μm thickness) were thaw-mounted on glass slides. Organ samples and tissue sections were stored at −80 °C until further use. All animal experiments were performed with the permission of the Regional Council Karlsruhe (permission number G-53/17) and conformed to the Guide for the Care and Use of Laboratory Animals (NIH Publication No. 85-23, revised 2011). The mice were housed in the Interfaculty Biomedical Research Facility (IBF) of Heidelberg University, Germany. Matrices were applied by sublimation/resublimation onto tissue sections using a homebuilt setup (Figure S2 left).[44] Lipid standards and lipid extracts were spotted onto glass slides by dried-droplet deposition (1 μL) of 10^{-3} M solutions in methanol, chloroform, or dichloromethane. After lipid deposition, 10^{-2} M solutions of the respective matrix was spotted onto the lipid sample by dried-droplet deposition (1 μL).

MALDI-MSI. An AP-SMALDI5-AF MSI ion source (TransMIT GmbH, Giessen, Germany) coupled to an orbital trapping mass spectrometer (Q Exactive or Q Exactive HF; Thermo Fisher Scientific GmbH, Bremen, Germany) was employed for the MALDI-MS, MALDI-MSI, MALDI-MS^2, and MALDI-MS^2I experiments. The full-pixel mode was used for MALDI-MS, MALDI-MS^2, and MALDI-MS^2I experiments with 10−20 μm pixel size. In full-pixel mode, the ablation area

https://dx.doi.org/10.1021/acs.analchem.0c03150
Anal. Chem. 2020, 92, 14130−14138

is increased by quickly moving the sample while operating the ablation laser with a high repetition rate.[35] For MALDI-MSI measurements, a step size of 7 μm was used to locally probe the sample surface without steering the laser across the sample. For MS, MSI, MS^2, and MS^2I, the following settings were used—mass resolution at m/z 200: 140,000 (Q Exactive) or 240,000 (Q Exactive HF); higher-energy collisional dissociation (HCD) normalized collision energy setting: between 18 and 44; inlet capillary temperature: 250 °C; S-lens setting: 100; and inlet time: 500 ms. External mass calibration for MALDI-MSI was performed using the ion signals of protonated PC 34:1 and deprotonated PI 38:4 in positive- and negative-ion mode, respectively.

Microscopy and UV/Vis Spectroscopy. Immunofluorescence staining of mouse kidney and mouse pancreas tissue sections was done following Supporting Protocol 1 and Supporting Protocol 2, respectively. Optical microscope images and fluorescence microscope images were acquired using the aid of a Keyence VHX-5000 digital microscope (Keyence Deutschland GmbH, Neu-Isenburg, Germany) and an Axiovert 2000 M microscope (Zeiss, Oberkochen, Germany), respectively. UV/vis measurements of matrix-covered cuvettes were performed using a V-550 (JASCO GmbH, Pfungstadt, Germany) instrument.

Data Analysis and Visualization. The Thermo XCalibur Qual Browser was used for manual analysis of individual or averaged mass spectra, whereas MS images were processed using Mirion imaging software.[45] Normalized level (NL) values, the intensity scale of Thermo Fisher Scientific mass spectrometers, were provided by XCalibur Qual Browser software. All images were created with a histogram bin width of 0.01 u and an absolute m/z variance of 0.01 u. Ion-signal intensities used for MALDI-MSI and MALDI-MS^2I were normalized to the total ion current (TIC) per pixel and the highest signal intensity per image. For lipid assignment in MALDI-MSI experiments, accurate m/z values were compared with exact m/z values using data bank searches in LIPID MAPS. The data bank was searched for protonated, sodiated, potassiated, and deprotonated ions in the positive- and negative-ion mode, respectively. Annotations were included in a putative lipid list if their relative m/z deviation was $\leq \pm 2$ ppm. Additional annotation criteria are detailed in the Supporting Information. The reaction yield (Y) for the attachment of neutral matrix molecules to lipid ions was calculated using MS intensities of one particular ion type ($[M + H]^+$, $[M + Na]^+$, $[M + K]^+$, or $[M - H]^-$) according to the formula Y = (product ion intensity)/(product ion intensity + unfunctionalized lipid precursor ion intensity)·100%.

Fragment Ion Nomenclature. Upon dissociative cleavage of intact oxetanes formed in PB reactions, four fragment ions per DB position can result from HCD (Scheme 1). According to the nomenclature introduced in Scheme 1, fragment ions that contain the lipid head group will be labeled as α ions. Complementary fragment ions that contain the remaining FA residue are classified as ω-ions. The location, x, of the dissociated DB, according to the above introduced DB nomenclature, is added as a superscript. If the number of DBs in the FA from which the retro-PB ions originate, #, is known or determined from MS^2 results, # is added as the second superscript. The subscript A indicates if the fragment ions formally contain an aldehyde, whereas E refers to the suffix -ene for the alkene moieties within the fragment ions.

Scheme 1. Paternò–Büchi Functionalization and Higher-Energy Collisional Dissociation of Functionalized Lipids[a]

[a] R^2 corresponds to the lipid residue containing the lipid head group, whereas R^1 comprises the remaining hydrocarbon chain.

RESULTS AND DISCUSSION

Screening of PB-Reactive Matrices. To improve the performance of our PB-reactive MALDI scheme in terms of MS intensities and reaction yields compared with BPh results, mixtures of 12 BPh derivatives with PC 18:1(n-9)/18:1(n-9) were investigated using MALDI-MS as well as MALDI-MS^2 and results are shown in Figure 1 and Figure S3. All tested matrices contain a carbonyl group to ensure PB reactivity and aromatic residues for UV absorption (Figures S1 and S4). Additional hydroxy, carboxy, and amine groups are attached to the aromatic residues of THBPh, 4-BzBA, and 2-/3-/4-ABPh to promote the protonation or deprotonation of analytes, respectively. Other potential matrices contain fluorine substituents (DFBPh), covalently interlinked aromatic residues (DAF and 9F), an expanded aromatic system (IQPK), or pyridinyl instead of phenyl moieties (BzPy, D2PyM, and D3PyM). A comparison of the NLs of protonated PC 18:1(n-9)/18:1(n-9) as a relative measure for ionization efficiency and the reaction yield derived from the [PC 18:1(n-9)/18:1(n-9) + matrix + H]$^+$ signal for all studied matrix compounds and BPh is shown in Figure 1A. Every tested compound performed as a MALDI matrix, affording NL values ranging from 3.8×10^4 for D2PyM to 1.2×10^6 for 4-ABPh, which is a 1.5- and 49.6-fold NL improvement compared with BPh, respectively. In contrast, most reaction yields of the [PC 18:1(n-9)/18:1(n-9) + matrix + H]$^+$ signal were lower or comparable to BPh results. In particular, only the matrices BzPy, D2PyM, and D3PyM gave Y values of 35 ± 6, 23 ± 7, and 18 ± 4%, respectively, which are higher or comparable to the Y value 25 ± 6% obtained for BPh.

In the next set of experiments, MALDI-MS^2 of [PC 18:1(n-9)/18:1(n-9) + matrix + H]$^+$ ions was performed to distinguish nonselective lipid-matrix compounds from PB reaction products. As highlighted in Scheme 1, collisional activation of PB product ions results in a set of product ion pairs per DB upon retro-PB oxetane cleavage, whereas only dissociation of ions/molecules containing intact matrix molecules is expected in the absence of PB reactivity. Two representative MALDI-MS^2 spectra that indicate the absence of PB reactivity and are characteristics for PB-reactive matrices are shown in Figure 1B and C, respectively. Whereas experiments with 9F resulted in the formation of [PC 18:1(n-9)/18:1(n-9) + 9F + H]$^+$ ions with a reaction yield of 5 ± 1% (Figure S3A), no retro-PB ions are present in the MALDI-MS^2 spectrum (Figure 1B). This indicates that 9F is not PB reactive (indicated in Figure 1A; shaded blue). This is in contrast to the fragment ions in MALDI-MS^2 spectra of [PC 18:1(n-9)/18:1(n-9) + BzPy + H]$^+$ (Figure 1C). The ions at m/z 676.453 and m/z 827.531 are in line with the retro-PB

https://dx.doi.org/10.1021/acs.analchem.0c03150
Anal. Chem. 2020, 92, 14130–14138

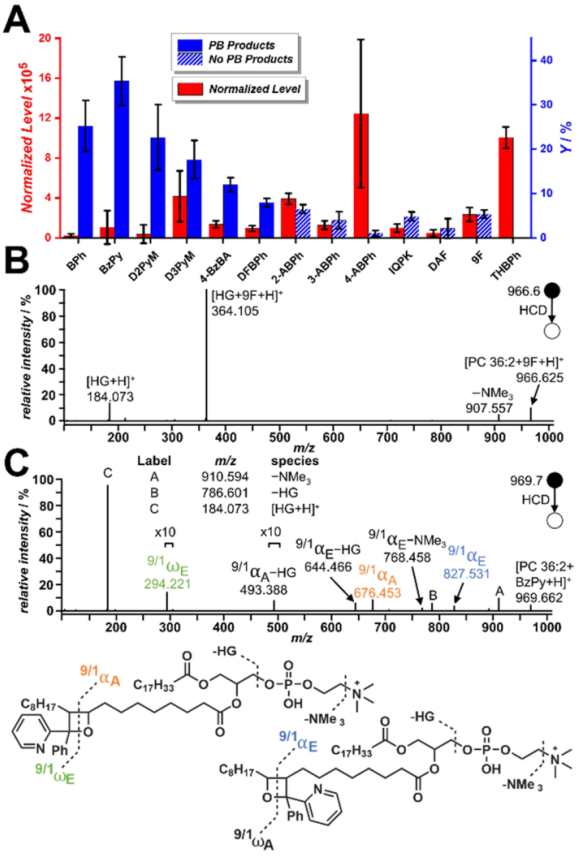

Figure 1. (A) Normalized level (red bars) and the reaction yield, *Y*, (blue bars) of screened matrices. Confirmed PB product formation and the absence of PB reactions are highlighted by full blue bars and shaded blue bars, respectively. Error bars represent one standard deviation. Positive-ion mode MALDI-MS^2 spectra of (B) [PC 18:1(*n*-9)/18:1(*n*-9) + 9F + H]$^+$ and (C) [PC 18:1(*n*-9)/18:1(*n*-9) + BzPy + H]$^+$. Corresponding oxetane structures of [PC 18:1(*n*-9)/18:1(*n*-9) + BzPy + H]$^+$ and retro-PB cleavage sites are indicated. NL − normalized level; HG − head group; NMe_3 − trimethylamine.

cleavage of oxetanes resulting in $^{9/1}\alpha_A$ and $^{9/1}\alpha_E$ fragments (Scheme 1) consistent with a PB reaction between BzPy and PC 18:1(*n*-9)/18:1(*n*-9) during MALDI. Additionally, the signal at *m/z* 294.221 indicates the protonation of the pyridine moiety, affording $^{9/1}\omega_E$ fragments not observed with BPh (Figure S5). However, prominent neutral water and matrix loss, as recently demonstrated by Xia and co-workers,[31] reveal that other reactions than PB functionalization can occur (Figure S5). According to the MALDI-MS^2 results, not only BzPy but also D2PyM, D3PyM, 4-BzBA, and DFBPh are PB-reactive MALDI matrices as highlighted in Figure 1A.

These results suggest that PB reactivity is diminished if hydroxy or amino groups are present or conformational flexibility of matrix moieties is decreased as a result of covalent interlinking of aromatic residues. The reactivity trend of identified PB-reactive matrices, however, does not correlate with available photochemical reactivity descriptors such as matrix extinction coefficients at 343 nm or phosphorescence quantum yields. Out of all tested matrices, only BzPy, D2PyM, and D3PyM afforded reaction yields higher or comparable to BPh. MALDI-MS^2 of these compounds provided α and ω retro-PB fragment ions (Figure 1C, Figure S6). Because the *Y* and NL values for α ions were higher for BzPy than those for BPh, D2PyM, and D3PyM, BzPy was used throughout the rest of the study as the reactive MALDI matrix.

Reaction Yields and DB Assignment of Lipids in Positive- and Negative-Ion Mode. To evaluate the number of lipid classes with addressable DBs compared with BPh and other DB localization methods, the DB functionalization scope of BzPy was investigated. Table S1 summarizes the corresponding positive- and negative-ion mode MALDI-MS and MALDI-MS^2 results. In particular, *Y* values of investigated lipids (FA, SHexCer, PA, PE, PI, SM, PG, PS, HexCer, CL, TG, and plasmalogen PC) along with the DB positions inferred from accurate *m/z* values (mass error ≤ ±5 ppm) of fragment ions are listed. In both ion modes, PB-functionalized lipids differ by 183.068 Da from unfunctionalized compounds. The α/ω fragment ion pairs corresponding to the same DB are separated by 151.079 Da (Scheme 1). Lipids and the corresponding reaction products were detected as [M + H]$^+$ and/or [M + Na]$^+$ and [M − H]$^-$ ions. The *Y* values for BzPy depend on the lipid class and ion identity and range from 5.0% for oleic acid to 100% for TG 54:3. The reaction yields also depend on the charge carrier identity as observed for different TG adducts. For example, the TG + matrix signals ([TG 54:3 + BzPy + H]$^+$, [TG 54:3 + 2BzPy + H]$^+$, and [TG 54:3 + 3BzPy + H]$^+$) are higher in intensity than the corresponding sodiated ion signals, even though the NL value for [TG 54:3 + Na]$^+$ is higher than that for [TG 54:3 + H]$^+$. As a consequence, the reaction yields for the sodiated TG 54:3 + BzPy species with the highest MS intensity is 70.8%, whereas *Y* calculated for the corresponding protonated signal is 100%. Similarly, the protonated-to-sodiated ion signal ratios of reaction products of PI, PA, PE, and PS were increased by a factor of 2−600 compared with unfunctionalized species. Protonated signals of PG, CL, and TG lipids were exclusively observed for BzPy-modified compounds. These results suggest that BzPy attachment can affect ionization yields of products compared with unfunctionalized lipids. This is also in line with the recent PB-ESI-MS results by Ma,[26] Xia,[31] and our group[28] that documented the ability to enhance ionization efficiencies using various pyridine-containing PB-reactive compounds. Therefore, *Y* values are affected by the intrinsic matrix reactivity and ionization efficiency changes. In general, these results indicate that BzPy can ionize all tested lipid standards in positive- and/or negative-ion mode and can increase the MS intensity of lipid ions upon BzPy attachment.

Next, HCD fragmentation of BzPy-adduct ions was used to investigate the influence of lipid classes and ion modes on the ability to assign DB positions. As listed in Table S1, α_A and α_E ions were detected for all lipid species except for PS 16:0/18:1(*n*-9) and SHexCer 42:2(*n*-9) for which the α_E signals are absent in the MS^2 spectra. To the best of our knowledge, the list includes MALDI-MS^2 DB localization for lipid classes not reported before. Some representative examples are shown in Figure 2 and Figure S7 , and MS^2 spectra of the other tested lipids are shown in Figures S8 and S9. For example, TG 54:3 readily reacts with BzPy during MALDI to form mono-, di-, and tri-PB-functionalized protonated or sodiated ions (Figure S9). The MS^2 spectra of [TG 54:3 + 3BzPy + H]$^+$ and mono- and difunctionalized protonated and sodiated TG 54:3 are shown in Figure 2A and Figure S9B−E, respectively. Similar to mono- and difunctionalized counterparts, HCD of [TG 54:3 +

https://dx.doi.org/10.1021/acs.analchem.0c03150
Anal. Chem. 2020, 92, 14130−14138

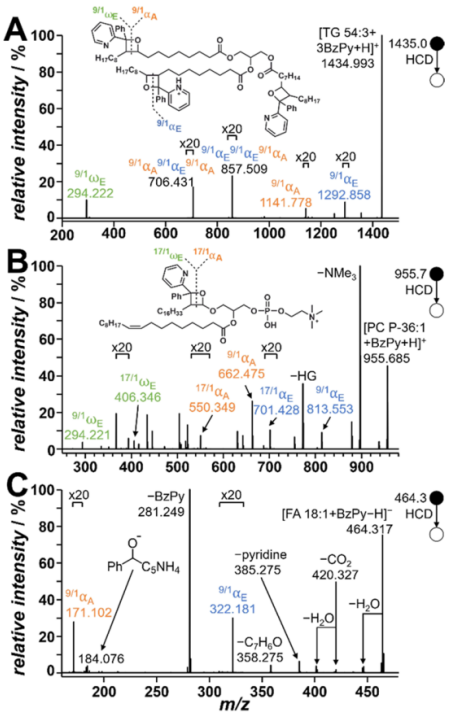

Figure 2. MALDI-MS^2 spectra of BzPy-functionalized (A) TG 18:1(n-9)/18:1(n-9)/18:1(n-9), (B) PC P-18:0/18:1(n-9), and (C) FA 18:1(n-9). See Figure S7 for additional assignments.

3BzPy + H]$^+$ yielded α_A, α_E, and ω_E fragment ions resulting from a combination of multiple retro-PB events. All HCD results for TGs exhibit protonated or sodiated $^{9/1}\omega_E$ ion signals. This indicates that charge carriers can migrate to or are located at BzPy. Because the appearance of ω_E ion signals documents the propensity of BzPy toward charge carries, these results also support the finding that the ionization efficiency is changed due to BzPy attachment.

Another example for DB assignment is shown in Figure 2B for the plasmalogen PC P-18:0/18:1(n-9) that possesses a vinylic and an isolated DB at positions n-17 and n-9, respectively. HCD of [PC P-18:0/18:1(n-9) + BzPy + H]$^+$ afforded multiple DB fragment ions including protonated α_A, α_E, and ω_E ions that enable the DB assignment of the free and the vinylic DBs. In contrast to the reports of Lin et al. who observed a preference for α_E fragments from plasmalogen DBs, α fragments were detected with similar abundances (α_E:α_A = 1.4:1).[46] To demonstrate the use of BzPy in negative-ion mode DB localization, MALDI-MS^2 of deprotonated FA 18:1(n-9) (Figure 2C) and SHexCer 42:2(n-9) (Figure S8A) were performed. Despite the low intensity of retro-PB fragment ions (0.3−2.2% relative to the precursor ions), $^{9/1}\alpha_A/^{9/1}\alpha_E$ and $^{9/1}\alpha_A$ ions enabled DB-position assignment for FA 18:1(n-9) and SHexCer 42:2(n-9) in negative-ion mode using MALDI-MS^2 for the first time, respectively. Next, we investigated if reactive MALDI using BzPy allows us to relatively quantify DB-position isomers. Solutions of the isomeric lipid standards PC 18:1(n-12)/18:1(n-12) and PC 18:1(n-9)/18:1(n-9) were mixed in defined molar ratios, and MALDI-MS^2 experiments were performed. The MS^2 intensity ratios of the isomer-specific $^{12/1}\alpha_A$ and $^{9/1}\alpha_A$ ions linearly correlate with the molar ratios (R^2 = 0.999), showcasing the ability to differentiate and relatively quantify lipid DB-position isomers using the reactive matrix BzPy (Figure S7D).

These results demonstrate the multifunctional character of BzPy as a MALDI matrix: The compound enables lipid ionization in positive- and negative-ion mode, enhances MS signals for some lipids upon reaction, and improves the ability introduced with BPh to identify and relatively quantify DB positions of lipids in positive-ion mode while extending the DB addressable lipid classes.

MSI Lipid Class Coverage in the Mouse Cerebellum. As the ionization of many lipid classes suffers from the ion suppression effect,[47] the coverage of lipid classes in mouse cerebellum tissue was evaluated to assess the suitability of BzPy for comprehensive lipid coverage in MSI studies (Figure 3,

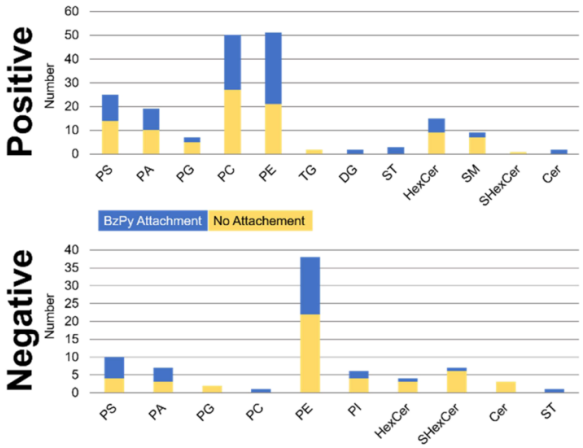

Figure 3. Assigned compounds and the corresponding lipid classes in (upper row) positive- and (lower row) negative-ion mode from MALDI-MSI measurements of BzPy-covered mouse cerebellum tissue. The numbers of lipids with and without BzPy-attachment are highlighted as blue and yellow bars, respectively.

Figure S10). In total, 251/79 features were assigned to 133/58 lipids in the positive-/negative-ion mode. Figure S11A gives an overview of the assigned lipids and lipid classes. Corresponding subclasses are shown in Figure S11B−D. Tables S2−S6 list all the assigned lipid species. As expected, the assigned lipids are dominated by 107/45 glycerophospholipids (GPLs) but also 4/0 GLs, 19/12 sphingolipids (SLs), and 3/1 sterols (STs) are present in positive-/negative-ion mode (Figure S11A top rows). In addition to the detected unfunctionalized species (Figure S11A middle rows), 48/41% of the annotated signals are BzPy-attached species in positive-/negative-ion mode. This includes lipids annotated either without and with BzPy, and 37/11 assignments in positive-/negative-ion mode that were exclusively detected as BzPy adducts (Figure S11). This underlines the advantage of using a reactive matrix that facilitates ionization. Because BzPy attachment was observed for unsaturated and saturated lipids, BzPy most likely also reacts with the head group, in a reaction other than PB functionalization, or attaches to lipids in a noncovalent manner. This is also consistent with the reports by Xia[31] and Hayen[30] about PB reaction by-products in in-solution reactions. The numbers of lipids with or without BzPy attachment are compared in Figure 3. For example, BzPy attachment increases the number of detectable PEs and PCs by

https://dx.doi.org/10.1021/acs.analchem.0c03150
Anal. Chem. 2020, 92, 14130−14138

30 and 71% in positive-ion mode as well as PSs, PAs, and PIs by 43, 75, and 50% in negative-ion mode, respectively. Some lipids, namely, DGs, STs, and CerPs, are only detected due to BzPy attachment, highlighting the potential of BzPy to provide increased lipid coverage in comparison with BPh.

Dual-Polarity High-Resolution MALDI-MSI of the Mouse Kidney. After evaluating the matrix crystal size, PB and retro-PB reactivity, and the lipid class coverage of BzPy, the ability to perform MALDI-MSI experiments in both ion modes with pixel resolutions down to 7 μm was tested. For this purpose, lipid distributions were visualized from transverse mouse kidney sections, and Figure 4 displays the RGB

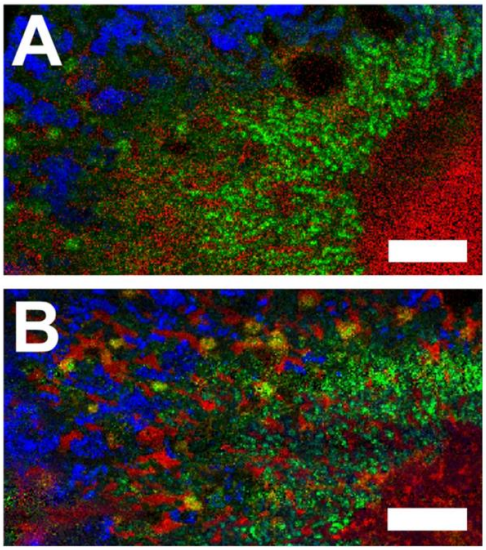

Figure 4. RGB MALDI-MS images of the mouse kidney acquired in (A) positive- and (B) negative-ion mode with 7 μm step size. The lateral resolved signal intensities of $[PS\ O\text{-}36{:}1 + H]^+$ (red, m/z 776.581), $[SM\ 34{:}1 + H]^+$ (green, m/z 703.575), and $[PE\ 38{:}0 + K]^+$ (blue, m/z 814.573) in the positive-ion mode and $[PA\ 36{:}1 - H]^-$ (red, m/z 701.513), $[PE\text{-}Cer\ 36{:}1 - H]^-$ (green, m/z 687.544), and $[SHexCer\ 42{:}2 - H]^-$ (blue, m/z 888.623) in the negative-ion mode were superimposed. The scale bars reflect 400 μm.

MALDI-MS images (7 μm step size) of $[PS\ O\text{-}36{:}1 + H]^+$ (red), $[SM\ 34{:}1 + H]^+$ (green), and $[PE\ 38{:}0 + K]^+$ (blue) in the positive-ion mode and $[PA\ 36{:}1 - H]^-$ (red), $[PE\text{-}Cer\ 36{:}1 - H]^-$ (green), and $[SHexCer\ 42{:}2 - H]^-$ (blue) in the negative-ion mode. Fluorescence microscopy images of post-MALDI-MSI immunofluorescence-stained sections (following Supporting Protocol 1) are shown in Figure S12. A comparison of MSI results in Figure 4 and microscopic images in Figure S12 allows us to correlate histological regions, for example, glomeruli with synaptopodin, with mass spectrometrically recorded lipid distributions. Whereas $[PS\ O\text{-}36{:}1 + H]^+$ and $[PA\ 36{:}1 - H]^-$ are associated with the inner renal medulla and the renal tubules, $[SM\ 34{:}1 + H]^+$ and $[PE\text{-}Cer\ 36{:}1 - H]^-$ are located in the outer renal medullary interstitium regions and the glomeruli. High signal intensities of $[PE\ 38{:}0 + K]^+$ and $[SHexCer\ 42{:}2 - H]^-$ are associated with the renal cortex.[48] Further MS images are presented in Figures S13 and S14 for both ion polarities and 7 μm pixel size and 10 μm pixel size as shown in Figure S15. For example, the regions with low or no ion intensity in Figure 4 are renal blood vessels (Figure S16) and are linked with other lipids such as $[PC\ 34{:}0 + K]^+$ (Figure S13J). In addition to unfunctionalized lipids, BzPy allows us to image lipid + BzPy ion signals. Representative examples are shown in Figure S17 (positive-ion mode) and Figure S18 (negative-ion mode) and indicate that the lateral distributions of BzPy-derivatized lipids and unfunctionalized compounds are similar. For example, high signal intensities of $[SM\ 34{:}1 + H]^+$ and $[SM\ 34{:}1 + BzPy{+}H]^+$ (Figure S17A) are linked to the medullary interstitium and glomeruli. Additionally, the correlation between MALDI-MSI and optical microscopy suggests that no wash-out effects occur with BzPy as the MALDI matrix and that BzPy can be used to visualize and differentiate histological features in tissues with down to 7 μm in positive- and negative-ion mode.

On-Tissue DB Assignment of Lipids. To investigate the capabilities of BzPy as a reactive matrix for lipid DB-position assignment in complex lipid mixtures, the mouse cerebellum, kidney, and pancreas tissues were studied in positive- and negative-ion mode. Representative MS^2 results for $[PC\ 36{:}2 + BzPy{+}H]^+$ (pancreas) and $[PC\ 34{:}1 + BzPy{+}H]^+$ (pancreas), as well as $[PC\ O\text{-}38{:}6 + BzPy{+}H]^+$ (kidney), $[PC\ 36{:}4 + BzPy{+}H]^+$ (pancreas), $[PC\ 36{:}3 + BzPy{+}H]^+$ (pancreas), and $[SHexCer\ 42{:}2 + BzPy{-}H]^-$ (cerebellum), are shown in Figure 5 and Figures S19 and S20, respectively. For all compounds, α and/or ω ions enabled the assignment of DB positions. Whereas retro-PB fragments for SHexCer 42:2 (Figure S20), PC O-38:6 (Figure S19A), and PC 36:4 (Figure S19B) are consistent with the presence of only a single DB-position isomer, multiple isomers are present for PC 36:2 (Figure 5A), PC 34:1 (Figure 5B), and PC 36:3 (Figure S19C). In particular, α/ω ions for PC 34:1, PC 36:2, and PC 36:3 point to the presence of two, three, and five DB positions, respectively. For example, retro-PB fragment ions of PC 36:2 indicate that mono- and diunsaturated FAs, such as PC 18:1_18:1 and PC 18:0_18:2, are combined and that their DBs are located at n-6, n-7, and n-9. Fragment ions of PC 36:2 wherein all DBs are lost allow us to connect them to either mono- or diunsaturated FAs. This is because the corresponding neutral loss channels from a diunsaturated FA contain intact DBs, shifting the neutral loss by −2.016 Da compared with the fragment ions stemming from monounsaturated FAs. DB-retaining fragment ions do not allow us to distinguish mono- and diunsaturated FAs, but in combination with the lack of corresponding unsaturated neutral losses, these fragments indicate the presence of a monounsaturated FA. These results suggest that BzPy enables DB assignment of mono- and polyunsaturated lipids in positive- and negative-ion mode directly from tissues.

Resolving DB-Position Isomers in Pancreatic ß-Cells. To demonstrate the improvement in lateral resolution for DB-position isomer localization when using BzPy compared with BPh, mouse pancreas tissue sections were investigated with MALDI-MS^2I. An average MALDI mass spectrum is shown in Figure S21, revealing endogenous lipids and the corresponding derivatization products detected in the pancreas tissue. MALDI-MSI distributions of lipids were largely in line with previous studies of the pancreas tissue.[49] Multiple ion signals of BzPy-derivatized lipids were subjected to MALDI-MS^2I. Namely, protonated signals of PC 34:1 + BzPy, PC 36:2 + BzPy, PC 36:4 + BzPy, and PC 34:2 + BzPy were fragmented, and α_A ions were employed to visualize lateral DB-position isomer distributions with 10 μm pixel size (Figure 5 and Figures S22 and S23). To the best of our knowledge, this is the

https://dx.doi.org/10.1021/acs.analchem.0c03150
Anal. Chem. 2020, 92, 14130−14138

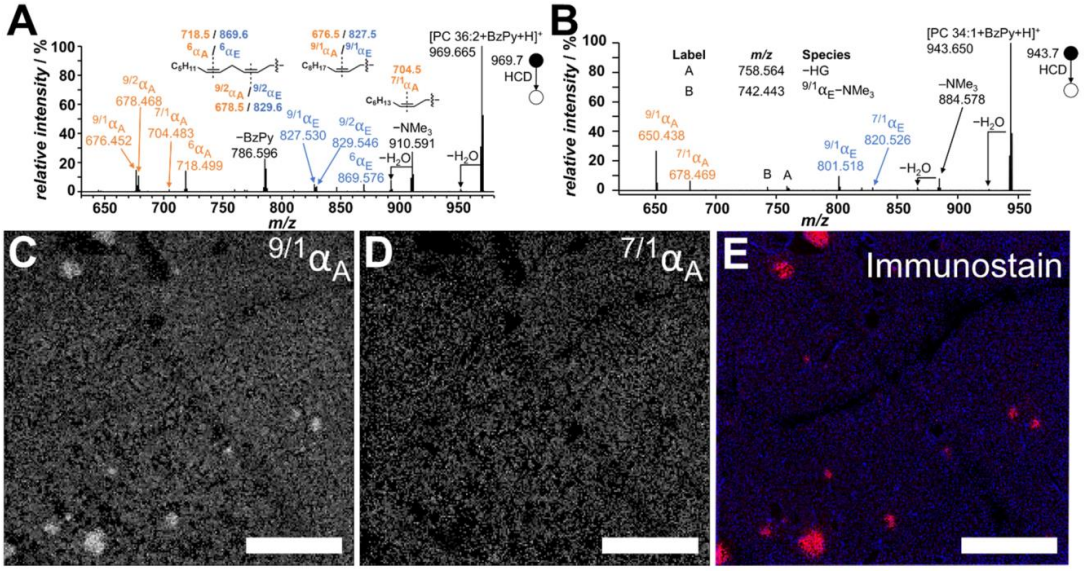

Figure 5. MALDI-MS^2 spectra of (A) [PC 36:2 + BzPy+H]$^+$ and (B) [PC 34:1 + BzPy+H]$^+$ desorbed from mouse cerebellum and mouse pancreas tissue, respectively. TIC-normalized MALDI-MS^2 images of diagnostic fragment ions (C) $^{9/1}\alpha_A$ (m/z 650.439) and (D) $^{7/1}\alpha_A$ (m/z 678.470) of DB-position isomers of [PC 34:1 + BzPy+H]$^+$ were acquired from mouse pancreas tissue with 10 μm pixel size. (E) Fluorescence microscopy image of the post-MALDI-MS^{2}I-immunofluorescence-stained pancreas tissue section. Red areas in E indicate insulin-positive β-cells in the Langerhans islets. The scale bars reflect 600 μm.

highest reported lateral resolution for DB-position isomer imaging. Protonated PC 34:2 + BzPy and PC 36:4 + BzPy did not show DB-position isomerism. Consequently, all DB fragment ions showed similar lateral distributions (Figure S23). In contrast, protonated PC 34:1 + BzPy and PC 36:2 + BzPy possess several isomers with DBs in the positions n-9 and n-7 and n-9, n-7, and n-6, respectively. The lateral distributions of these isomers differed. Local upregulation of mass spectrometric intensities linked with the n-9 isomer of PC 34:1 was observed in circular areas with 50−150 μm diameter (Figure 5C), contrasted by the $^{7/1}\alpha_A$ ion intensities decreased in the same regions (Figure 5D). After post-MALDI-MS^{2}I immunfluorescence staining, fluorescence microscopy was performed to assign PC 34:1 isomer distribution to specific histological regions in the pancreatic tissue, and the results are shown in Figure 5E. Red fluorescence indicates the location of Langerhans islets, whereas cell nuclei are colored blue. A comparison of MALDI-MS^{2}I results for PC 34:1 with fluorescence microscopy reveals that tissue regions with high $^{9/1}\alpha_A$ and low $^{7/1}\alpha_A$ intensities are correlated with the location of pancreatic islets. Differing lateral distributions were also observed for the DB-position isomers of PC 36:2. The α_A ions of the PC 36:2 isomer possessing a diunsaturated FA with DBs at positions n-6 and n-9 are homogenously distributed (Figure S22A,B). In contrast, $^{9/1}\alpha_A$ and $^{7/1}\alpha_A$ ions of the isomers with two monounsaturated FAs are both enriched in the pancreatic islets (Figure S22C,D). The murine Langerhans islets predominantly consist of β-cells.[50] Consequently, the increased mass spectrometric abundances in the pancreatic islets are directly linked to β-cells and are distinctly different from the surrounding tissue. This finding suggests that the enriched lipid DB-position isomers fulfill specific functions in β-cells or are linked to metabolic reactions in β-cells that predominantly give rise to lipids with well-defined DB positions.

CONCLUSIONS

Screening of 12 aromatic carbonyl compounds revealed pyridine derivatives of BPh as novel PB reactive MALDI matrices for DB position-resolved MALDI-MS^{2}I and high-resolution dual-polarity MALDI-MSI studies. In particular, BzPy improves ion intensities in positive-ion mode, the reaction yield, and the number as well as relative signal intensities of DB-position diagnostic fragment ions compared with BPh. In situ PB functionalization using PB-reactive MALDI and MS^2 DB localization is presented for GPLs, SLs, and a TG in the positive-ion mode as well as for an FA and a SHexCer in the negative-ion mode. This extends the number of lipid classes with addressable DB positions compared with the previously reported desorption-based MS^2 strategies. PB and nonspecific functionalization of lipids with BzPy during MALDI allows us to increase lipid ion intensities and lipid coverage compared with BPh results. Namely, a total of 133/58 features were assigned in positive-/negative-ion mode including GPLs, GLs, SLs, and STs.

The capabilities of spatially resolved lipidomics have been demonstrated by on-tissue MALDI-MS^2, MALDI-MSI, and MALDI-MS^{2}I from different mouse tissues. High-resolution dual-polarity MALDI-MSI (7 μm) of the mouse kidney allows us to link lateral distributions of endogenous lipids and histological features, such as glomeruli, by post-MSI immunofluorescence microscopy. In comparison to BPh, the improvement in lateral resolution and detectable diagnostic fragment ions of MALDI-MS^{2}I is showcased by DB-position isomer-resolved MS^2 images of PCs with down to 10 μm in mouse pancreas tissue sections. We observed up- and downregulation of the n-9 and n-7 isomers in areas that match with the islets of Langerhans.

The caveat of our methodology, similar to DESI and other MALDI workflows, is the ion suppression effect that makes MALDI-MS^{2}I experiments challenging. Whereas signal in-

https://dx.doi.org/10.1021/acs.analchem.0c03150
Anal. Chem. 2020, 92, 14130−14138

tensities for ∼90% of PCs and SMs are sufficient for DB assignment, DB positions of suppressed lipid classes from tissue are not accessible. Even though the matrix BzPy has considerably increased lipid coverage, allowed negative-ion mode investigations, and improved the lateral resolution compared with BPh, other laser wavelengths, matrix systems that provide higher Y values to decrease spectral complexity due to additional lipid + matrix signals, or postionization schemes are most likely necessary to probe DB-position isomerism in tissue samples for lipid classes other than PCs, SMs, and SHexCers. These investigations are currently underway.

In terms of applications, we envision that the herein introduced BzPy matrix can be used to study local lipid isomer variations in pancreas and kidney tissues in the context of diabetes. Diabetes and related metabolic malfunctions have been linked with lipid, especially local PC, alterations in these organs, and we are keen to explore spatially resolved lipid isomerism to contribute to an understanding of altered lipid metabolism.

■ ASSOCIATED CONTENT

Supporting Information

The Supporting Information is available free of charge at https://pubs.acs.org/doi/10.1021/acs.analchem.0c03150.

Experimental details, annotation criteria, and protocols; MSI results using BzPy as MALDI matrix; solid-phase UV spectrum of BzPy; lipid MALDI-MS^2 for reactive matrices; assigned lipid classes; immunofluorescence results of the mouse kidney; positive- and negative-ion mode MALDI-MSI of the kidney with 7 and 10 μm pixel size; comparison of endogenous and corresponding BzPy distributions in the kidney; additional DB-position-resolved MALDI-MS^2 results for the mouse kidney; and MALDI-MS^2 as well as MALDI-MS^{2}I results for pancreas sections (PDF)

■ AUTHOR INFORMATION

Corresponding Author

Sven Heiles − *Institute of Inorganic and Analytical Chemistry, Analytical Chemistry, Justus Liebig University Giessen, 35392 Giessen, Germany*; orcid.org/0000-0003-3779-8071; Email: sven.heiles@anorg.chemie.uni-giessen.de

Authors

Fabian Wäldchen − *Institute of Inorganic and Analytical Chemistry, Analytical Chemistry, Justus Liebig University Giessen, 35392 Giessen, Germany*

Franziska Mohr − *Department of Cardiovascular Physiology, Heidelberg University, 69120 Heidelberg, Germany*

Andreas H. Wagner − *Department of Cardiovascular Physiology, Heidelberg University, 69120 Heidelberg, Germany*

Complete contact information is available at: https://pubs.acs.org/10.1021/acs.analchem.0c03150

Author Contributions

S.H. supervised the project. S.H. and F.W. designed and F.W. performed the MS experiments. A.H.W. and F.M. performed the immunofluorescence experiments. S.H., F.W., and A.H.W. discussed the findings, and S.H. and F.W. wrote the manuscript with the input of A.H.W.

Notes

The authors declare no competing financial interest.

■ ACKNOWLEDGMENTS

S.H. acknowledges the Fonds der chemischen Industrie for financial support through a Liebig fellowship. Financial support by the Deutsche Forschungsgemeinschaft (HE 8521/1-1) and institutional funds (A.W.) is gratefully acknowledged. All authors thank Dr. Daniela Fietz (Institute of Veterinary Anatomy, Histology and Embryology, JLU Giessen) for providing mouse brain samples.

■ REFERENCES

(1) Han, X. *Nat. Rev. Endocrinol.* **2016**, *12*, 668−679.
(2) Yang, K.; Han, X. *Trends Biochem. Sci.* **2016**, *41*, 954−969.
(3) Tsugawa, H.; Ikeda, K.; Takahashi, M.; et al. *Nat. Biotechnol.* **2020**, 1−5.
(4) Harayama, T.; Riezman, H. *Nat. Rev. Mol. Cell Biol.* **2018**, *19*, 281−296.
(5) Vriens, K.; Christen, S.; Parik, S.; et al. *Nature* **2019**, *566*, 403−406.
(6) Volmer, R.; Ploeg, K.; Ron, D. *Proc. Natl. Acad. Sci. U. S. A.* **2013**, *110*, 4628−4633.
(7) Cunha, D. A.; Hekerman, P.; Ladrière, L.; et al. *J. Cell Sci.* **2008**, *121*, 2308−2318.
(8) Fu, S.; Yang, L.; Li, P.; et al. *Nature* **2011**, *473*, 528−531.
(9) Sustarsic, E. G.; Ma, T.; Lynes, M. D.; et al. *Cell Metab* **2018**, *28*, 159−174.e11.
(10) Bergholt, M. S.; Serio, A.; McKenzie, J. S.; et al. *ACS Cent. Sci.* **2018**, *4*, 39−51.
(11) Ellis, S. R.; Paine, M. R. L.; Eijkel, G. B.; et al. *Nat. Methods* **2018**, *15*, 515−518.
(12) Murphy, R. C.. *Tandem mass spectrometry of lipids*; Royal Society of Chemistry: Cambridge, 2015.
(13) Vasilopoulou, C. G.; Sulek, K.; Brunner, A.-D.; et al. *Nat. Commun.* **2020**, *11*, 331.
(14) Feider, C. L.; Macias, L. A.; Brodbelt, J. S.; Eberlin, L. S. *Anal. Chem.* **2020**, *92*, 8386−8395.
(15) Blevins, M. S.; James, V. K.; Herrera, C. M.; Purcell, A. B.; Trent, M. S.; Brodbelt, J. S. *Anal. Chem.* **2020**, *92*, 9146−9155.
(16) Klein, D. R.; Feider, C. L.; Garza, K. Y.; Lin, J. Q.; Eberlin, L. S.; Brodbelt, J. S. *Anal. Chem.* **2018**, *90*, 10100−10104.
(17) Fang, M.; Rustam, Y.; Palmieri, M.; Sieber, O. M.; Reid, G. E. *Anal. Bioanal. Chem.* **2020**, *412*, 2339−2351.
(18) Narreddula, V. R.; Boase, N. R.; Ailuri, R.; et al. *Anal. Chem.* **2019**, *91*, 9901−9909.
(19) Pham, H. T.; Julian, R. R. *Int. J. Mass Spectrom.* **2014**, *370*, 58−65.
(20) Paine, M. R. L.; Poad, B. L. J.; Eijkel, G. B.; et al. *Angew. Chem., Int. Ed.* **2018**, *57*, 10530−10534.
(21) Kirschbaum, C.; Saied, E. M.; Greis, K.; et al. *Angew. Chem., Int. Ed.* **2020**, *59*, 13126−13126.
(22) Feng, Y.; Chen, B.; Yu, Q.; Li, L. *Anal. Chem.* **2019**, *91*, 1791−1795.
(23) Kuo, T.-H.; Chung, H.-H.; Chang, H.-Y.; et al. *Anal. Chem.* **2019**, *91*, 11905−11915.
(24) Esch, P.; Heiles, S. *Analyst* **2020**, *145*, 2256−2266.
(25) Birk, F.; Fraatz, M. A.; Esch, P.; Heiles, S.; Pelzer, R.; Zorn, H. *J. Agric. Food Chem.* **2019**, *67*, 13460−13469.
(26) Cao, W.; Cheng, S.; Yang, J.; et al. *Nat. Commun.* **2020**, *11*, 375.
(27) Li, H.-F.; Cao, W.; Ma, X.; Xie, X.; Xia, Y. *Zheng Ouyang. J. Am. Chem. Soc.* **2020**, *142*, 3499−3505.
(28) Esch, P.; Heiles, S. J. *Am. Soc. Mass Spectrom.* **2018**, *29*, 1971−1980.
(29) Ma, X.; Xia, Y. *Angew. Chem., Int. Ed.* **2014**, *53*, 2592−2596.
(30) Jeck, V.; Froning, M.; Tiso, T.; Blank, L. M.; Hayen, H. *Anal. Bioanal. Chem.* **2020**, *412*, 1−13.

(31) Xie, X.; Zhao, J.; Lin, M.; Zhang, J.-L.; Xia, Y. *Anal. Chem.* **2020**, *92*, 8487−8496.
(32) Spraggins, J. M.; Djambazova, K. V.; Rivera, E. S.; et al. *Anal. Chem.* **2019**, *91*, 14552−14560.
(33) Bednařík, A.; Bölsker, S.; Soltwisch, J.; Dreisewerd, K. *Angew. Chem., Int. Ed.* **2018**, *57*, 12092−12096.
(34) Bednařík, A.; Preisler, J.; Bezdeková, D.; et al. *Anal. Chem.* **2020**, *92*, 6245−6250.
(35) Wäldchen, F.; Spengler, B.; Heiles, S. J. *Am. Chem. Soc.* **2019**, *141*, 11816−11820.
(36) Porta Siegel, T.; Ekroos, K.; Ellis, S. R. *Angew. Chem., Int. Ed.* **2019**, *58*, 6492−6501.
(37) Heiles, S.; Kompauer, M.; Müller, M. A.; Spengler, B. J. *Am. Soc. Mass Spectrom.* **2020**, *31*, 326−335.
(38) Gilmore, I. S.; Heiles, S.; Pieterse, C. L. *Annu. Rev. Anal. Chem.* **2019**, *12*, 201−224.
(39) Kampmeier, J.; Dreisewerd, K.; Schürenberg, M.; Strupat, K. *Int. J. Mass Spectrom.* **1997**, *169-170*, 31−41.
(40) Cerruti, C. D.; Benabdellah, F.; Laprévote, O.; Touboul, D.; Brunelle, A. *Anal. Chem.* **2012**, *84*, 2164−2171.
(41) Huang, P.; Huang, C.-Y.; Lin, T.-C.; et al. *Anal. Chem.* **2020**, *92*, 7139−7145.
(42) Calvano, C. D.; Monopoli, A.; Cataldi, T. R. I.; Palmisano, F. *Anal. Bioanal. Chem.* **2018**, *410*, 4015−4038.
(43) Liebisch, G.; Vizcaíno, J. A.; Köfeler, H.; et al. *J. Lipid Res.* **2013**, *54*, 1523−1530.
(44) Hankin, J. A.; Barkley, R. M.; Murphy, R. C. J. *Am. Soc. Mass Spectrom.* **2007**, *18*, 1646−1652.
(45) Paschke, C.; Leisner, A.; Hester, A.; et al. *J. Am. Soc. Mass Spectrom.* **2013**, *24*, 1296−1306.
(46) Lin, Q.; Zhang, D.; Xia, Y. *Analyst* **2020**, *145*, 513−522.
(47) Boskamp, M. S.; Soltwisch, J. *Anal. Chem.* **2020**, *92*, 5222−5230.
(48) Bowman, A. P.; Bogie, J. F. J.; Hendriks, J. J. A.; et al. *Anal. Bioanal. Chem.* **2020**, *412*, 2277−2289.
(49) Prentice, B. M.; Hart, N. J.; Phillips, N.; et al. *Diabetologia* **2019**, *62*, 1036−1047.
(50) Nie, J.; Liu, X.; Lilley, B. N.; et al. *Proc. Natl. Acad. Sci. U. S. A.* **2013**, *110*, 13857−13862.

https://dx.doi.org/10.1021/acs.analchem.0c03150
Anal. Chem. 2020, 92, 14130−14138

Acknowledgements

First, I want to thank Prof. Dr. Bernhard Spengler for the opportunity to work in such a productive group and with the modern instruments and equipment of his laboratories. It was a very valuable experience.

Thanks also go to Prof. Dr. Richard Göttlich and Prof. Dr. Gerd Hamscher for their willingness to be referees of this thesis.

Special thanks are due to my supervisor Prof. Dr. Sven Heiles who was not only a very good mentor and pushed the project by new challenges but also considered my ideas and promoted my talents.

Besides thanking the whole working group for sharing a great time, I want to emphasize how grateful I am for the many precious conversations with Stefanie Gerbig, Parviz Ghezellou and Simon Becher.

Finally, I want to thank my family and friends and my girlfriend for supporting me in so many ways that the list would be longer than this thesis.

Declaration

I declare that I have completed this dissertation single-handedly without the unauthorized help of a second party and only with the assistance acknowledged therein. I have appropriately acknowledged and cited all text passages that are derived verbatim from or are based on the content of published work of others, and all information relating to verbal communications. I consent to the use of an anti-plagiarism software to check my thesis. I have abided by the principles of good scientific conduct laid down in the charter of the Justus Liebig University Giessen „Satzung der Justus-Liebig-Universität Gießen zur Sicherung guter wissenschaftlicher Praxis“ in carrying out the investigations described in the dissertation.

Place, Date

Fabian Wäldchen

Erklärung

Ich erkläre: Ich habe die vorgelegte Dissertation selbstständig und ohne unerlaubte fremde Hilfe und nur mit den Hilfen angefertigt, die ich in der Dissertation angegeben habe. Alle Textstellen, die wörtlich oder sinngemäß aus veröffentlichten Schriften entnommen sind, und alle Angaben, die auf mündlichen Auskünften beruhen, sind als solche kenntlich gemacht. Ich stimme einer evtl. Überprüfung meiner Dissertation durch eine Antiplagiat-Software zu. Bei den von mir durchgeführten und in der Dissertation erwähnten Untersuchungen habe ich die Grundsätze guter wissenschaftlicher Praxis, wie sie in der „Satzung der Justus-Liebig-Universität Gießen zur Sicherung guter wissenschaftlicher Praxis“ niedergelegt sind, eingehalten.

Ort, Datum

Fabian Wäldchen